MINIATURIZED, INHERENTLY MATCHED, AND SCALABLE FOLDED DIPOLE ANTENNAS WITH APPLICATIONS IN NARROWBAND SENSING

by

SANGHAMITRO DAS

A thesis submitted in partial fulfillment of the requirements for the degree of

Doctor of Philosophy

in

Electromagnetics and Microwaves

Department of Electrical and Computer Engineering

University of Alberta

Abstract

This work presents a novel technique for miniaturizing folded dipole antennas using a simple series reactive loading scheme that enables the input impedance to be engineered, such that the antenna can be matched inherently to either a real or a complex source impedance at a specified level of miniaturization. This ability to achieve good matching with respect to an essentially arbitrary source impedance allows these miniaturized antennas to be integrated into various wireless systems without using an external matching network, which usually increases the overall size and complexity.

First, the well-known analytical model of an unloaded folded dipole antenna is extended to include the effects of reactive loading. Initially, a symmetric loading scheme is chosen, where it has been shown that in order to realize good matching conditions, an extremely large loading inductance and an extremely small loading capacitance will be necessary. However, if asymmetries are introduced in the loading scheme, the required loading values can become much smaller and more easily realizable.

The conclusions from this study are then applied in order to realize a practical example, where a printed folded dipole antenna is miniaturized to 25% of its resonant length by employing a fully asymmetric loading scheme, i.e., one arm of the antenna is made inductive and the other is made capacitive, and excellent matching is achieved with respect to a selected source impedance. The widths of the folded dipole arms are also made unequal in order to use as an additional degree of freedom. A unique feed structure is also designed to provide a balanced input to the antenna. It is shown that any effects from this feed or other practical losses can be compensated easily by adjusting the loading reactance values. Furthermore, it is found that the miniaturized folded dipole antenna has a radiation efficiency that is comparable to that of an equivalent loaded conventional dipole antenna, however by virtue of being inherently matched (and therefore not requiring a potentially lossy and bulky external matching network), the folded dipole antenna exhibits a better realized gain, and hence a higher radiated power. The antenna is fabricated and experimental results are found to be in excellent agreement with the simulated.

Finally, the applicability of this miniaturization technique is studied for narrowband electrically small sensor antennas. A 75% miniaturized fully printed folded dipole prototype is designed for matching to a real source impedance at the UHF ISM frequency band (902-928 MHz) specified for sensing applications in North America. In the next step, the input-impedance engineering technique is extended to match an equally miniaturized folded dipole antenna to a complex source impedance, and its suitability as a RFID tag antenna is discussed. Once again, excellent agreement is found between the measured and simulated results for both designs.

Preface

This thesis presents a miniaturization technique for folded dipole antennas, where the end product is an electrically small and inherently matched antenna that does not require any external matching network. My supervisor Prof. A. K. Iyer provided me with the initial idea, and I developed the corresponding miniaturization technique, including performing the simulations and measurements for all the reported antennas. Prof. Iyer played a strong supervisory role throughout the work.

A portion of this research was conducted under collaboration with Sensors and Software Inc., Mississauga, ON, Canada, which have been reported in Chapter 4 and Section 5.2. Dr. Nectaria Diamanti and Dr. A. Peter Annan from Sensors and Software helped with their ideas and opinions during the course of this collaboration. My colleague David J. Sawyer helped me with setting up the measurements and in the design/layout of the feed network for the fabricated prototype. This part of the work resulted in two abstract submissions:

[1] S. Das, A. K. Iyer, A. P. Annan, and N. Diamanti, "Study of reactive loading for the miniaturization of folded dipole antennas," *IEEE International Symposium on Antennas and Propagations and North American Radio Science Meeting*, San Diego, CA, USA, July 2017,

[2] S. Das, D. J. Sawyer, N. Diamanti, A. P. Annan, and A. K. Iyer, "Design of strongly miniaturized, inherently matched, and scalable folded dipole antennas," presented in

the Special Session: Low-Profile Antennas from Gigahertz to Terahertz at the *USNC-URSI National Radio Science Meeting*, Boulder, CO, USA, January 2019.

Additionally, the contents of Chapter 4 have been communicated as:

[3] S. Das, D. J. Sawyer, N. Diamanti, A. P. Annan, and A. K. Iyer, "A strongly miniaturized and inherently matched folded dipole antenna for narrowband applications," under fourth round of review in *IEEE Transactions on Antennas and Propagation*, 2019.

The contents of Section 5.3 were performed in collaboration with Hossein Saghlatoon, a Ph.D. student of Prof. P. Mousavi of the University of Alberta, Canada. Hossein provided me with the required specifications and also helped me in the measurements. The work has been published as:

[4] S. Das, H. Saghlatoon, P. Mousavi, and A. K. Iyer, "A highly miniaturized and inherently conjugately matched folded dipole-based RFID tag antenna," *IEEE Access*, vol. 7, pp. 101658-101664, July 2019.

Acknowledgments

First of all, I would like to extend my gratitude to my supervisor, Prof. Ashwin K. Iyer, for his continuous guidance, motivation and support during my Ph.D. studies. I would always admire his immense knowledge on the subject and his dedication to the truth and the truth only, no matter what. Ph.D. is a difficult journey, and things do not always go as planned. But I will remember how he encouraged me from time to time asking whether I have learnt anything new. Thank you for not giving up on me, I will forever be indebted for that.

Second, I would like to thank all my fellow colleagues – Justin, Stuart, Linh, Elham, Ian, Hailey, David, Braden, Mitchell, Jacob and Christopher – for all the valuable academic and non-academic discussions we had, and also for their assistance in the simulations, experiments and writings in different phases of this research. Special thanks to Justin, who introduced me to the anechoic chamber; Stuart, who not only helped me learn HFSS better, but also helped me in preparing this thesis and brought me into extra-curricular activities like swimming and driving; and finally Elham, who helped me throughout in filling out numerous application forms during all these years. It had been a real privilege to become a part of this amazing group and have such wonderful people as friends.

I would not have made it this far without the love and support from my parents, my sister Debarati and her husband – my big brother Chinmoy. I would also like to take the opportunity to mention about two very close friends of mine – Tom and Sabreen – I am really grateful for all the talks and support during my difficult times.

I would also like to thank my collaborators, Dr. Nectaria Diamanti and Dr. A. Peter Annan from Sensors and Software, for providing their valuable expertise and insight on various practical issues during the course of this research. I would like to acknowledge the financial support provided by the Natural Sciences and Engineering Research Council (NSERC) of Canada through a Collaborative Research and Development (CRD) grant with Sensors and Software, graduate fellowship from Alberta Innovates and IEEE Antennas and Propagation Society, the simulation tools provided by CMC Microsystems, surface-mount inductor samples supplied by Coilcraft Inc., and the RFID chip samples provided by Alien Technology.

Last but not the least, I would like to conclude by thanking my former supervisors, Prof. Debatosh Guha and Dr. Jawad Y. Siddiqui for inspiring me to get into Ph.D. studies, and Prof. Guha for the opportunity.

Contents

List of Tables

List of Figures

List of Symbols

l	Length of the Folded Dipole Antenna
s	Separation between Folded Dipole Arms
λ	Wavelength
ω	Angular Frequency
λ_g	Guided Wavelength
f_R	Half-Wavelength Resonance
$f_{AR,1}$	First Antiresonance of the Folded Dipole Antenna
$f_{AR,2}$	Second Antiresonance of the Folded Dipole Antenna
$f_{R,N}$	New Resonance of the Folded Dipole Antenna
f_{AR}	One-Wavelength Antiresonance of the Conventional Dipole Antenna
I_{TLM}	Transmission Line Mode Current
Z_{TLM}	Transmission Line Mode Input Impedance
I_{AM}	Antenna Line Mode Current
Z_{AM}	Antenna Line Mode Input Impedance
Z_0	Characteristic Impedance of CPS Transmission Line
β	Propagation Constant
a_{eff}	Effective Cross-Sectional Radius of Equivalent Cylindrical Dipole
w	Width of Each Arm of a Folded Dipole Antenna
$Si(x)$	Sine Integral
$Ci(x)$	Cosine Integral

$Z_{in,FD}$	Overall Input Impedance of the Folded Dipole Antenna
ε_r	Relative Permittivity
ε_{eff}	Effective Relative Permittivity
X_{load}	Loading Reactance
L	Loading Inductance
C	Loading Capacitance
Z_{du}	Self-Impedance of the Unloaded Equivalent Cylindrical Conventional Dipole
w_{fd}	Width of Folded Arm
w_{fd}	Width of Driven Arm
S_{11}	Reflection Coefficient
C_g	Gap Width of Interdigitated Capacitor
C_l	Finger Length of Interdigitated Capacitor
C_w	Finger Width of Interdigitated Capacitor
Q_{ind}	Quality Factor of the Loading Inductor
$\eta_{rad,O}$	Overall Radiation Efficiency
$\eta_{rad,A}$	Radiation Efficiency of the Antenna
η_F	Feed Efficiency
l_p	Length of Perpendicular Sections for Adjusting Loading Inductance
w_p	Width of Perpendicular Sections for Adjusting Loading Inductance
L_w	Trace Width of the Meandered Inductor
L_g	Separation between two Traces of the Meandered Inductor
N	Number of Turns of the Meandered Inductor
Z_a	Input Impedance of the RFID Tag Antenna
Z_{ic}	Input Impedance of the RFID IC Chip
P_{ic}	Wake-up Power of the RFID IC Chip
τ	Antenna-IC Power Transfer Efficiency of the RFID Tag Antenna

d_{tag}	Read Range of the RFID Tag Antenna
$d_{tag,meas}$	Measured Read Range of the RFID Tag Antenna
$d_{tag,scaled}$	Scaled and Measured Read Range of the RFID Tag Antenna
χ_{pol}	Polarization Mismatch Factor of the RFID Tag Antenna
$G_{r,tag}$	Realized Gain of the RFID Tag Antenna
D_{tag}	Directivity of the RFID Tag Antenna
$\eta_{r,tag}$	Radiation Efficiency of the RFID Tag Antenna
P_{in}	Input Power to the Feed
$\Gamma_{in,F}$	Reflection Coefficient at the Input of the Feed
$P_{acc,F}$	Power Accepted to the Feed
$P_{out,F}$	Output Power from the Feed
$P_{acc,A}$	Input Power to the Antenna
$S_{11,A}$	Reflection Coefficient of the Antenna
$S_{11,F}$	Input Reflection Coefficient of the Feed
$S_{22,F}$	Output Reflection Coefficient of the Feed
$S_{21,F}$	Input-to-Output Transmission Coefficient of the Feed
$S_{12,F}$	Output-to-Input Transmission Coefficient of the Feed
k	Wave Number
a	Radius of the Smallest Circumscribing Sphere of an Antenna
Q_{ant}	Quality Factor of an Antenna
$Q_{ant,min}$	Minimum Quality Factor of an Antenna
FBW_V	Fractional Bandwidth Corresponding to a Specified VSWR Level
$FBW_{V,max}$	Maximum Fractional Bandwidth Corresponding to a Specified VSWR Level
σ	VSWR Level

List of Acronyms

RF	Radio Frequency
MF	Medium Frequency
HF	High Frequency
VHF	Very High Frequency
UHF	Ultra High Frequency
SHF	Super High Frequency
ISM	Industrial, Scientific and Medical
NRI-TL	Negative Refractive Index-Transmission Line
CRLH TL	Composite Right/Left-Handed Transmission Line
ENG	Epsilon Negative
MNG	Mu Negative
SRR	Split Ring Resonator
CLL	Capacitively Loaded Loop
IF	Inverted-F
Op-Amp	Operational Amplifier
TLM	Transmission Line Mode
AM	Antenna Mode
EMF	Electromotive Force
MATLAB	Matrix Laboratory
CPS	Co-Planar Stripline

FEM	Finite Element Method
HFSS	High Frequency Structure Simulator
MMCX	Micro-Miniature Coaxial
ADS	Advanced Design System
Balun	Balanced to Unbalanced
SPICE	Simulation Program with Integrated Circuit Emphasis
PNA	Performance Network Analyzer
M2M	Machine-to-Machine
IoT	Internet of Things
BAN	Body-Area Network
RFID	Radio Frequency Identification
IC	Integrated Circuit
EIRP	Equivalent Isotropic Radiated Power
RHCP	Right Hand Circular Polarization
ESA	Electrically Small Antenna
VSWR	Voltage Standing Wave Ratio
FBW	Fractional Bandwidth

Chapter 1

Introduction

1.1 Motivation

In recent years, there has been an increasing demand for wireless transceiver systems that are compact and portable. With advancements in microwave and solid state technologies, there has been significant success in reducing the size of various Radio Frequency (RF) circuit elements and components inside a transmit/receive module. However, miniaturization of antennas, which are possibly the most important and often the largest components in a wireless system have always been a topic of conflicting interest, since the process of size reduction significantly degrades the bandwidth and the radiation efficiency of the antenna, thus affecting the performance of the whole system in the expense of portability.

The performance of an antenna is largely dependent on its electrical size, i.e., size with respect to wavelength, which is usually of the order of one-half of a wavelength, or sometimes a full wavelength. An antenna that is much smaller than this size, usually exhibits a small input resistance and large input reactance that makes it difficult to match to a practical source impedance, which in turn results in poor bandwidth and efficiency. External matching networks are often employed as a remedy, but not without increasing the overall size and complexity of the system, which defeats the purpose of miniaturization to some extent.

Thus, it remains an open challenge to realize a sufficiently small antenna with an adequate bandwidth and efficiency, such that the overall system performance is not affected.

The use of electrically small antennas goes a long way back to the late 1800s, when Edison used vertical top-loaded grounded antennas for a communication system, or Hertz performed his groundbreaking spark-gap experiments, and in the early 1900s, when Marconi performed his trans-Atlantic communication using fan-shaped monopole [1]. Antenna technology experienced a remarkable development during the two World Wars, which essentially paved the way for smaller-sized wireless communication systems. In that pursuit, the operating frequency has also been gradually raised from MF and HF band to VHF, UHF and SHF band in the recent years. Apart from broadcasting and mobile communications, electrically small antennas have been employed extensively in sensing/monitoring applications, some examples of which include Machine-to-Machine (M2M) communications, Internet of Things (IoT), Radio-Frequency Identification (RFID), biomedical implants, and various other body-centric sensor systems. These systems usually transmit/receive a small amount of data over a relatively short distance, and thus do not require a wide bandwidth and/or a high radiation efficiency.

Dipole and folded dipole antennas, along with their monopole equivalents, are often the preferred choice for many sensing applications, particularly because of their simplicity, low cost, compact size, well-defined radiation properties, omnidirectional coverage area and simple analysis and design, both in wire and printed forms. Although a folded dipole antenna has identical radiation characteristics as a conventional dipole antenna, it can be considered somewhat advantageous compared to its conventional counterpart for miniaturization purposes as its input impedance can be modified by making suitable structural changes, as will be disclosed in the latter chapters. Nevertheless, as mentioned earlier, impedance matching can be a major issue for both miniaturized conventional and folded dipole antennas. Having a well-matched antenna for sensing purposes is important, as it will radiate more power for a given radiation efficiency, and hence a longer detection range can be realized.

Again, the impedance matching problem is usually resolved by employing external matching networks, or sometimes increasing the footprint of the antenna itself in lateral directions (e.g., meander-line dipole/monopole antennas, folded dipole antennas with multiple arms). Furthermore, the source impedance of a sensor antenna can be either be real or complex (e.g., RFID tag). As a result, different kinds of matching network topologies are usually employed.

1.2 Objectives

A folded dipole antenna has been selected for this work owing to the aforementioned advantage over a conventional dipole antenna. Thus, the main objectives of this work are the following: (1) to develop a miniaturization technique for folded dipole antennas by employing a simple reactive loading topology, such that good matching can be obtained with respect to an arbitrary real source impedance for a given level of miniaturization, without using any external matching network or having to alter the antenna structure greatly, (2) extend the matching technique for sensor antennas requiring matching to complex input impedances, and finally (3) experimentally validate both miniaturization techniques.

1.3 Outline

Chapter 2 provides a detailed account of the different approaches for miniaturizing conventional and folded dipole antennas, along with the corresponding matching techniques.

In Chapter 3, the well-known analytical model of a folded dipole antenna is extended in order to include the effects of a symmetric reactive loading scheme applied to the antenna, and the conditions crucial for achieving good matching at a given miniaturization level are discussed. Furthermore, it is demonstrated that an asymmetric loading scheme will result in easily realizable loading reactance values compared to a symmetric loading scheme, and it is also discussed why the analytical model is unable to account for the introduced asymmetries.

Chapter 4 demonstrates an example of a folded dipole antenna that was miniaturized to 75% level following the conclusions drawn in Chapter 3. The radiation performance parameters of the miniaturized folded dipole antenna are compared to that of an equivalently loaded conventional dipole antenna. The miniaturized folded dipole antenna is validated using measurements.

In Chapter 5, a fully printed 75% miniaturized folded dipole antenna is designed for UHF ISM band of 902-928 MHz, which can be suitable for sensor applications where matching is required with respect to real input impedances. Following that, the design technique is extended in order to realize a RFID tag antenna that needs to be matched to a complex input impedance. Both the antennas are experimentally validated.

Finally, the thesis is concluded in Chapter 6, where a number of future directions of this research have been proposed.

Chapter 2

Background

2.1 Dipole Antennas

2.1.1 Introduction

A dipole antenna consists of a linear metallic conductor, which is usually split at the center and fed by a balanced transmission line that carries equal and opposite currents on its two conductors. These antennas, and their variants, are possibly the simplest, oldest and least expensive radio antennas that are still being used extensively as basic transmitters and receivers in various communication systems, broadcasting, measurements of electric fields, and as feeding elements of larger aperture-type antennas like horn or reflector antennas.

The current distribution on a dipole antenna can be explained easily with the help of a lossless two-conductor transmission line terminated in an open circuit [2]. Consider charges moving along the transmission-line conductors comprising a travelling wave current of magnitude $I_0/2$, which upon arriving at the open circuit goes through a complete reflection that results in a reflected travelling wave current of the same magnitude, but with a 180° reversed phase. The mechanism is shown in Fig. 2.1(a). Thus, the reflected travelling wave after being combined with the incident travelling wave, creates a sinusoidal standing wave pattern of magnitude I_0 on the two conductors of the transmission line. Although the individual

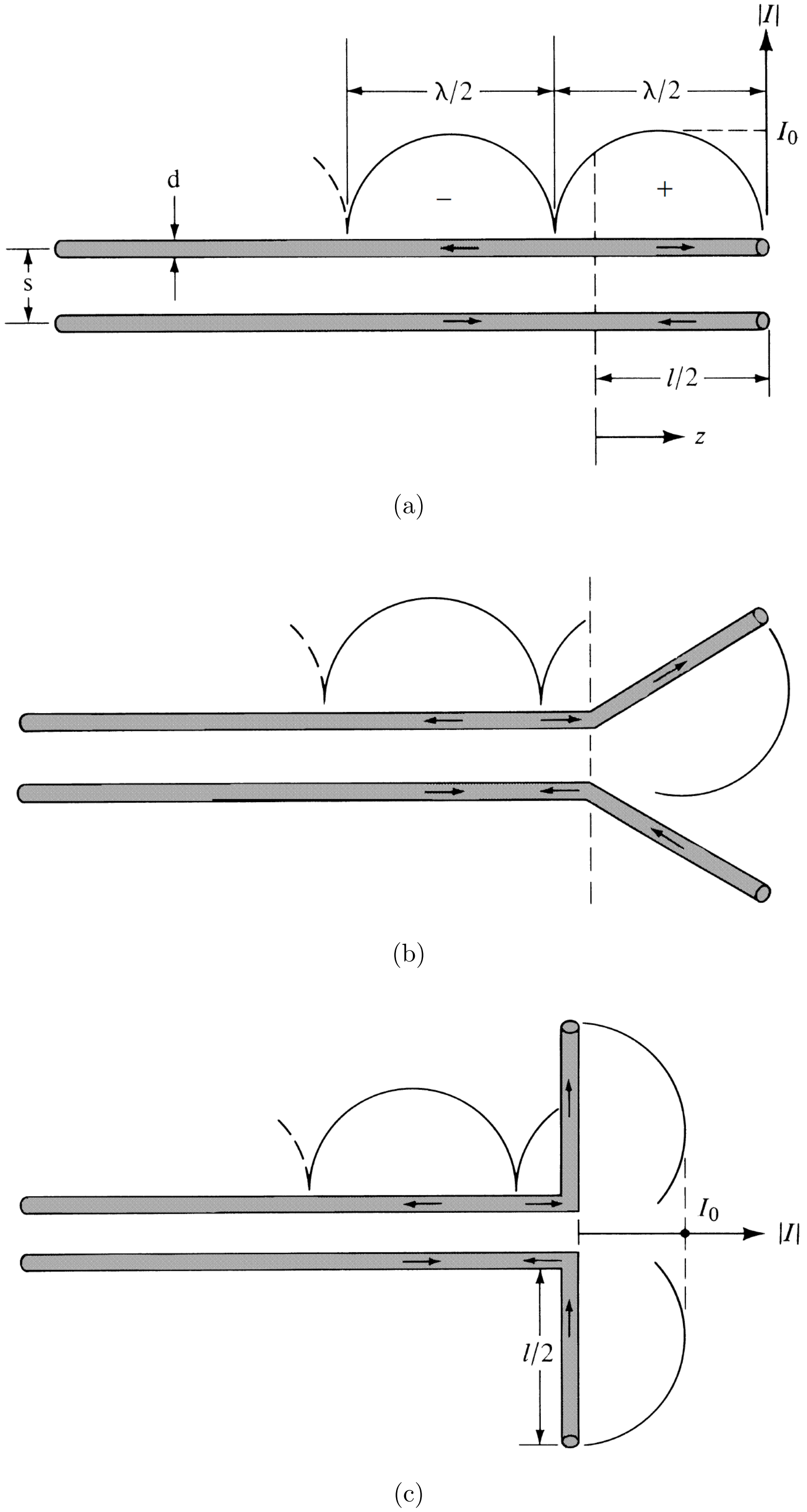

Figure 2.1: Current distributions on (a) lossless two-conductor transmission line, (b) flared transmission line, and (c) linear dipole antenna [2].

conductors of the transmission line radiate due to the time-varying nature of the currents, since the spacing between them is usually considered much smaller than the wavelength ($s \ll \lambda$) the two radiated fields essentially cancel each other, thus producing no overall radiation. Now, if the two conductors at the end of the transmission line begin to flare apart from each other as shown in Fig. 2.1(b), then for the same current distribution, the two radiated fields will not completely cancel each other anymore. An extreme case of this flaring can be seen in Fig. 2.1(c), where the flared sections are at a perfect right angle with the remaining transmission-line section. This essentially represents a linear dipole antenna. Now, if the total length of the flared section is smaller than a wavelength ($l < \lambda$), then the standing wave currents on each of the flared segments is co-directed throughout the length, and the corresponding radiated fields from each of these currents will reinforce each other. The open circuits at the ends basically form the boundary conditions for the dipole antenna. The most commonly used dipole antennas are a half-wavelength long ($l = \lambda/2$), where the dipole antenna undergoes its first resonance and exhibits only a real input impedance. At all lengths $l < \lambda$, a center-fed dipole antenna radiates in an omnidirectional pattern with a linear polarization parallel to the length of the dipole. A representative diagram of a half-wavelength long dipole antenna along with its omnidirectional radiation pattern is shown in Fig. 2.2. For lengths $l > \lambda$, the currents on the different parts of the dipole antenna will not be co-directed anymore, thus the fields radiated by the antenna will experience constructive and destructive interferences, which in turn will produce a diffraction pattern including sidelobes and nulls.

Another equivalent form of the dipole antenna is the monopole antenna, which is realized by placing half of the dipole antenna perpendicularly in the vicinity of an infinite and perfectly conducting surface, often termed as the ground plane. Since a monopole antenna is more compact compared to its dipole equivalent, it is one of the most widely used antennas in the handheld units of mobile communication systems [3,4]. The image formed by the ground plane acts as a substitute for the remaining half of the dipole, in that the induced currents on

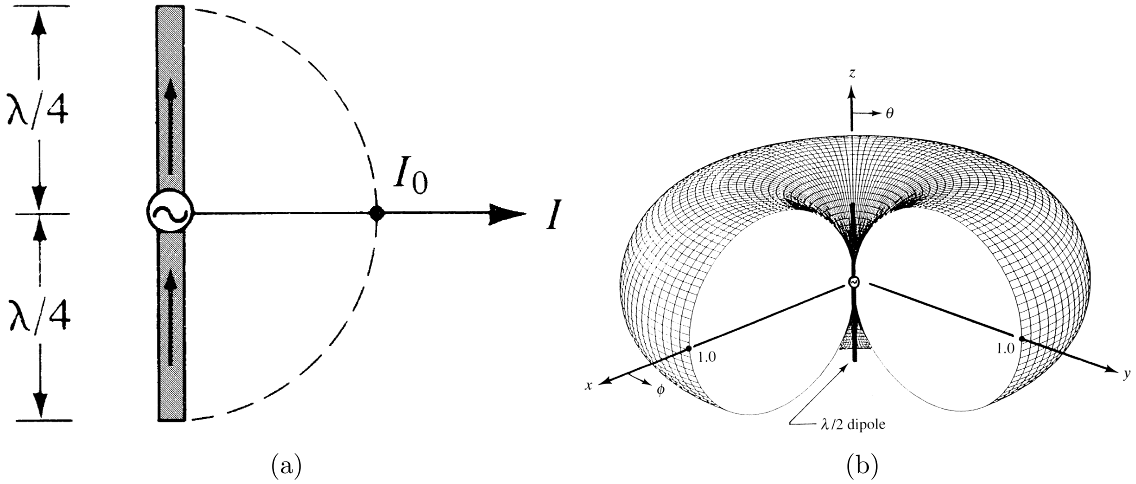

Figure 2.2: (a) Half-wavelength dipole antenna, and (b) its omnidirectional radiation pattern [2].

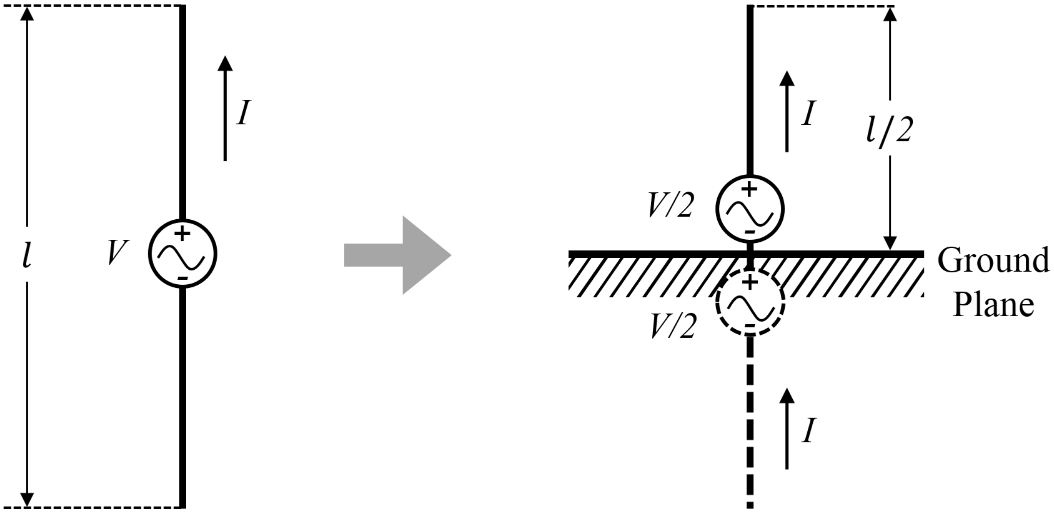

Figure 2.3: Schematic of a monopole antenna.

the ground plane produce the corresponding fields in the upper half-space. Thus, the most commonly used monopole antennas are a quarter-wavelength ($\lambda/4$) long, and exhibit a similar omnidirectional pattern. A representative monopole antenna has been shown in Fig. 2.3. The input impedance of a monopole antenna is half of the equivalent dipole antenna, since only half of the input voltage is required to produce the same amount of current. Similarly, since only half of the input power of the dipole is needed to produce the same field strengths, the gain of a monopole antenna is usually double compared to that of the dipole. However, although monopole antennas have a more compact size and better gain compared to their dipole counterparts, they still require a large ground plane, and since an infinite perfectly conducting ground plane is practically not realizable, the radiation pattern and the gain are usually affected by the finiteness of both the ground plane size and conductivity [5, 6].

2.1.2 Miniaturization Techniques

The recent advances in wireless and solid state technologies have made the realization of high-performance miniaturized transmit and receive modules a reality, which have found widespread use in different industrial, medical, and military applications. This led to a requirement for components that are compact and efficient at the same time. In order to meet these ever-increasing space constraints, the size of the constituent active circuit elements and RF components inside a wireless system has been reduced notably. However, although there have been significant efforts towards miniaturization of antennas that are often the largest components in a wireless system, the challenge remains to realize a sufficiently small antenna with an adequate bandwidth and radiation efficiency, the reason behind which is the small input resistance and large input reactance exhibited by the electrically small antennas. Thus, these antennas generally require an external matching network that can provide conjugate matching, such that maximum power transfer can be ensured from the rest of the wireless system to the antenna. However, these matching networks often increase the size and complexity of the system.

Once again, dipole and monopole antennas are among the preferred choices for several compact antenna applications, particularly because of their simplicity, compact size, well-defined radiation properties and simple design and analysis; in both wire and printed forms. In this section, different miniaturization techniques of these antennas will be discussed.

2.1.2.1 Reactive Loading

Electrically small dipole antennas are inherently capacitive, thus the simplest method for miniaturizing a dipole antenna is to load it with a series inductor. The series inductive loading essentially shifts the half-wavelength-like resonance of the dipole antenna to a lower frequency, where the physical length of the antenna is smaller than the corresponding half-wavelength. Many examples can be found in the literature, where inductive loading has been applied to a dipole and monopole antenna using various inductor topologies with the sole objective of increasing the length of the antenna within a compact form. Possibly the first reported work on loaded monopoles was done by Bulgerin and Walters in 1954, who performed a series of experiments on short fat monopoles of different lengths at 100 MHz [7]. Followed by that, Harrison performed a study on the effect of loading position on the radiation efficiency using a coil loaded monopole antenna [8], a schematic of which is shown in Fig. 2.4. The results showed that the efficiency increases gradually as the loading point is moved away from the feed and towards the end of the antenna, but the data are only available up to 2/3 loading point, i.e., $2/3^{rd}$ distance from the feed to the end ($|h_2| = 2|h_1|/3$ in Fig. 2.4). However, later in 1975, Hansen showed using moment-method calculations on a similar problem that the maximum radiation efficiency occurs at roughly 0.4 loading point ($|h_2| = 0.4|h_1|$ in Fig. 2.4), and falls off slowly as the loading point is moved towards the end [9, 10]. But, he also showed that the input resistance keeps on increasing as the loading point is moved all the way to the end, which is essential for obtaining good impedance matching. Thus, he proposed that the $2/3^{rd}$ loading point can be regarded as a good compromise between achieving high radiation efficiency and large input resistance.

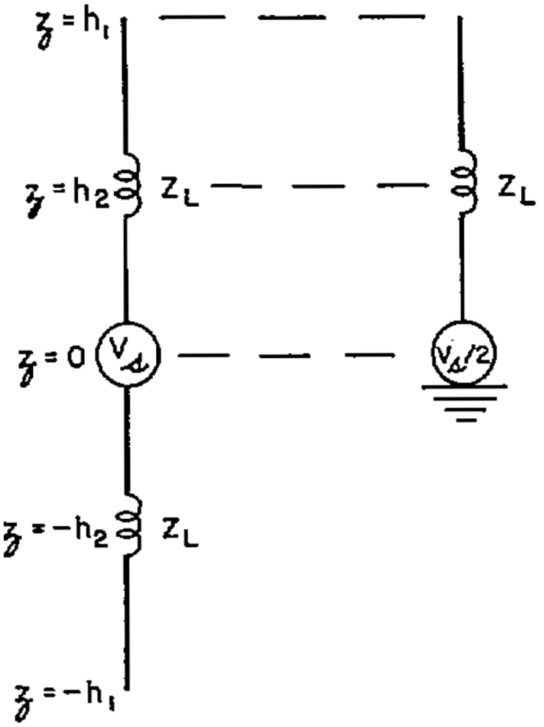

Figure 2.4: Series inductively loaded dipole and monopole antenna [8].

These kinds of coil-loaded monopole antennas are traditionally called whip antennas and have been used extensively for vehicular communication systems. Some other examples of coil loaded whip antennas can be found in [11, 12]. Moreover, instead of using a localized coil for providing inductive loading, distributed inductive loading was also employed in some of the whip antennas, where the monopoles were essentially constructed using a helix with a tapered pitch [13, 14]. Miniaturized dipole/monopole antennas have also been realized using other distributed inductive loading topologies, e.g., using meandered arm [15–19], zigzag arm [20], sinusoidal arm [21], rolled dipole arms [22] etc. Several of these distributed inductively loaded small antennas are shown in Fig. 2.5.

Another method of miniaturizing a dipole/monopole antenna is to load it with a shunt capacitor, which is typically done by placing a conducting disk at the ends of the antenna. This loading scheme is also known as top-loading. The use of top-loaded dipole antenna dates back to the late 1800s, when in 1875 Edison patented a communication system using vertical, top-loaded grounded antennas [1], or when Hertz performed his famous spark gap experiment

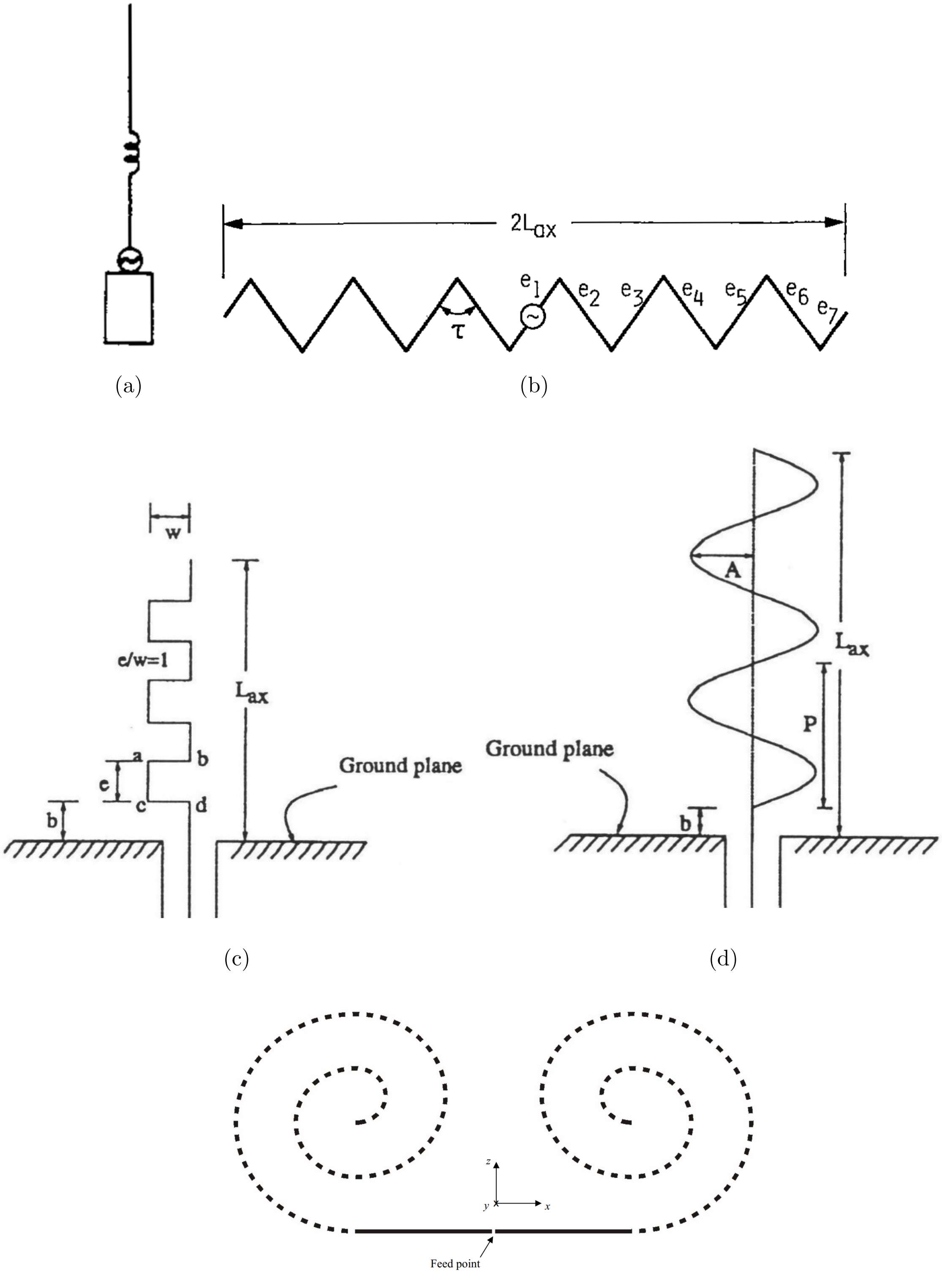

(a) (b) (c) (d) (e)

Figure 2.5: Series inductive loading topologies: (a) coil loaded whip antenna [11], (b) zigzag dipole antenna [20], (c) meandered monopole antenna [21], (d) sinusoidal monopole antenna [21], and (e) rolled dipole antenna [22].

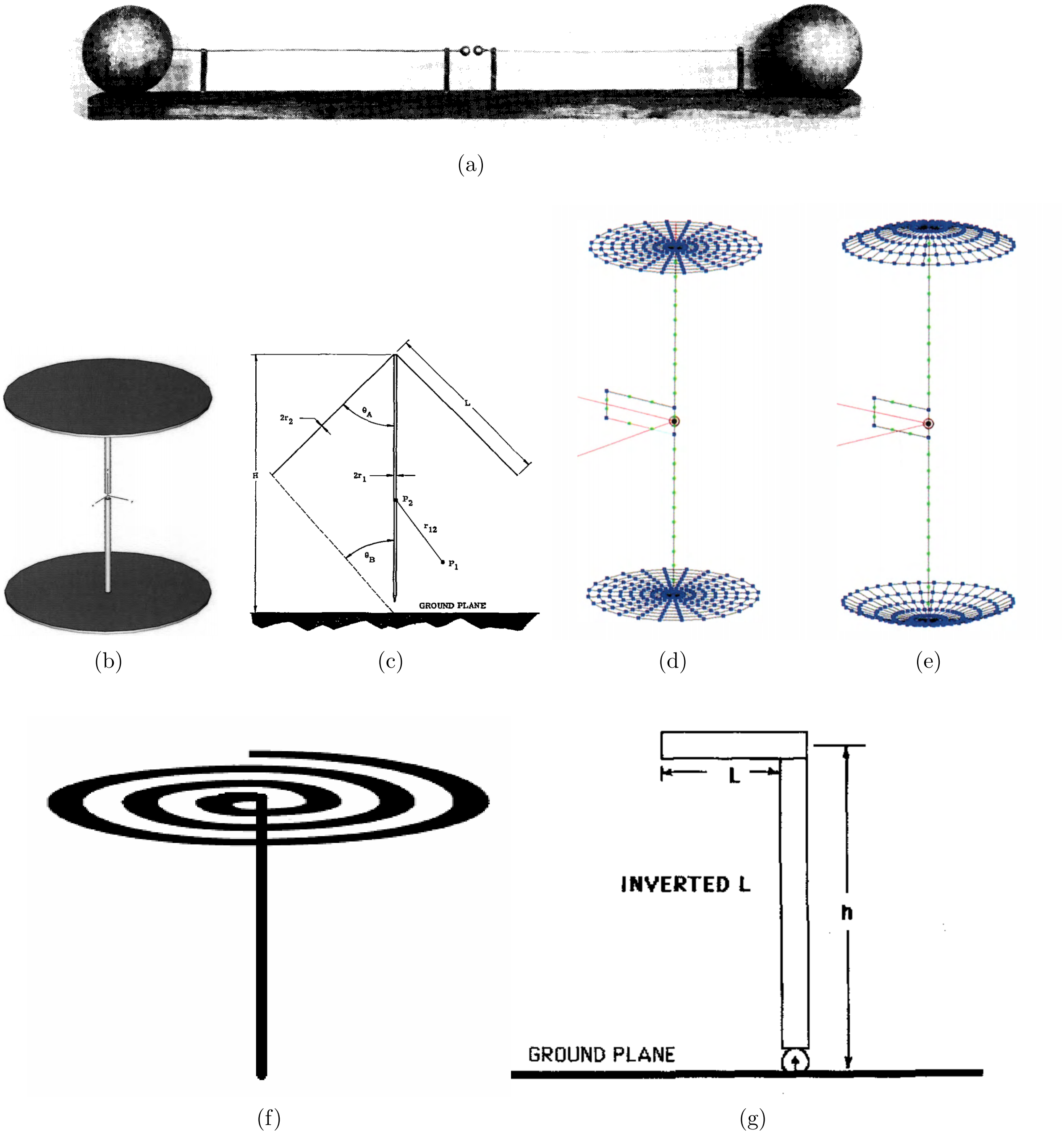

(a)

(b) (c) (d) (e)

(f) (g)

Figure 2.6: Shunt capacitive loading topologies: (a) spherical top loading used by Hertz [23], (b) solid disk-loaded dipole antenna [30], (c) umbrella-shaped top loading [29], (d) wire-grid disk type top-loading [30], (e) wire-grid spherical cap type top-loading [30], (f) spiral coil type top-loading [31], and (g) inverted-L monopole antenna [33].

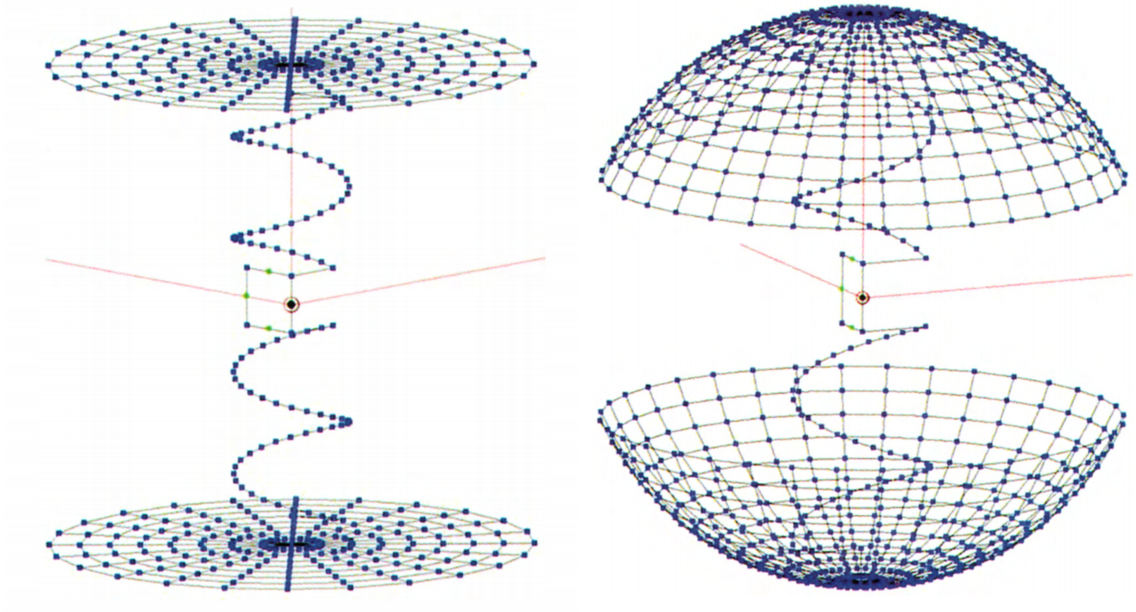
(a) (b)

Figure 2.7: Combination of series inductive and shunt capacitive loading topologies: (a) wire-grid disk type top-loading on a helical dipole [30], (b) wire-grid spherical cap type top-loading on a helical dipole [30].

using a dipole with sliding capacitive spheres between 1886 and 1889 [1,23]. The top-loading arrangement changes the boundary condition for the antenna current at the ends, and since the currents no longer have to go to zero at the ends, the overall current profile becomes more uniform over the dipole length, thus resulting in an enhanced radiation efficiency and bandwidth [24,25]. In this approach, the degree of miniaturization depends on the size of the loading disks, however at the price of increased dimension in the lateral directions. Various shapes were used for realizing top-loading, some typical examples include thin circular plate or disk [26, 27], umbrella-shaped loading [28, 29], wire-grid disk or spherical-cap [30], spiral coil [31], or inverted-L shaped top-loading [32, 33]. Some of these top-loading topologies are shown in Fig. 2.6. Furthermore, top-loading can also be used in conjunction with distributed series inductive loading in order to realize miniaturized dipoles, as shown in Fig. 2.7 [30].

2.1.2.2 Metamaterial Loading

More recently, metamaterial technology has been exploited for realizing electrically small dipole-like antennas. Metamaterials or left-handed materials are artificially engineered materials with unusual properties like negative permittivity or permeability that are not readily available in nature. Particularly important for antenna miniaturization are the transmission-line metamaterials, where the aforementioned exotic properties can be achieved by loading a regular or right-handed transmission line periodically using series capacitance and shunt inductances, with each period (also known as unit cell) being much smaller than the guided wavelength, which is essentially the Bloch wavelength of the periodic structure, in order to realize an effective homogeneous medium [34, 35]. These kinds of loaded transmission lines are called Negative Refractive Index Transmission Lines (NRI-TLs) or Composite Right/Left-Handed Transmission Lines (CRLH TLs).

The guided wavelength (λ_g) in a NRI-TL is dominated by the capacitors and inductors that load the underlying transmission line, whereas the wavelength in a right-handed transmission line is essentially determined by its filling medium. Thus, the required condition for creating a standing wave resonance on such a transmission line of length L is given as:

$$L = |n|\frac{\lambda_g}{2} \quad ; \quad n = 0, \pm 1, \pm 2 \; ... \tag{2.1}$$

where n is the resonance number. Of particular importance for miniaturization of dipole antennas are the zeroth order resonance ($n = 0$) and the half-wavelength resonances ($n = \pm 1$). The field distribution for a zeroth order resonance is flat, and thus not related to the physical length of the transmission line, which suggests that in principle, it can be used for realizing arbitrarily small antenna sizes. On the other hand, the half-wavelength resonances can be used for multiband operation by choosing the number of unit cells, and miniaturization can be attained by properly choosing the loading reactance values. Finally, a zeroth order resonant antenna will exhibit a higher radiation efficiency compared to the

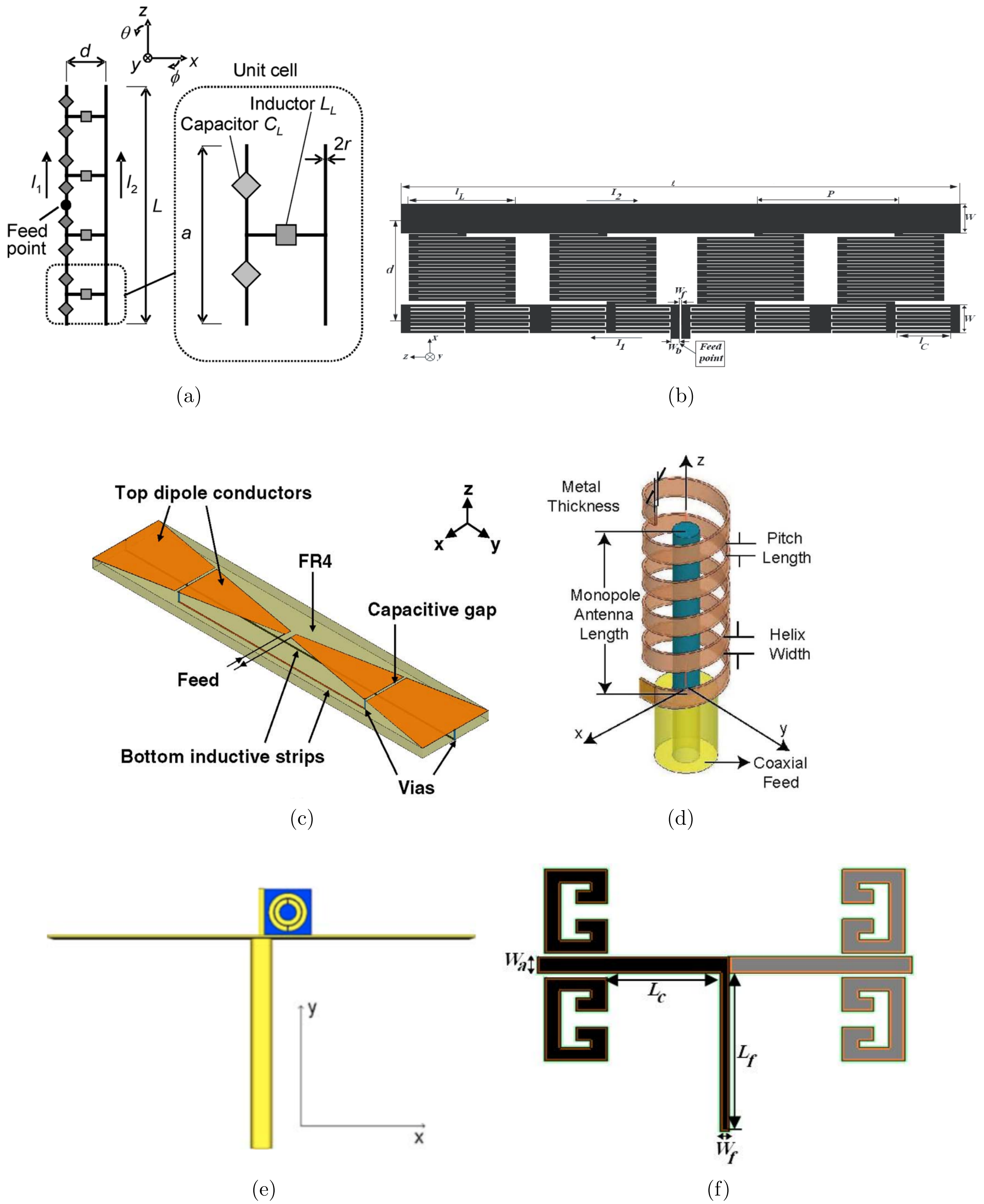

(a) (b)

(c) (d)

(e) (f)

Figure 2.8: Metamaterial loaded dipole/monopole antenna topologies: (a) Transmission line metamaterial loaded [36], (b) CRLH loaded [39], (c) NRI-TL loaded bowtie antenna [40], (d) small monopole surrounded by an ENG-like medium [42], (e) SRR loaded [43], and (f) CLL loaded [44].

half-wavelength resonant antennas due to its higher uniformity of fields along the structure. Examples of various transmission line metamaterial loaded miniaturized dipole antennas can be found in [36–40].

In another approach, an electrically-small dipole antenna was surrounded with negative permittivity (epsilon-negative or ENG) material that acts as an appropriate parasitic element in order to achieve good matching and efficiency [41, 42]. Alternatively, a monopole antenna can be loaded with a split-ring resonator (SRR) that is a negative-permeability element (mu-negative or MNG). The operating frequency of the composite structure is determined by the resonance frequency of the SRR, which can be easily made to resonate at a lower frequency than the monopoles own resonance frequency, thus resulting in miniaturization [43]. Furthermore, a dipole can be loaded with capacitively loaded loops (CLL), where again the resonance frequency of the CLL influences the operating frequency of the composite structure, which can be lowered by increasing the overall capacitance of the CLL by using surface-mount chip capacitors [44]. The various metamaterial loading techniques described in this section are shown in Fig. 2.8.

2.1.2.3 Other Techniques

One way to make monopole antennas more compact is by realizing them in Inverted-F (IF) form; although they are typically quarter-wavelength-long antennas, compactness is achieved by bending them and making them parallel to the ground plane [45], as shown in Fig. 2.9(a). It is shorted at one end close to the feed point. IF antennas radiate in an omnidirectional pattern and the input impedance can be adjusted by changing the feeding location on the antenna, thereby facilitating matching. These kinds of antennas can be made to radiate in multiple frequency bands by inserting additional stubs/slots [46–48], and also can be further miniaturized by meandering and folding the conductor [49–51], parallel capacitive loading [52, 53], or by applying Composite Right/LeftHanded (CRLH) metamaterials [54, 55]. Some of these IF antennas are shown in Figs. 2.9(b)-2.9(e).

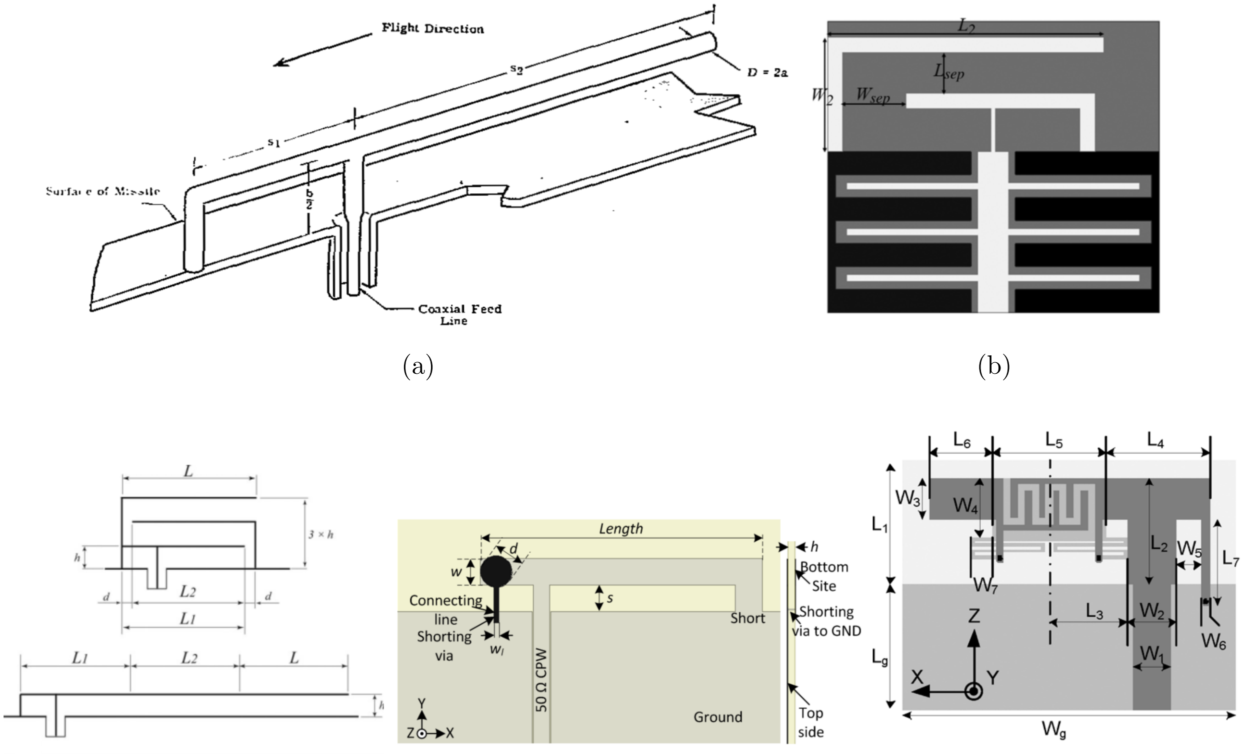

(a) (b)

(c) (d) (e)

Figure 2.9: IF antenna topologies: (a) unloaded [45], (b) slot loaded [47], (c) meandered and folded IF antenna [50], (d) capacitively loaded [53], and (e) CRLH loaded [54].

Furthermore, attempts have been made to miniaturize a dipole antenna by loading it with high-permittivity and high-permeability materials [56–60]. However, a dipole with series inductive loading usually results in a better efficiency and bandwidth [61].

2.1.3 Matching Techniques

As mentioned earlier, one of the major challenges involving small-antenna design is to match the antenna to a practical source impedance. For most of the cases, this requires including an external matching network, which again increases the size and complexity of the antenna structure, thus somewhat defeating the purpose of miniaturization. Another potential challenge in introducing an external matching network is that the loss resistances within the matching-network components may result in an overall low efficiency. However, the introduced loss may also help to increase the operating bandwidth of the antenna. Thus, introduction of a lossy matching network can be an acceptable tradeoff between achieving wider bandwidth and an adequate radiation efficiency, depending on the particular application [30].

Rather than employing an external matching network, the antenna structure can also be modified in order to achieve a higher input resistance at the miniaturized resonance. Some of these techniques have been already mentioned in the previous sub-sections, such as distributed-inductor loading, top-hat loading, and metamaterial loading. Whereas it is possible to achieve the required input resistance in order to facilitate matching for the reactively loaded dipole antennas either by increasing meandering or by increasing the top-hat dimensions, it usually results in a reduced radiation efficiency due to the increased conductor losses. Furthermore, these modifications also increase the antenna dimension in lateral directions. On the other hand, transmission-line-metamaterial loaded antennas usually suffer from poor efficiency mainly due to the oppositely-directed transmission-line-like currents flowing on the structure [36, 39, 40].

Matching networks used for electrically small antennas are typically of two kinds: (1) Foster matching networks, and (2) Non-Foster matching networks. Foster matching networks are basically composed of passive elements like inductors, capacitors or transmission-line sections. Although ideally lossless, practical implementations of these elements can have some physical losses, thus the matching networks constructed using these elements might affect the radiation efficiency of the miniaturized antenna. Another drawback of these kinds of matching networks is their limited bandwidth. However, these networks are simple to design and easy to fabricate. Some typical examples of these networks include L, T, or π-sections that mostly use lumped reactive elements, single/double/triple stub matching networks that use transmission-line sections, single- and multi-stage quarter wave transformers, tapered transmission-line segments where the tapering is usually designed by employing binomial or Chebyshev polynomials, and finally T- and Gamma-type matches, where a smaller dipole is attached to the larger main dipole antenna and the corresponding dimension and separation

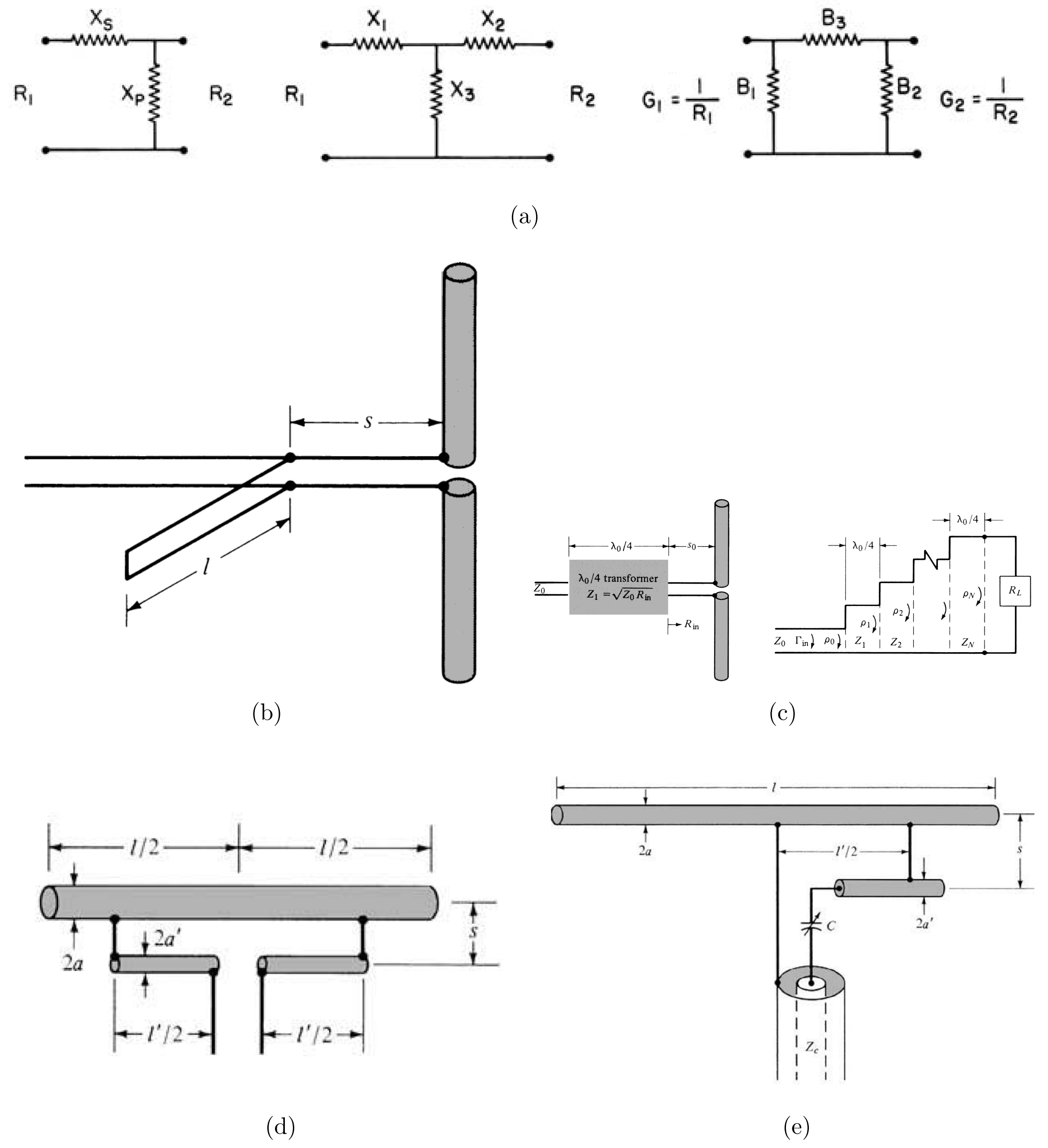

Figure 2.10: Foster matching network topologies: (a) L, T, and -sections [62], (b) stub matching [2], (c) single and multi-stage quarter wave transformers [2], (d) T-match [2], and (e) Gamma match [2].

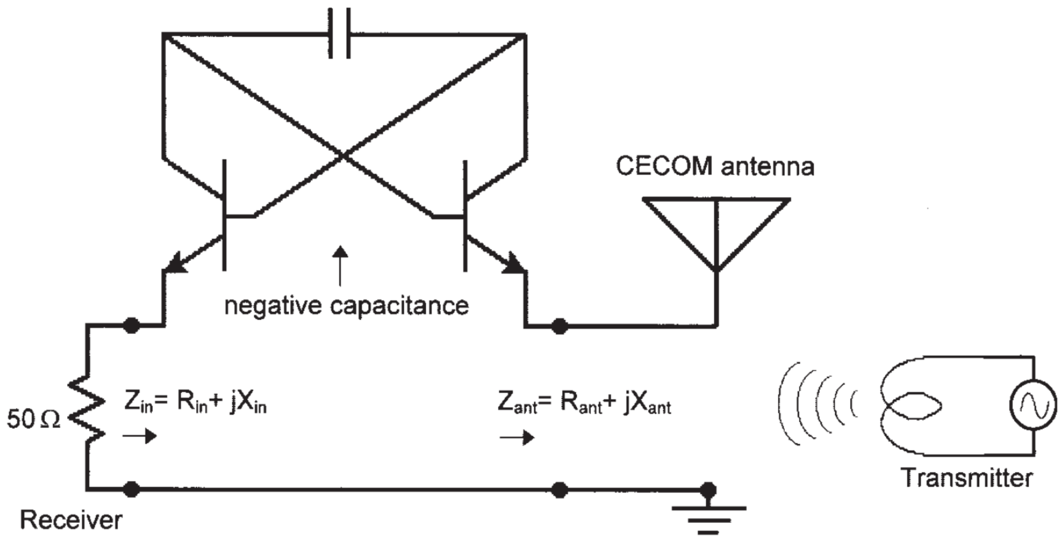

(a)

Figure 2.11: Non-Foster matching network using transistors [65].

are varied in order to achieve the required matching [2,62]. Some of these matching networks are shown in Fig. 2.10. The Non-Foster matching networks on the other hand employ active elements like Op-Amps and transistors in order to realize negative reactance and resistances that provide a wider bandwidth compared to the Foster matching networks and a better noise figure, respectively. However, as expected, these matching networks are much more complex and require external biasing sources for the active elements [61,63–65]. An example is shown in 2.11.

2.2 Folded Dipole Antennas

2.2.1 Introduction

A folded dipole antenna is constructed by joining two closely-spaced ($s \ll \lambda$) parallel dipoles of equal length at the ends, and feeding at the center of one of the dipoles. For the rest of this thesis, the fed arm will be called the “Driven” arm, and the other arm will be referred to as the “Folded” arm. Similar to a conventional dipole antenna, a folded

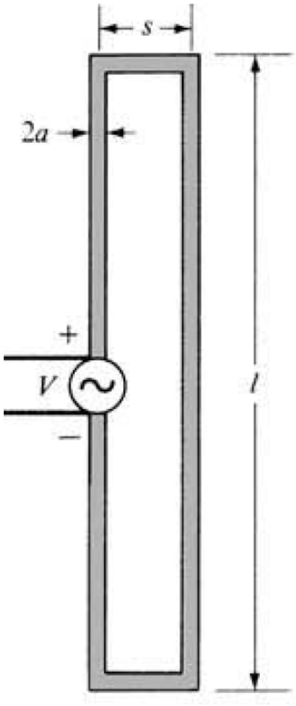

Figure 2.12: Schematic of a folded dipole antenna [2].

dipole antenna is typically operated at its half-wavelength frequency (i.e., when the overall length $l = \lambda/2$, and the total conductor length $\approx 2l = \lambda$), and it radiates in a similar omnidirectional pattern. At its half-wavelength resonance, the input impedance of a folded dipole antenna with two identical arms is four times greater than that of a conventional dipole antenna at resonance (i.e., $4 \times 73 = 292\ \Omega$), and thus it is usually fed by a balanced twin-lead transmission line that has a characteristic impedance of approximately 300 Ω. However, the input impedance of the antenna can be further modified either by employing multiple folded arms [2], or by making the cross-sectional dimensions of the driven and folded arms unequal [66]. Folded dipole antennas are used extensively as the driven element in a Yagi-Uda array and have applications in domestic television, VHF communications and FM broadcast antennas. A representative diagram of a two-arm folded dipole antenna has been shown in Fig. 2.12.

2.2.2 Miniaturization Techniques

Although not as widely studied as the conventional dipole antenna, miniaturization techniques for a folded dipole antenna are very similar to those of a conventional dipole antenna, owing to their structural and behavioral similarity. It should be noted that many of the following examples employ folded monopoles, which is essentially half of the folded dipole antenna placed vertically on a ground plane, with the driven arm being fed and the folded arm being shorted to the ground.

2.2.2.1 Reactive Loading

Once again, the simplest way to miniaturize a folded dipole antenna is to load it with series inductors. The loading can be done by placing lumped inductors on the folded dipole/monopole arms or by meandering the arms themselves [67–70]. One advantage of miniaturized folded dipole antennas is that since the input impedance is already high, the antennas exhibit sufficient amount of input resistance at their resonances even after miniaturization, thus making matching to a practical source impedance (e.g., 50 Ω) easier compared to a conventional dipole antenna.

Top-loading has also been used for realizing electrically small folded dipole antennas [71,72], where matching was realized by employing unequal cross-sectional dimensions of the two arms. Again, the top-loading was used simultaneously with meandered folded dipole arms for miniaturization in [68], where multiple folded arms were used to increase the input resistance of the antenna to improve both matching and radiation efficiency. A representative diagram containing various reactive loading techniques is given in Fig. 2.13.

2.2.2.2 Metamaterial Loading

Metamaterial technology has also been applied to the miniaturization of folded dipole antennas. Electrically small, but efficient folded antennas were realized by forcing the antenna arms to radiate in phase using metamaterial phase-shifting lines [73], or by zero-degree

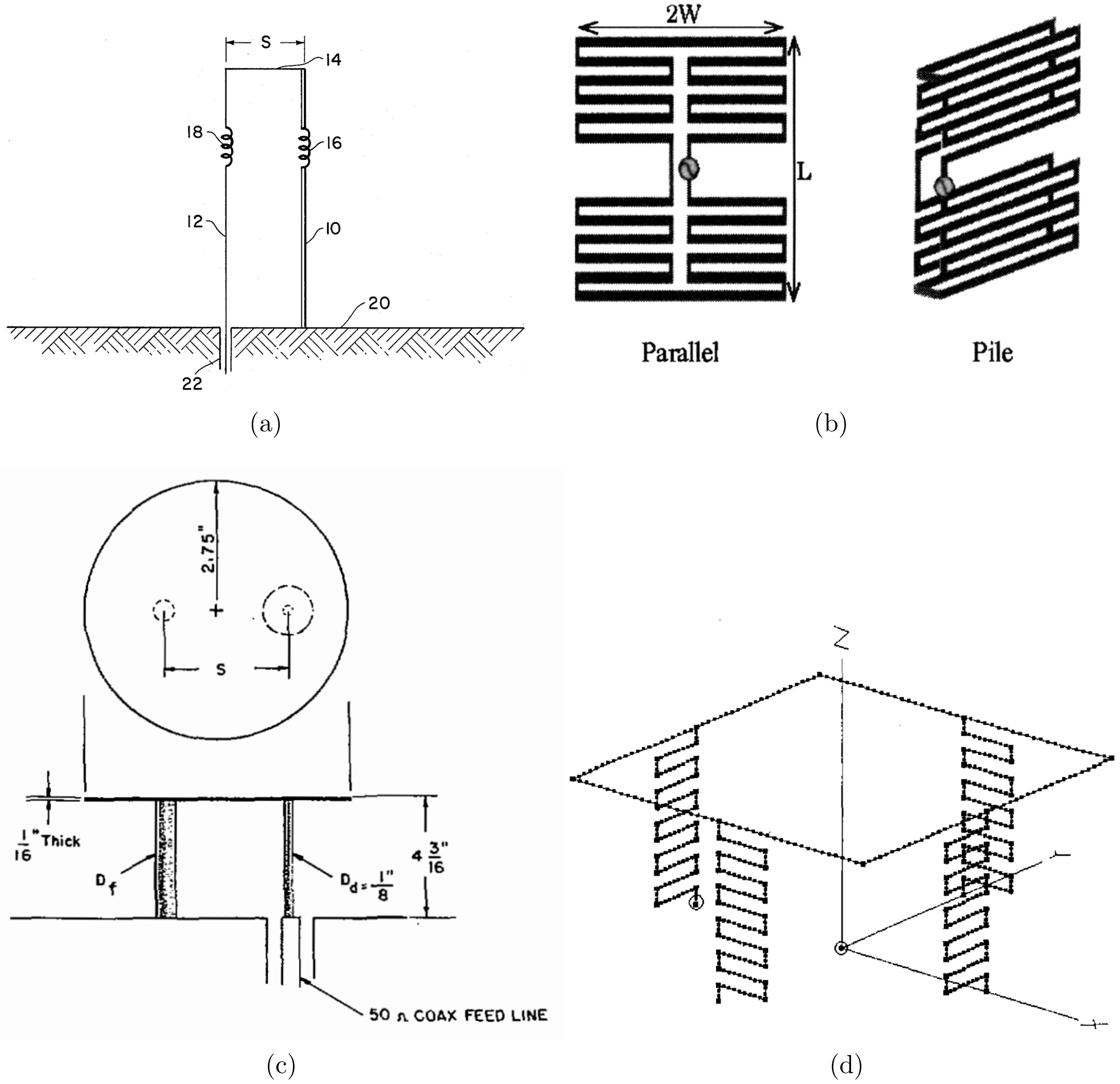

(a) (b)

(c) (d)

Figure 2.13: Reactively loaded folded dipole topologies: (a) series inductively loaded [67], (b) meandered folded dipole [69], (c) disk loaded [71], and (d) with both series inductive loading and shunt capacitive loading [68].

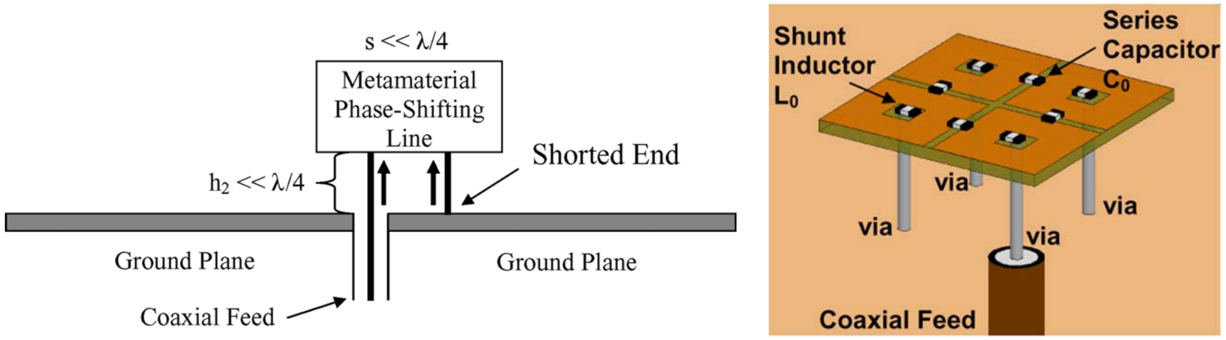

(a) (b)

Figure 2.14: Metamaterial loaded folded dipole topologies: (a) with metamaterial phase shifter [73], and (b) with NRI-TL π-type unit cell [74].

NRI-TL metamaterial unit cells [74].

In [73], the metamaterial phase-shifting lines provided the required phase, such that the current distribution over the folded monopole structure experiences a total of 180° phase shift, which is the required condition to simulate a quarter-wave long unloaded folded monopole that has co-directional currents on its two arms. The technique used in [74] is somewhat different. The design of the miniaturized folded dipole antenna was based on a symmetric NRI-TL π-type unit cell topology, mainly because of its resemblance to a folded monopole. The corresponding unit cell dimensions and the loading reactance values were chosen accordingly to ensure a 0° total phase over the unit cell. Then it was shown using the even-odd mode analysis that the even mode, i.e., the co-directed currents (radiating currents) overwhelm the odd mode, i.e., the contra-directed currents (non-radiating currents), which in turn resulted in a high radiation efficiency. The input resistance in this work was increased by employing multiple folded arms to facilitate matching. Both the structures are shown in Fig. 2.14.

2.2.2.3 Other Techniques

In an analogous approach to the work described in [73], conventional 180° phase shifters were employed to realize highly efficient but strongly miniaturized folded dipole antennas

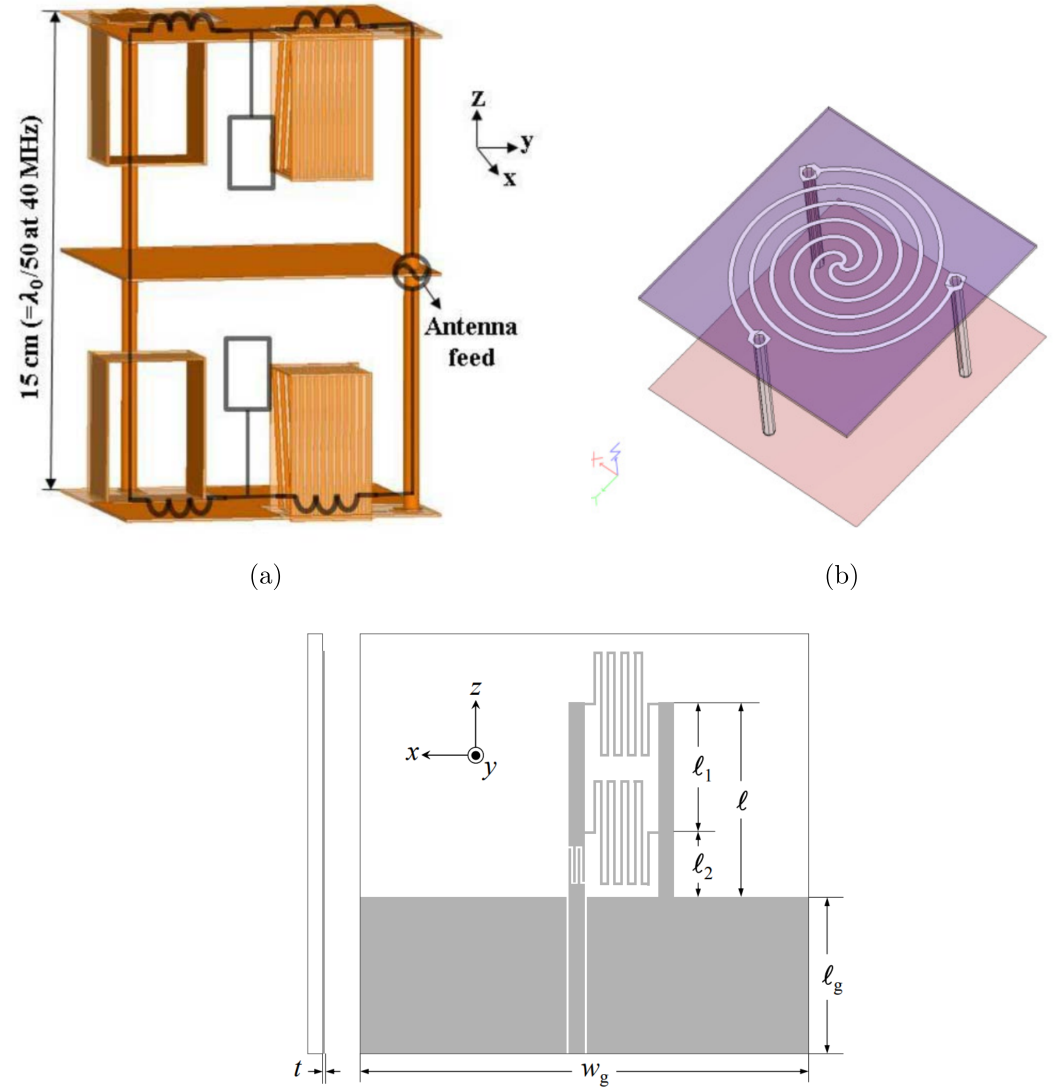

(a) (b)

(c)

Figure 2.15: Other miniaturization techniques of folded dipole antennas: (a) by T-type 180° phase shifter [76], (b) using a spiral transmission line [77], and (c) by loading with a LC resonator [78].

with co-directed currents on the two arms [75, 76]. The phase shifters were realized by a T-type network having two high-Q air-core inductors on its series arm and an open stub as the shunt arm. A similar work was done in [77] where a spiral transmission line was used among three arms of a folded monopole antenna in order to provide the required phase such that an in-phase current distribution can be realized on the antenna arms.

Furthermore, external LC resonators were used to miniaturize folded monopole antennas, where the operating frequency was determined by the resonance frequency of the loading inductors and capacitors, and not by the length of the antenna [78]. The corresponding structures for all the other methods are shown in Fig. 2.15.

2.2.3 Comparison with Conventional Dipole Antenna

Although the radiation properties of the folded dipole are identical to those of a conventional dipole, the major difference between these two antennas lies in their input impedance characteristics. This is because, unlike the open-ended conventional dipole, the folded dipole is a special case of a loop antenna that radiates like an electric dipole due to the small spacing between its two arms [79]. The input impedance profiles of a conventional dipole antenna and a folded dipole antenna are shown in Fig. 2.16. A detailed discussion on the input impedance of a folded dipole antenna will be provided in the next chapter.

It can be seen from the impedance profiles of the two antennas that, unlike the conventional dipole antenna, the half-wavelength (0.5λ) resonance frequency f_R of the folded dipole antenna is surrounded by two antiresonances, $f_{AR,1}$ and $f_{AR,2}$, the first of which lies well below f_R. For a conventional dipole antenna, there is no such antiresonance before f_R, and the first antiresonance expectedly occurs around the one-wavelength (1.0λ) point f_{AR}. It should be noted that, in the case of an ideal loop antenna, the shown antiresonances occur when its circumferential length is equal to 0.5λ and 1.5λ, with the resonance occurring at 1.0λ. The 1.0λ resonance of the loop antenna directly corresponds to f_R of the folded dipole antenna with each of its arms 0.5λ long. However, since the separation between the conductors is

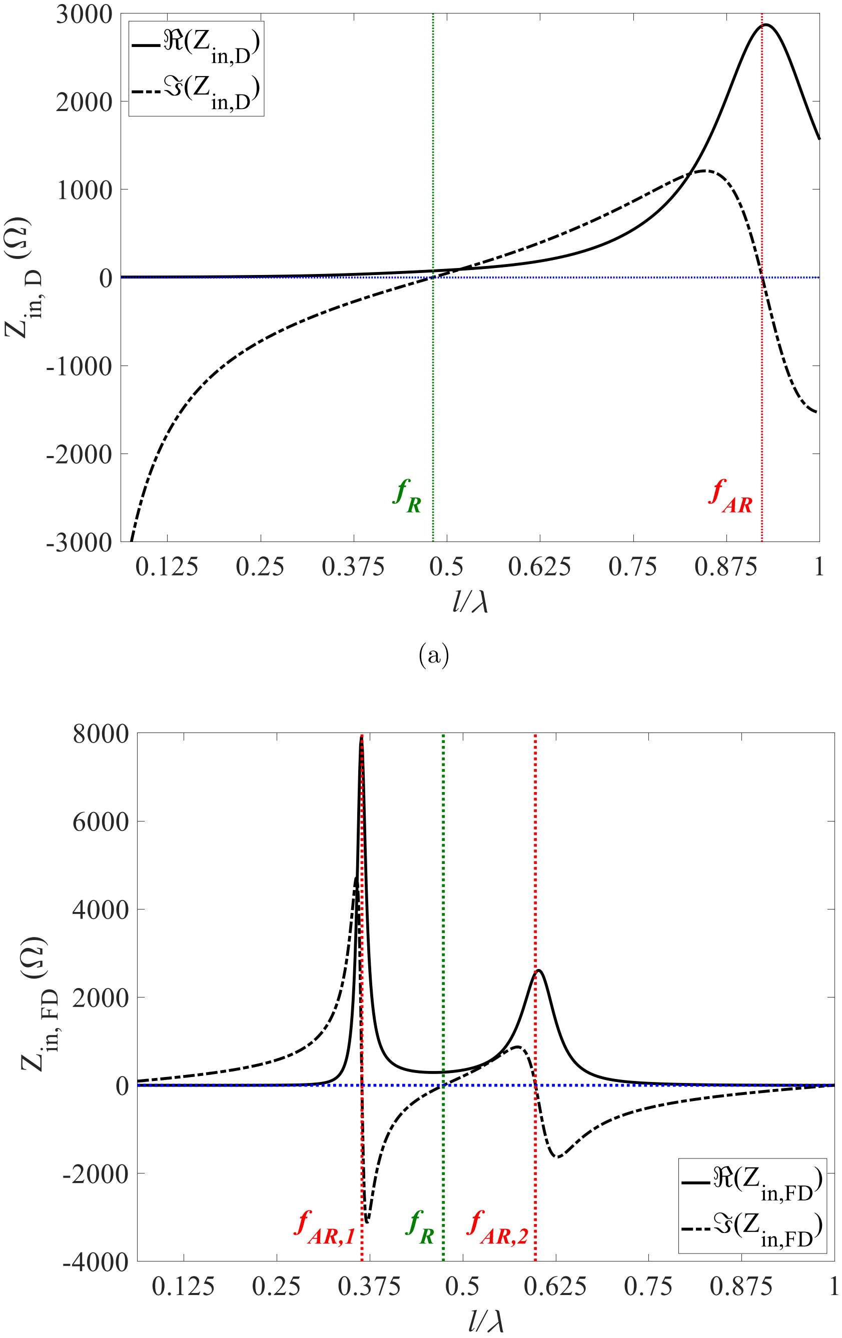

(a)

(b)

Figure 2.16: Input impedance profiles of (a) conventional dipole antenna, and (b) folded dipole antenna.

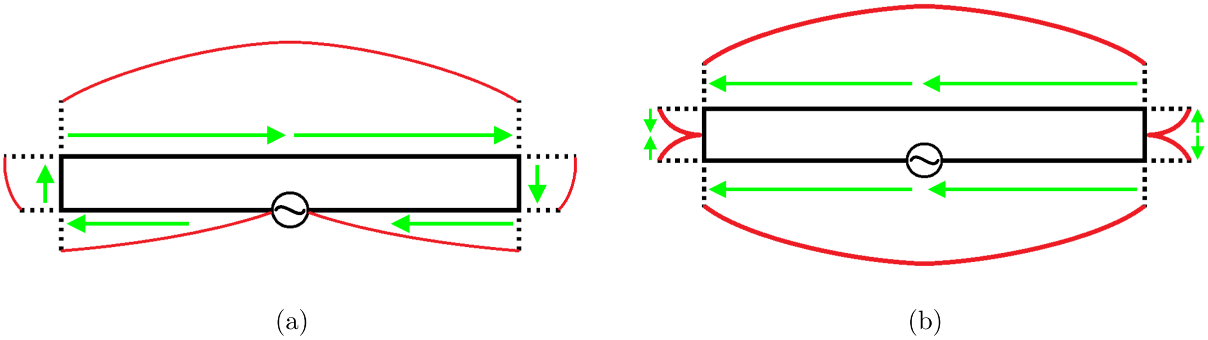
(a) (b)

Figure 2.17: Current distributions on a folded dipole antenna at (a) antiresonance $f_{AR,1}$, and (b) resonance f_R.

much smaller for a folded dipole antenna than for a typical loop, mutual effects cause the antiresonances to be located typically much closer to f_R.

However, despite $f_{AR,1}$ being well below f_R, it is not typically used as the operating point, for the following two related reasons: (1) very high value of input resistance at $f_{AR,1}$ makes it unsuitable for matching to a practical source impedance, and (2) f_R offers higher radiation efficiency. A quick study of the impedance and current profiles at $f_{AR,1}$ and f_R offers some insight. As shown in Fig. 2.17, the folded dipole exhibits a 0.5λ circumferential current distribution at $f_{AR,1}$, akin to a loop antenna at its first antiresonance point. It can be noticed that the current is minimum at the feed point, thus a high input resistance appears at its feed, making it difficult to match with a realistic port impedances. On the contrary, a 1.0λ circumferential current distribution can be observed at f_R, which results in a current maximum at the feed point. As a result, the input resistance at this point is much lower, and therefore easier to match. Besides, at $f_{AR,1}$ the currents on the two arms are oppositely-directed, however the difference in the current amplitudes creates a net unbalanced condition that results in a non-zero radiation efficiency, which can be further improved by introducing asymmetries; one such example is realizing the folded dipole antenna with different cross-sectional dimensions of its arms. In contrast, at f_R the currents on both arms are co-directed and equal in magnitude, thus producing a larger amount of radiation. Thus, all the miniaturization techniques described in the previous section focus mostly on f_R, or realizing an f_R-like current distribution. The issue of reduced input resistance of the folded dipole antenna due to the miniaturization is usually resolved without using any external matching network, either by using multiple folded arms, or by using unequal cross-sectional arm dimensions, as was mentioned in the description of different miniaturization techniques in the previous section. This impedance-modification property is one of the major advantages of the folded dipole antenna over a conventional dipole antenna. Unfortunately, such techniques generally increase complexity and the footprint of these antennas, and often require very large ratios of cross-sectional arm dimensions, which may be counterproductive to the goal of miniaturization.

However, in the next chapters, it will be demonstrated how to engineer the input resistance of a folded dipole antenna at the antiresonance $f_{AR,1}$ by means of a novel reactive-loading scheme, and use it to make the antenna inherently well-matched with respect to a given source impedance without using multiple folded arms, very large ratios of cross-sectional arm dimensions, or an external matching network, such that an overall smaller footprint can be realized.

Chapter 3

Theory

3.1 Introduction

In this chapter, the well-established theory of folded dipole antennas is extended to include the effects of reactive loading. The input impedance trends corresponding to different reactive loading scenarios have been studied in order to find crucial conditions that will allow good matching at high miniaturization levels. Finally, a transition from a symmetric to an asymmetric loading scheme has been studied and the corresponding benefits are described.

3.2 Theory of the Unloaded Folded Dipole Antenna

The unloaded folded dipole antenna is typically analyzed by decomposing the currents on its arms into two modes, namely the transmission-line mode (TLM, or odd mode), for which the currents on the arms flow in opposite directions and therefore do not contribute to radiation, and the antenna mode (AM, or even mode), for which the currents are co-directed on both arms, thus creating an unbalanced current condition on the antenna that accounts for all of the radiation [80]. The decomposition of the antenna currents into these two modes is shown in Fig. 3.1. The overall input impedance of the antenna is estimated by combining the corresponding TLM and AM input impedances.

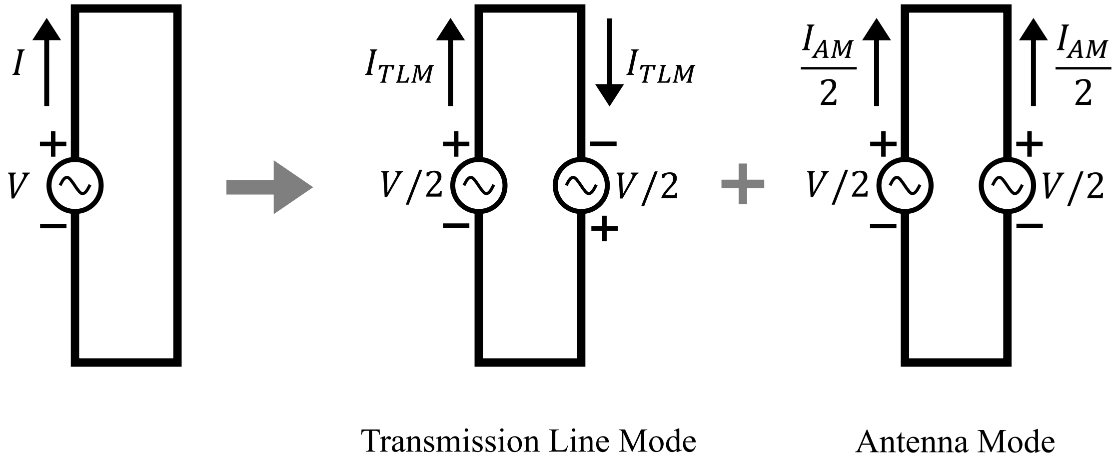

Figure 3.1: Decomposition of unloaded folded dipole antenna into transmission-line mode (TLM) and antenna mode (AM).

3.2.1 Transmission Line Mode (TLM)

As shown in Fig. 3.1, the two voltage sources ($V/2$) on the folded dipole arms are of opposite polarity in order to maintain the contra-directed currents (I_{TLM}) on the two arms. Now, the two voltage sources can be decomposed into an equivalent set of voltage sources ($V/4$) without disturbing the current distribution on the arms in order to view the folded dipole as a set of two identical shorted transmission lines of length $l/2$ that are driven by a total source voltage of $V/2$ across its input terminals. The decomposition is shown in Fig. 3.2. Thus, the TLM current can be calculated as:

$$I_{TLM} = \frac{V/2}{Z_{TLM}} \tag{3.1}$$

where Z_{TLM} is the input impedance of the transmission line mode, which can be determined using the well-known equation:

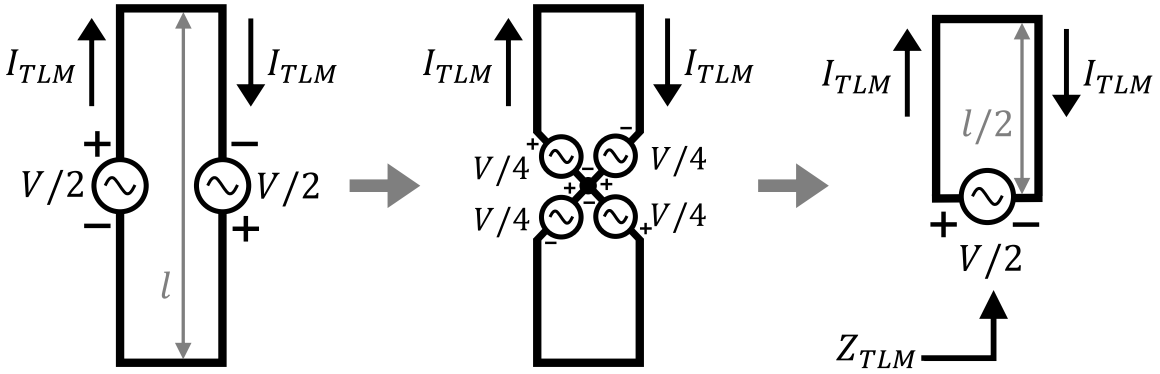

Figure 3.2: TLM decomposition for unloaded folded dipole antenna.

$$Z_{TLM} = jZ_0 \tan\left(\frac{\beta l}{2}\right) \tag{3.2}$$

where Z_0 is the characteristic impedance of the two-conductor equivalent transmission line and β is the corresponding propagation constant.

3.2.2 Antenna Mode (AM)

For the AM, the two voltage sources on the folded dipole arms are of the same polarity, thus maintaining co-directed currents ($I_{AM}/2$) on the two arms as shown in Fig. 3.1. For this case, the two voltage sources can be combined into a single source of voltage $V/2$ by exploiting their identical polarities, such that the current distributions on the two arms again remain unaffected. The described procedure is shown in Fig. 3.3. Thus, the AM current can be estimated as:

$$I_{AM} = \frac{V/2}{Z_{AM}} \tag{3.3}$$

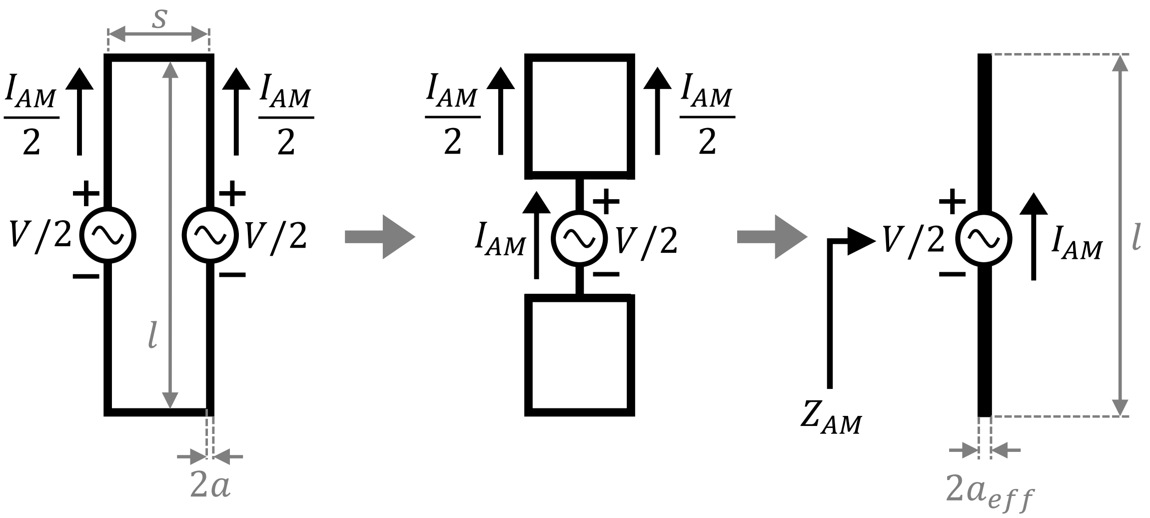

Figure 3.3: AM decomposition for unloaded folded dipole antenna.

where Z_{AM} is the input impedance of the antenna mode, which is typically obtained by replacing the folded dipole antenna with a single equivalent linear dipole antenna of the same length, but with an effective cross-sectional dimension. For a folded dipole antenna with cylindrical arms of cross-sectional radius a and center-to-center separation s between the arms, the effective cross-sectional radius of the equivalent linear dipole can be calculated as [80, 81]:

$$a_{eff} = \sqrt{as}. \tag{3.4}$$

Thus, Z_{AM} can be obtained using the induced-EMF method using the following expressions [2]:

$$\begin{aligned}\Re(Z_{AM}) =& \frac{\eta}{2\pi}\Bigg\{C + \ln(kl) - C_i(kl) + \frac{1}{2}\sin(kl)[S_i(2kl) - 2S_i(kl)] \\ &+ \frac{1}{2}\cos(kl)\left[C + \ln\left(\frac{kl}{2}\right) + C_i(2kl) - 2C_i(kl)\right]\Bigg\} \\ \Im(Z_{AM}) =& \frac{\eta}{4\pi}\Bigg\{2S_i(kl) + \cos(kl)[2S_i(kl) - S_i(2kl)] - \sin(kl)\Bigg[2C_i(kl) \\ &- C_i(2kl) - C_i\left(\frac{2ka_{eff}^2}{l}\right)\Bigg]\Bigg\}\end{aligned} \tag{3.5}$$

where, C is Euler's constant ≈ 0.5772, η is the impedance of the medium, k is the propagation constant, and $S_i(x)$ and $C_i(x)$ are the sine and cosine integrals, respectively, which can be given as:

$$\begin{aligned}S_i(x) &= \int_0^x \frac{\sin(\tau)}{\tau}d\tau \\ C_i(x) &= -\int_x^\infty \frac{\cos(\tau)}{\tau}d\tau.\end{aligned} \tag{3.6}$$

However, the method described above for estimating the input impedance of the AM requires two conditions to be satisfied simultaneously by the equivalent dipole, and therefore by the individual arms of the folded dipole: (1) the currents on the two arms must be identical for a particular mode (can be enforced by making the arms identical), and (2) the dipoles must be slender, in that their cross-sectional dimensions must be infinitesimally thin compared to the wavelength. Similarly, their separations must also be deeply subwavelength.

3.2.3 Overall Input Impedance of the Folded Dipole Antenna

Finally, the overall input impedance of the folded dipole antenna ($Z_{in,FD}$) can be estimated by taking the ratio of the total voltage and current at the feed location of the folded dipole antenna shown in Fig. 3.1.

$$Z_{in,FD} = \frac{V}{I} = \frac{V}{I_{TLM} + \dfrac{I_{AM}}{2}}. \tag{3.7}$$

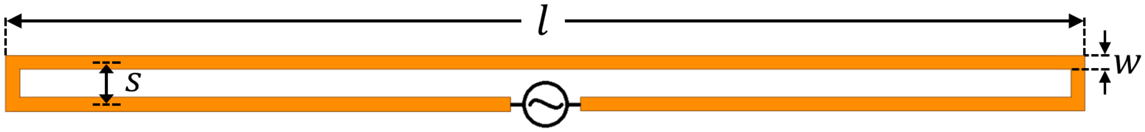

Figure 3.4: Schematic of the planar unloaded folded dipole antenna.

Substituting the expressions of I_{TLM} and I_{AM} from equations 3.1 and 3.3, $Z_{in,FD}$ can be obtained as:

$$Z_{in,FD} = \frac{V}{\dfrac{V}{2Z_{TLM}} + \dfrac{V}{4Z_{AM}}} = \frac{4Z_{TLM}Z_{AM}}{Z_{TLM} + 2Z_{AM}}. \tag{3.8}$$

In this chapter, a planar unloaded folded dipole antenna based on co-planar strip (CPS) lines has been selected for study. For simplicity, no dielectric substrate has been used for this antenna. In the next chapter, an example will be shown where a printed folded dipole antenna of length $l = 38$ mm ($= \lambda/2$ at 3.95 GHz) will be strongly miniaturized by approximately 75% (i.e., $l \approx \lambda/8$) and made to operate at around 1 GHz, using the technique described in this chapter. Thus, for the current study, the selected folded dipole antenna was assigned with the same length, with each arm width $w = 0.05$ mm ($\sim 0.0006\lambda$ at 3.95 GHz), and the separation between the arms $s = 0.1$ mm ($\sim 0.001\lambda$ at 3.95 GHz). A schematic of the antenna is shown in Fig. 3.4. The individual TLM and AM impedances corresponding to the planar unloaded folded dipole antenna were calculated numerically using MATLAB, and then combined to obtain the overall analytical input impedance of the antenna using equation 3.8.

Z_{TLM} was obtained by evaluating the input impedance of a short-circuited section of CPS on an air substrate using equation 3.2, where the characteristic impedance Z_0 and the propagation constant β of the CPS transmission line were calculated using the following equations [82]:

$$Z_0 = \frac{120\pi}{\sqrt{\varepsilon_{eff}}} \cdot \frac{K(k')}{K(k)} \tag{3.9}$$

where

$$\varepsilon_{eff} = 1 + \frac{1}{2}(\varepsilon_r - 1)\frac{K(k)K(k_d')}{K(k')K(k_d)} \tag{3.10}$$

where

$$\begin{aligned} k &= \sqrt{1 - \left(\frac{s}{s+2w}\right)^2} \\ k' &= \sqrt{1-k^2} \\ k_d &= \sqrt{1 - \frac{\sinh^2(\pi s/4h)}{\sinh^2[\pi(s+2w)/4h]}} \\ k_d' &= \sqrt{1-k_d^2} \end{aligned} \tag{3.11}$$

and,

$$\beta = \frac{\omega}{c/\sqrt{\varepsilon_{eff}}}. \tag{3.12}$$

For the AM input impedance, the planar unloaded folded dipole was converted into an equivalent unloaded folded dipole with cylindrical arms, where the cross-sectional radius of each of the cylindrical arms (a) can be related to the width of an individual planar arm w as $a = w/4$ [83]. Thus, Z_{AM} of the planar folded dipole antenna was obtained by estimating the driving point impedance of a conventional cylindrical dipole antenna with an effective cross-sectional radius $a_{eff} = \sqrt{ws/4}$ using equation 3.5.

Furthermore, the structure was simulated using a full-wave FEM-based electromagnetic simulator Ansys HFSS and the resultant input impedance was compared with the analytical solution. The comparison is shown in Fig. 3.5. A generally very close agreement is observed, which only slightly degrades around the second antiresonance $f_{AR,2}$, likely because the induced-EMF method starts becoming inaccurate approximately beyond $l = 0.6\lambda$ [84].

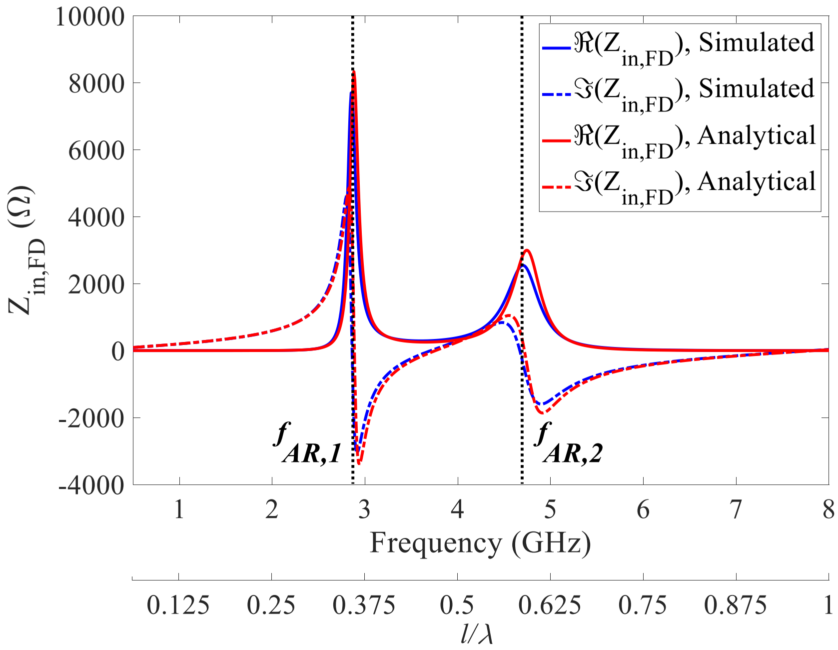

Figure 3.5: Comparison of $Z_{in,FD}$ of planar unloaded folded dipole antenna, obtained from simulation and analytical calculation.

3.3 Theory of the Reactively Loaded Folded Dipole Antenna

In this section, the analytical model for the unloaded folded dipole antenna has been expanded in order to accommodate loading reactances and the corresponding TLM and AM circuits were modified accordingly. To preserve the symmetry required for even-/odd-mode analysis, the loading reactances X_{load} are placed on both driven and folded arms, at a distance l_1 from the ends. The corresponding modified TLM and AM schematics are shown in Figs. 3.6 and 3.7, respectively.

The modified TLM, as compared to the unloaded case, is now comprised of three segments: (1) a short-circuited transmission-line segment of length l_1 near the end, (2) two loading reactances (X_{load}) in series, and finally (3) the remaining transmission line segment of length l_2 $(= l/2 - l_1)$ between the loading elements and the feed. Therefore, the overall TLM input impedance can be calculated as:

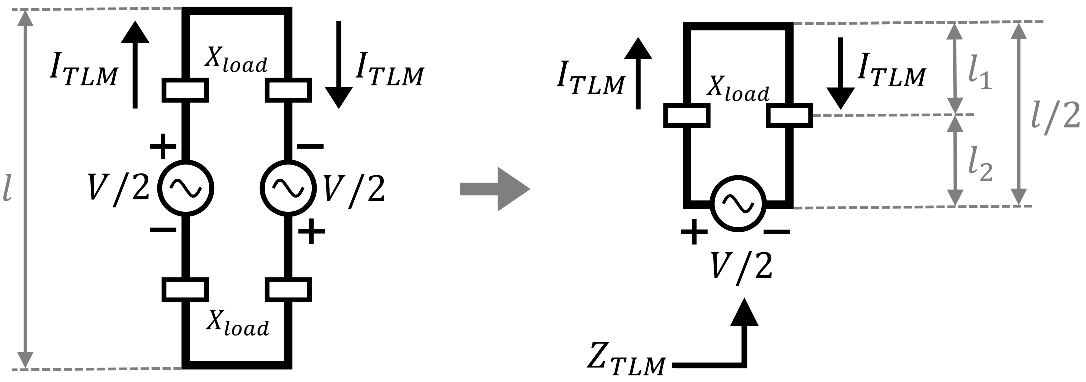

Figure 3.6: Modified TLM for the reactively loaded folded dipole antenna.

$$Z_{TLM} = Z_0 \frac{Z_L + jZ_0 \tan(\beta l_2)}{Z_0 + jZ_L \tan(\beta l_2)} \tag{3.13}$$

where,

$$Z_L = 2jX_{load} + jZ_0 \tan(\beta l_1) \tag{3.14}$$

where X_{load} is the total loading reactance placed on each half of one arm.

For the loaded AM problem, as shown in Fig. 3.7, the two loading reactances will appear in parallel for each half of the antenna, and the total reactive loading will be two such parallel combinations of the loading reactances in series, i.e., $2 \cdot (X_{load} \| X_{load}) = X_{load}$. This is then simply added to the Z_{AM} of the unloaded folded dipole (as obtained using the expressions in equation 3.5) in order to find the loaded AM impedance. Although, this is a very approximate method for estimating the AM input impedance of the loaded folded dipole as it does not take into account the actual placement of the reactive loading, it is nevertheless fairly accurate for a slender dipole in the low-frequency limit (i.e., much below their nominal dipolar resonances), where the AM input resistance $\Re(Z_{AM})$ is small. Fortunately, the objective of this exercise is to investigate the behaviour of the input impedance profile

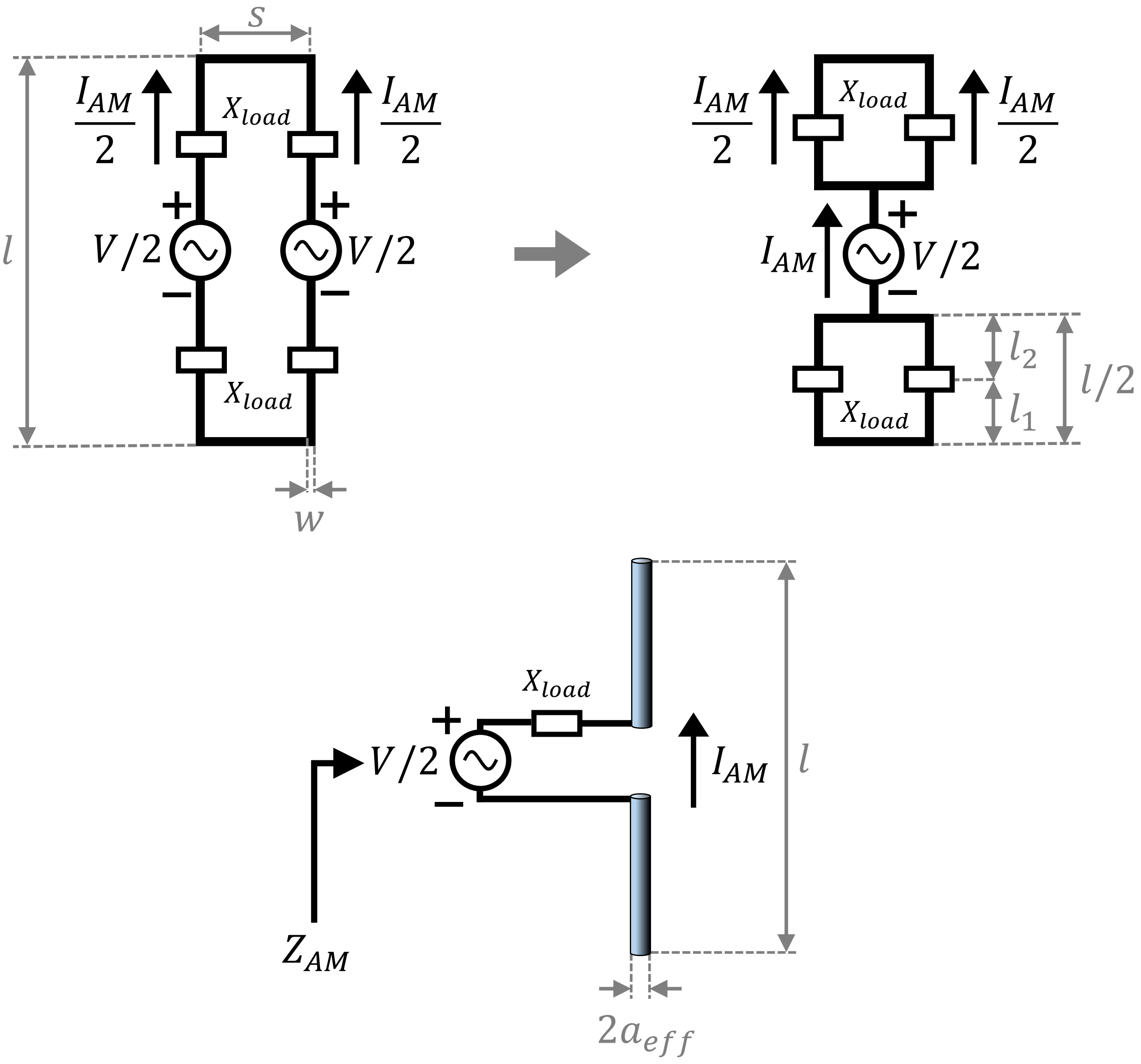

Figure 3.7: Modified AM for the reactively loaded folded dipole antenna.

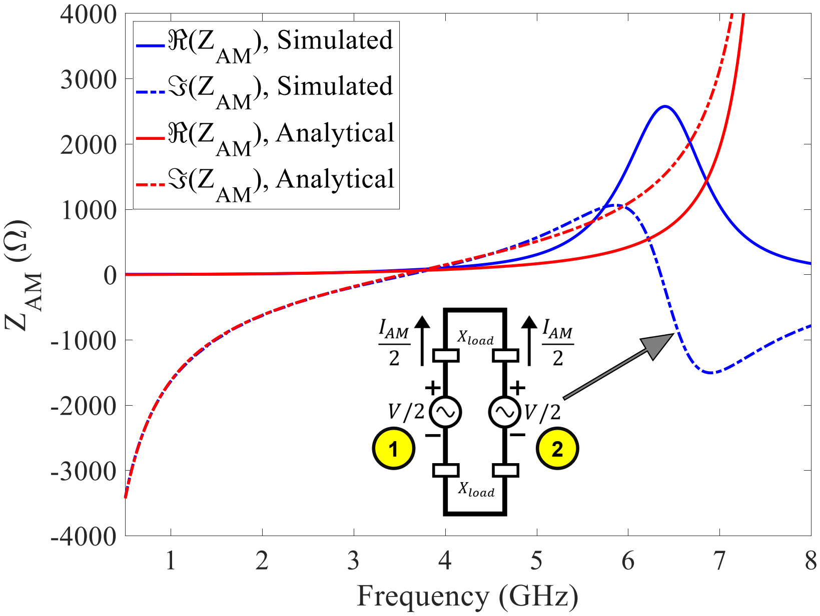

Figure 3.8: Comparison of AM input impedance estimated using simulation and analytically for series-LC loading (Loading L = 5 nH, and C = 1 pF), with the simulated structure as the inset.

below the 0.5λ point, where the folded dipole antenna is likely to be operated after being miniaturized.

A particular case has been chosen to validate the suggested modifications, where a series combination of a 5 nH inductor and 1 pF capacitor (X_{load}: 5 nH in series with 1 pF) were placed in the middle of each half of the individual arms (i.e., $l_1 = l_2 = l/4$ in Fig. 3.7). In order to justify the proposed method for estimating the Z_{AM}, the same 38-mm-long planar folded dipole antenna on air substrate was simulated in HFSS, with the X_{load} placed right in the middle of each half of the dipole antenna. However, this time both the arms were excited by identical voltage sources, maintaining the polarity as shown in the inset of Fig. 3.8 in order to obtain the antenna mode input impedance, which was then calculated using the following equation that involves the Z-parameters obtained from the simulation:

$$\frac{V}{2} = Z_{11}\frac{I_{AM}}{2} + Z_{12}\frac{I_{AM}}{2} \quad \Rightarrow \quad Z_{AM} = \frac{V/2}{I_{AM}} = \frac{1}{2}(Z_{11} + Z_{12}). \tag{3.15}$$

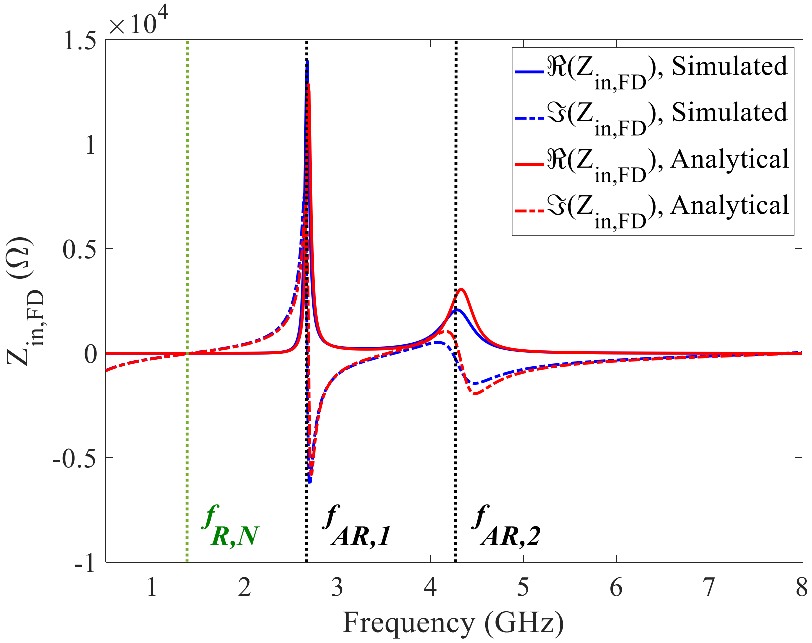

Figure 3.9: Comparison of input impedance of a loaded folded dipole estimated using simulation and analytically for series-LC loading (Loading L = 5 nH, and C = 1 pF).

The simulated input impedance was then compared with the Z_{AM} estimated using the aforementioned method. The comparison is also shown in Fig. 3.8. It can be noticed that similar to the unloaded case, again there is a very good agreement between the simulated and analytical results that slightly degrades only around the second antiresonance $f_{AR,2}$.

The individually computed TLM and AM input impedances of the corresponding LC-loaded antenna were then combined using equation 3.8 in order to get its overall input impedance, and compared with the corresponding simulated results. Again, a very good agreement can be seen at frequencies up to 4 GHz, as shown in Fig. 3.9. Moreover, it must be noticed that a new resonance ($f_{R,N}$) has appeared before the antiresonance $f_{AR,1}$, the occurrence of which can be related directly to the application of series capacitive loading into the inherently inductive antenna. It will be shown that, this new resonance $f_{R,N}$ together with the antiresonance $f_{AR,1}$ can be used to achieve good matching with respect to a given source impedance at a highly miniaturized operating frequency, without the need of an external matching network.

3.4 Impedance Trends

Now that the validity of the proposed analytical model is established, the trends of the analytically calculated input impedances for different inductive- (L-) and capacitive- (C-) loading cases were examined next. The corresponding plots are shown in Fig. 3.10. It can be seen from Fig. 3.10(a) that loading the folded dipole with series inductors shifts all the resonances towards lower frequencies, while increasing the $\Re(Z_{in,FD})$ at the $f_{AR,1}$ points, thus making these frequencies not suitable for matching. On the contrary, as shown in Fig. 3.10(b), the input impedance trend corresponding to the series C-loading is exactly the opposite the resonances are shifted towards higher frequencies, and the $\Re(Z_{in,FD})$ at the $f_{AR,1}$ points decreases with decreasing loading capacitance values, i.e., increasing capacitive loading.

Although the new resonance $f_{R,N}$ is typically at a frequency lower than the usual 0.5λ resonance point f_R, it is usually not possible to achieve good matching at this frequency as the corresponding input resistance ($\Re(Z_{in,FD})$) is very small. Thus, the only way to enable matching at this point is to increase the value of $\Re(Z_{in,FD})$, which can be done by bringing the $f_{AR,1}$ point very close to the $f_{R,N}$, such that the $\Re(Z_{in,FD})$ at $f_{R,N}$ can benefit from the quickly rising slope just before $f_{AR,1}$, and be large enough to facilitate matching with a practical source impedance.

A 3-D plot has been created showing $f_{R,N}$ and $f_{AR,1}$ as functions of loading inductance and capacitance, as shown in Fig. 3.11. It can be seen that the two resonances approach each other for a large value of loading inductance and a small value of loading capacitance (encircled). However, it was found that in order to bring them very close to each other, extreme values of loading reactances will be necessary, an example of which has been demonstrated in the next section.

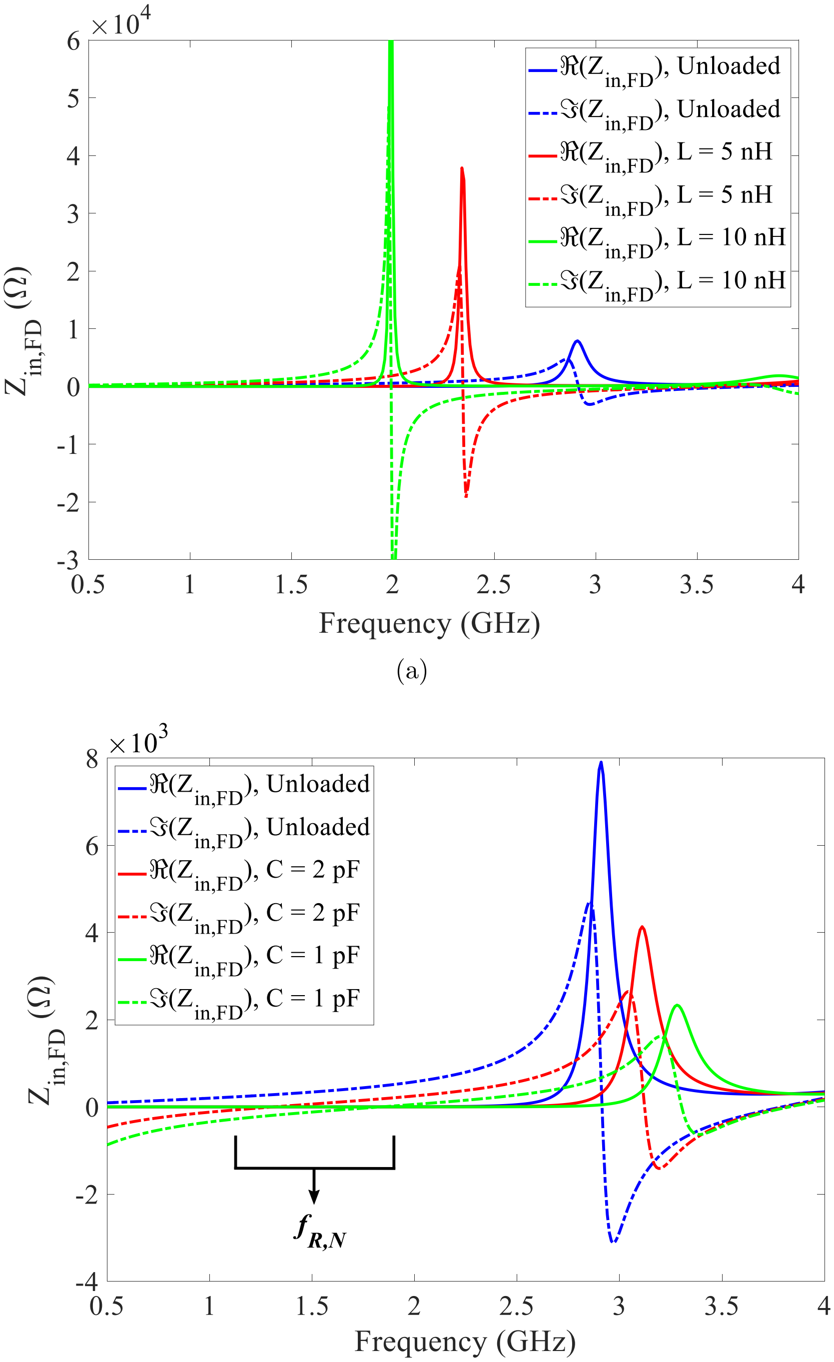

(a)

(b)

Figure 3.10: Input impedance trends for the reactively loaded folded dipole antenna (a) L-loading, (b) C-loading.

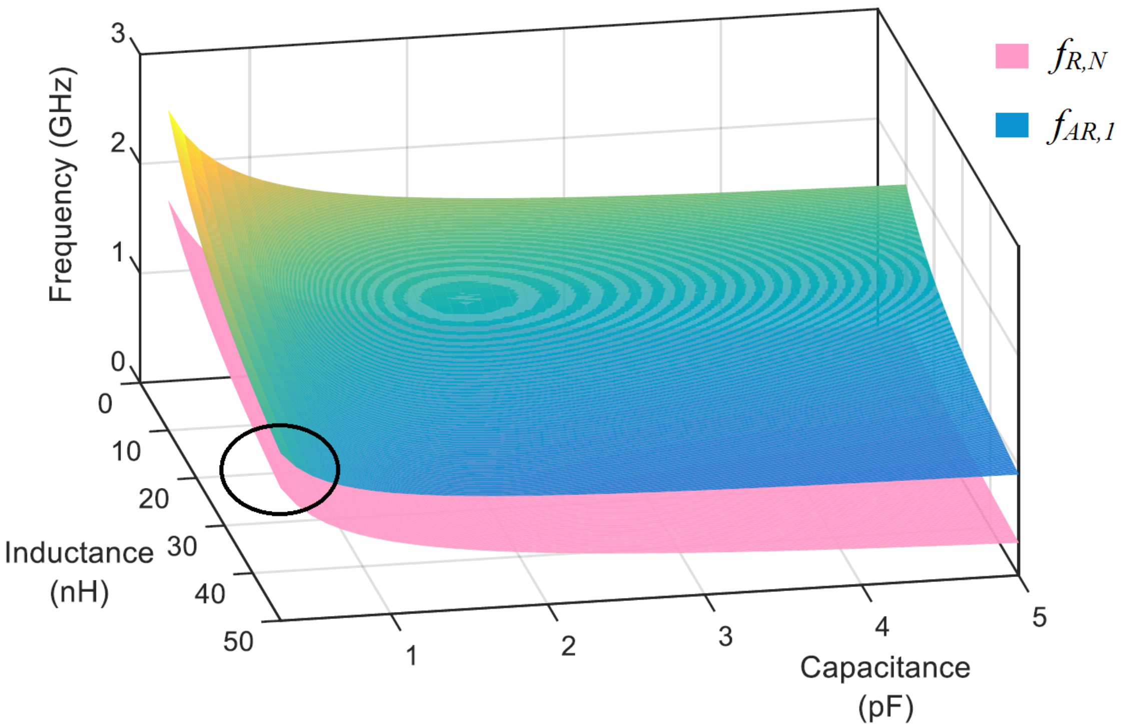

Figure 3.11: 3-D plot of $f_{R,N}$ and $f_{AR,1}$ as functions of loading inductance and capacitance.

3.5 Calculation of Loading L and C Values for Given $f_{R,N}$ and $f_{AR,1}$

Using the analytical method proposed in this chapter, it has been shown at the end of Section 3.3 that for a given set of loading L and C values, it is possible to successfully predict the locations of the new resonance $f_{R,N}$ and the first antiresonance $f_{AR,1}$ for a symmetrically loaded folded dipole antenna without the need of any time-consuming simulation, an example of which has been shown using Fig. 3.9. Additionally, in Section 3.4, it was mentioned that in order to achieve good matching at a given miniaturized frequency, it is important to bring the two resonances close to each other. Thus, it also becomes important to be able to estimate the required loading L and C values for a given set of $f_{R,N}$ and $f_{AR,1}$, which can be done by applying proper conditions to the expression of the real and imaginary parts of the overall input impedance of the reactively loaded folded dipole antenna.

To do that, the first step is to expand the expressions of the modified TLM and AM input impedances, and then combine them to form the complete expression of $Z_{in,FD}$. Using equations 3.13 and 3.14, the modified TLM input impedance can be expanded as:

$$Z_{TLM} = jZ_0 \frac{2X_{load} + Z_0 a_1}{Z_0 a_2 - 2X_{load}\tan(\beta l_2)} \tag{3.16}$$

where the parameters a_1 and a_2 can be given as following:

$$a_1 = \tan(\beta l_1) + \tan(\beta l_2) \tag{3.17}$$

$$a_2 = 1 - \tan(\beta l_1)\tan(\beta l_2). \tag{3.18}$$

The modified AM input impedance can be written following the discussion given in Section 3.3 as:

$$Z_{AM} = Z_{du} + jX_{load} = \Re(Z_{du}) + j\Im(Z_{du}) + jX_{load} \tag{3.19}$$

where Z_{du} is the self-impedance of the unloaded equivalent cylindrical conventional dipole with an effective cross-sectional dimension. Substituting equations 3.16 and 3.19 into equation 3.8, the expression for the overall input impedance of a folded dipole becomes:

$$\begin{aligned} Z_{in,FD} =& \frac{4(Z_{du} + jX_{load})\left(jZ_0 \dfrac{2X_{load} + Z_0 a_1}{Z_0 a_2 - 2X_{load}\tan(\beta l_2)}\right)}{2(Z_{du} + jX_{load}) + \left(jZ_0 \dfrac{2X_{load} + Z_0 a_1}{Z_0 a_2 - 2X_{load}\tan(\beta l_2)}\right)} \\ =& \frac{4Z_0 a_3 \Re(Z_{du})[a_6 - 2X_{load}a_4 - 2a_4\Im(Z_{du})]}{a_7} \\ &+ j\frac{2Z_0 a_3[2X_{load}a_6 + 2a_6\Im(Z_{du}) + 4a_4\Re(Z_{du})^2]}{a_7} \end{aligned} \tag{3.20}$$

where the parameters a_3, a_4, a_5, a_6 and a_7 can be given as following:

$$a_3 = 2X_{load} + Z_0 a_1 \tag{3.21}$$

$$a_4 = Z_0 a_2 - 2X_{load} \tan(\beta l_2) \tag{3.22}$$

$$a_5 = 2X_{load} a_4 + Z_0 a_3 \tag{3.23}$$

$$a_6 = a_5 + 2\Im(Z_{du}) a_4 \tag{3.24}$$

$$a_7 = 4\Re(Z_{du})^2 a_4^2 + a_6^2. \tag{3.25}$$

Now, in order to find the new resonance $f_{R,N}$, the imaginary part of $Z_{in,FD}$ must be set to zero, and then the proper solution needs to be found for X_{load}. Expanding the imaginary part of equation 3.20 by substituting the expressions of a_3, a_4, a_5, a_6 and a_7:

$$\begin{aligned}\Im(Z_{in,FD}) =&2Z_0[2X_{load} + Z_0 a_1][8X_{load}^3\{-\tan(\beta l_2)\} + 4X_{load}^2\{Z_0(a_2+1) - 4\tan(\beta l_2)\Im(Z_{du})\}\\ &+2X_{load}\{Z_0^2 a_1 + 4Z_0 a_2 \Im(Z_{du}) - 4\tan(\beta l_2)(\Re(Z_{du})^2 + \Im(Z_{du})^2) + 2Z_0\Im(Z_{du})\}\\ &+\{2Z_0^2 a_1 \Im(Z_{du}) + 4Z_0 a_2(\Re(Z_{du})^2 + \Im(Z_{du})^2)\}] = 0.\end{aligned} \tag{3.26}$$

It can be seen from equation 3.26 that there are four possible solutions for X_{load}, from which all the unphysical and inappropriate solutions need to be discarded. To find the first antiresonance $f_{AR,1}$, the real part of $Z_{in,FD}$ can be maximized with respect to X_{load}, exploiting the fact that $\Re(Z_{in,FD})$ becomes maximum at the antiresonances. The following equations can be used to find the solutions:

$$\frac{d\Re(Z_{in,FD})}{dX_{load}} = 0, \quad and \quad \frac{d^2\Re(Z_{in,FD})}{dX_{load}^2} \Rightarrow Negative. \tag{3.27}$$

Again, the correct solution needs to be found for X_{load} corresponding to the antiresonance $f_{AR,1}$. All the calculations were done numerically using MATLAB.

Let us consider the correct solutions for $f_{R,N}$ is $X_{load} = X_1$ and for $f_{AR,1}$ is $X_{load} = X_2$. Now, since X_1 and X_2 are the solutions of X_{load} at resonances $f_{R,N}$ and $f_{AR,1}$, respectively, and X_{load} is essentially the series combination of loading L and C, the following expressions can be written:

$$X_1 = \left(\omega_1 L - \frac{1}{\omega_1 C}\right) \tag{3.28}$$

$$X_2 = \left(\omega_2 L - \frac{1}{\omega_2 C}\right) \tag{3.29}$$

where ω_1 and ω_2 are the angular frequencies corresponding to $f_{R,N}$ and $f_{AR,1}$, respectively. Solving equations 3.28 and 3.29, the expressions for loading L and C can be found as:

$$L = \frac{\dfrac{X_1}{\omega_2} - \dfrac{X_2}{\omega_1}}{\dfrac{\omega_1}{\omega_2} - \dfrac{\omega_2}{\omega_1}} \tag{3.30}$$

$$C = \frac{\dfrac{\omega_1}{\omega_2} - \dfrac{\omega_2}{\omega_1}}{\omega_2 X_1 - \omega_1 X_2}. \tag{3.31}$$

From equations 3.30 and 3.31, it can be easily seen that for $f_{R,N}$ and $f_{AR,1}$ to be situated very close to each other, i.e., $\omega_1 \approx \omega_2$, the loading inductance L needs to have a very large value, whereas the loading capacitance C needs to be very small.

An example was carried out following the above calculations. It was found that in order to place $f_{R,N}$ at 1.0 GHz and $f_{AR,1}$ at 1.1 GHz where the antenna is $\sim 75\%$ miniaturized, the required loading L and C values are 297.13 nH and 0.08 pF, respectively. A representative input impedance plot for this case is shown in Fig. 3.12. It can be easily seen that even after using extreme L and C values, the two resonances $f_{R,N}$ and $f_{AR,1}$ are still not sufficiently close to each other in order to achieve good matching with respect to a practical source impedance, since the $\Re(Z_{in,FD})$ at $f_{R,N}$ is only 0.003 Ω. Thus, bringing $f_{AR,1}$ even closer to $f_{R,N}$ would require even larger L and C values, the practical implementation of which can easily increase the size of the structure, making it more lossy.

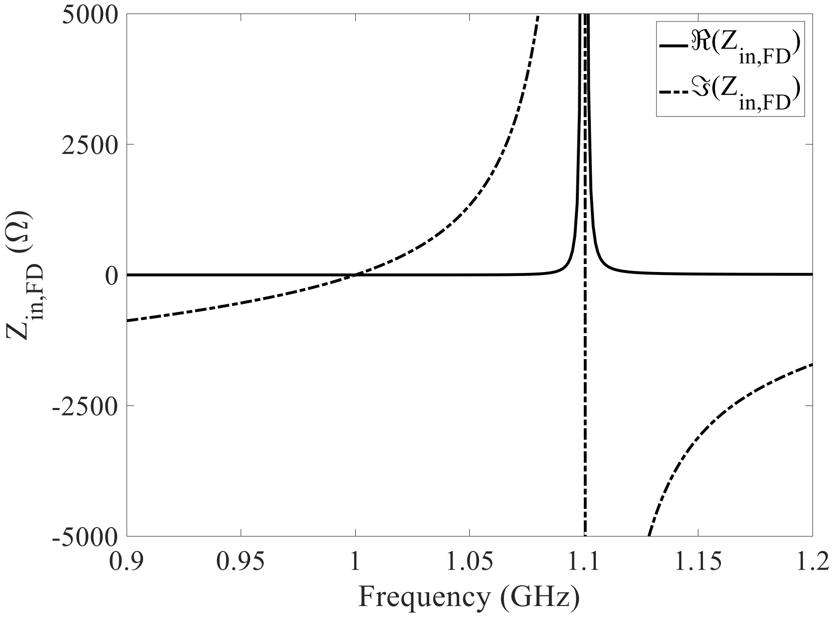

Figure 3.12: Input impedance of a loaded folded dipole with loading L = 297.13 nH, and C = 0.08 pF.

3.6 Introduction of Asymmetry

Following the discussion in the previous subsection, it was decided to introduce asymmetries in the current loading scheme, and explore if there are any potential benefits. A study has been devised in this section to examine how the frequencies of the two resonances $f_{R,N}$ and $f_{AR,1}$ vary as a function of the asymmetries introduced into the loading reactance values on the two arms, and thereby identify a trend that might be useful for bringing the two resonances closer without the need of any extreme reactance values.

A symmetrically loaded folded dipole that has identical LC-loading on both arms (X_{load}: 10 nH in series with 0.5 pF) has been selected as the starting point. The dimensions of the antenna were kept the same as before, with the loading reactances placed halfway between the antenna ends and the feed location. In the next step, the loading L or C value on one arm was increased by a small amount, and the same amount was subtracted from the loading values on the other arm, thus making one of the arms more inductive or capacitive. Six sets of parametric simulations were performed:

1. L was increased on the driven arm by an amount ΔL, decreased on the folded arm by the same amount, thus making the driven arm more inductive, keeping the loading capacitances on both arms unchanged.

2. L was increased on the folded arm by an amount ΔL, decreased on the driven arm by the same amount, thus making the folded arm more inductive, again keeping the loading capacitances on both arms unchanged.

3. C was increased on the driven arm by an amount ΔC, decreased on the folded arm by the same amount, thus making the folded arm more capacitive, keeping the loading inductances on both arms unchanged.

4. C was increased on the folded arm by an amount ΔC, decreased on the driven arm by the same amount, thus making the driven arm more capacitive. The loading inductances on both arms were kept unchanged.

5. L was increased on the driven arm by an amount ΔL, decreased on the folded arm by the same amount, thus making the driven arm more inductive; and C was increased on the driven arm by an amount ΔC, decreased on the folded arm by the same amount, thus making the folded arm more capacitive.

6. Finally, L was increased on the folded arm by an amount ΔL, decreased on the driven arm by the same amount, thus making the folded arm more inductive; and C was increased on the folded arm by an amount ΔC, decreased on the driven arm by the same amount, thus making the driven arm more capacitive.

The differences between $f_{R,N}$ and $f_{AR,1}$ resonance frequencies are obtained from each parametric simulation and listed in Table 3.1 for comparison. It can be noticed that as the folded arm becomes more inductive (increase in L on folded arm) or/and the driven arm more capacitive (decrease in C on driven arm), the asymmetric loading results in a smaller difference between the $f_{R,N}$ and $f_{AR,1}$ resonance points, and the difference decreases

Cases	ΔL (nH)	L on Driven arm (nH)	L on Folded arm (nH)	ΔC (pF)	C on Driven arm (pF)	C on Folded arm (pF)	Difference (MHz)
Symmetric Loading	0	10	10	0	0.5	0.5	890
L increased on Driven arm	2	12	8	0	0.5	0.5	940
	4	14	6				990
	6	16	4				1070
L increased on Folded arm	2	8	12	0	0.5	0.5	820
	4	6	14				760
	6	4	16				720
C increased on Driven arm	0	10	10	0.1	0.6	0.4	930
				0.2	0.7	0.3	950
				0.3	0.8	0.2	1010
C increased on Folded arm	0	10	10	0.1	0.4	0.6	830
				0.2	0.3	0.7	730
				0.3	0.2	0.8	560
L + C increased on Driven arm	2	12	8	0.1	0.6	0.4	980
	4	14	6	0.2	0.7	0.3	1080
	6	16	4	0.3	0.8	0.2	1160
L + C increased on Folded arm	2	8	12	0.1	0.4	0.6	750
	4	6	14	0.2	0.3	0.7	610
	6	4	16	0.3	0.2	0.8	430

Table 3.1: Differences between the $f_{R,N}$ and $f_{AR,1}$ as functions of added asymmetries in loading reactance values.

even further with increasing asymmetry. The trend is exactly opposite, i.e., the difference between $f_{R,N}$ and $f_{AR,1}$ increases, when the driven arm is more inductive (increase in L on driven arm) or/and the folded arm more capacitive (decrease in C on folded arm). The input impedance profiles of the asymmetrically loaded cases with both varying ΔL and ΔC (5^{th} and 6^{th} sets listed in Table 3.1) are compared with the input impedance of the symmetrically loaded case, and shown in Figs. 3.13(a) and 3.13(b) respectively.

A particular asymmetrically loaded case has been selected from Table 3.1 in order to compare the loading L and C values with an equivalent symmetrically loaded case that results in a same set of $f_{R,N}$ and $f_{AR,1}$ resonance frequencies. For ΔL = 6 nH and ΔC = 0.3 pF from the 6^{th} set described in Table 3.1, the loading vales on the driven arm is 0.2 pF in series with 4 nH, and on the folded arm is 0.8 pF in series with 16 nH. This particular

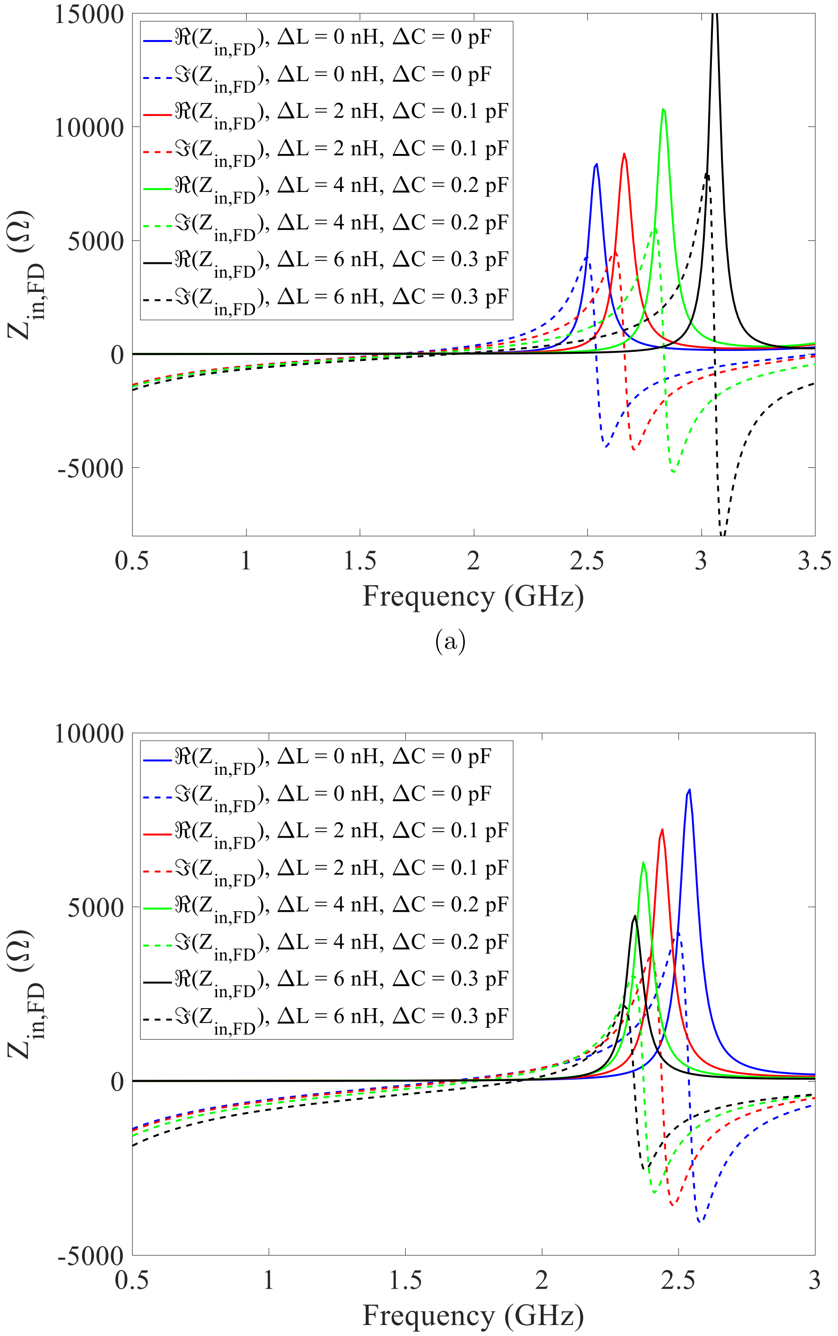

(a)

(b)

Figure 3.13: Input impedance trends for the asymmetrically loaded folded dipole antenna (a) driven arm more inductive, folded arm more capacitive, and (b) folded arm more inductive, driven arm more capacitive.

loading arrangement results in a $f_{R,N}$ point at 1.91 GHz and $f_{AR,1}$ point at 2.34 GHz. It can be found that in order to cause the same set of resonance points using the equivalent symmetrically loaded folded dipole, the required reactance values on each arms should be 28.6 nH and 0.19 pF. Thus, it can be clearly seen that for the symmetrically loaded folded dipole, although the required C value is of the same level, the required L value is much higher, and the difference in the loading values is only expected to increase with increasing amount of asymmetry.

Furthermore as an added benefit, the introduced asymmetry is expected create a greater current imbalance between the arms compared to the symmetrically loaded case, which will essentially result in a better radiation efficiency. It should be noted that since the introduced asymmetry in the loading scheme makes the currents on the two arms of the folded dipole antenna non-identical, the analytical model described in this chapter cannot be applied anymore to predict the frequencies of $f_{R,N}$ and $f_{AR,1}$. However, the equivalent symmetric case can be considered as a good starting point in order to obtain the required range of loading L and C values. An extreme case of asymmetric loading would be the driven arm loaded with only C and the folded arm loaded with only L, which will be explored in the next chapter for miniaturizing a folded dipole antenna to $1/4^{th}$ of its resonant half-wavelength (i.e., $l = \lambda/8$, or 75% miniaturized) and achieve good matching without the need of any external matching network. Thus, a smaller number of lumped components will be required for this arrangement, allowing the available space to be used more efficiently.

3.7 Summary

In this chapter, an analytical method was proposed that successfully described the input impedance profile of a reactively loaded folded dipole antenna. However, the use of this method is restricted by the following issues related to the estimation of Z_{AM}:

1. The induced-EMF method requires the dipole to be slender, but for any practical

design the dipole arm will have a considerable cross-sectional dimension.

2. The loading reactances cannot be simply added to the unloaded AM input impedance if the dipole arm is not slender, and the effects of their locations on the antenna arm will have to be considered.

3. The proposed analytical method will not work for asymmetric loading schemes since that will cause an unequal current distribution on the two arms, and thus the AM cannot be estimated by just replacing the folded dipole by an equivalent conventional dipole.

4. And finally, in practical scenarios, this analytical model will not be able to account for any significant mutual interactions between different loading elements, or parasitic reactances that might overpower the loading reactances, and also effects from feed structures.

However, in the slender limit, this model successfully reveals all the crucial trends and features of the different resonances in the input impedance profile of a folded dipole antenna without the need for time-consuming simulations, corresponding to different reactive loading cases that will be important for the realizing a miniaturized and well-matched antenna.

Chapter 4

Design of a 75% Miniaturized Folded Dipole Antenna

4.1 Introduction

In Chapter 3, it was shown that by employing an asymmetric loading scheme on the two arms of a folded dipole antenna, the two resonances $f_{R,N}$ and $f_{AR,1}$ could be brought close to each other without the need of extreme loading reactance values. In this chapter, a printed folded dipole antenna has been miniaturized to $1/4^{th}$ of its half-wavelength resonant length (i.e., $l = \lambda/8$, or 75% miniaturized) following a fully asymmetric loading scheme, where the loading inductances are placed only on the folded arm and the loading capacitances are placed only on the driven arm. Furthermore, in order to introduce an additional degree of freedom, the arm widths of the folded and driven arms are made unequal. It will be shown that the miniaturized antenna results in an enhanced radiation efficiency compared to an unloaded folded dipole antenna of the same footprint, by exploiting the benefits of introduced asymmetries that cause a greater current imbalance between the two arms of the folded dipole antenna.

A unique feed structure has been designed with only the purpose of providing a balanced

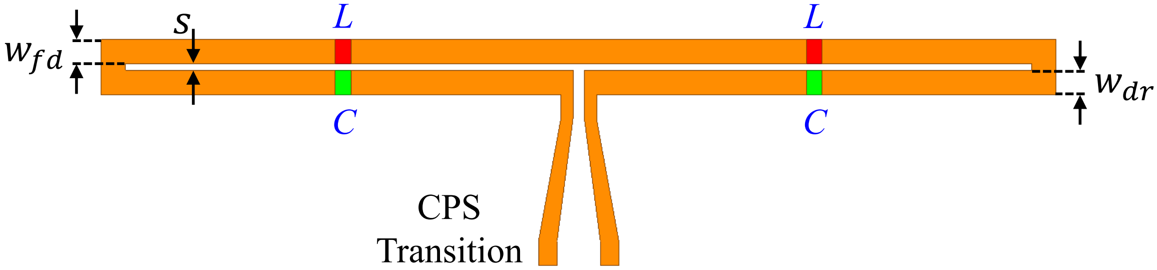

Figure 4.1: Schematic of a reactively loaded folded dipole antenna.

input current to the antenna, thus if a balanced input is already available for the antenna, the feed structure will not be necessary. It will also be shown in this chapter, how the practical considerations like the effect of the balun structure and the finite losses in the loading reactances influence the performance of the miniaturized antenna. Finally, the fabrication and measurements of the final design will be presented.

4.2 Initial Design

4.2.1 Geometry

A 40-mil-thick Megtron 4 R-5725 Laminate dielectric substrate has been considered for the design, whose relative permittivity (ε_r) and the loss tangent ($\tan\delta$) values are 4.14 and 0.005, respectively. The antenna length l was maintained at 38 mm, same as the length used for the studies in Chapter 3. The arm widths and the separation between them were made larger in order to facilitate fabrication. For generality, the driven and folded arm widths were assigned with two different width parameters: w_{dr} and w_{fd}, respectively. It was decided that from this chapter onward, the separation between the arms s will correspond to the edge-to-edge distance between the arms, unlike the center-to-center distance shown in Fig. 3.4 in Chapter 3. A balanced coplanar-strip (CPS) line was attached to the antenna that comprises a linearly-tapered transition from a 200-Ω CPS line to the 0.5 mm-wide feed gap on the driven arm of the folded dipole antenna, as shown in Fig. 4.1. Justification of using this particular 200 Ω impedance will be given later in Section 4.4 while describing the feed structure. The traces were assigned a finite conductivity of 5.8×10^7 S/m in order to simulate copper conductor, with a thickness and surface roughness of 35 μm and 0.2 μm, respectively, to model the practical losses in the conductor.

The L and C loading elements were placed asymmetrically on the folded and driven arms, respectively, at a distance $l/4$ from the ends of the antenna, such that a greater current imbalance can be ensured between the arms, and also the available space can be used more efficiently. Lossless lumped models were used in HFSS for the loading inductors and capacitors. The structure was optimized targeting a good impedance matching at 1 GHz (where the antenna will be 75% miniaturized) with respect to the 200-Ω port impedance.

4.2.2 Full-Wave Simulations and Optimization

Initially, widths of both the arms (w_{dr} and w_{fd}) and the separation between them (s) were set to 1 mm and 0.25 mm, respectively. Parametric simulations were performed by varying the loading reactances along with the individual arm widths. It was found that for L = 48.7 nH and C = 0.03 pF, very good return loss (which is a measure of how well a particular device is matched) could be obtained exactly at 1 GHz. The higher is the value of the return loss, the better is the matching. It is usually expressed as the negative of the reflection coefficient S_{11} in dB scale. The input impedance profile and S_{11} of the optimized design are shown in Figs. 4.2(a) and 4.2(b), respectively. It can be easily noticed from Fig. 4.2(a) that, due to the application of high loading inductance and small loading capacitance values, the resonances $f_{R,N}$ and $f_{AR,1}$ are now situated very close to each other with only 7 MHz separation between them. This results in $Z_{in,FD}$ at the resonance $f_{R,N}$ very close to the desired 200 Ω, and thus validates the proposed approach described in Chapter 3. The miniaturized folded dipole antenna retains an omnidirectional radiation pattern, and presents a gain of -1.0 dBi with 71.1% radiation efficiency, as compared to -11.2 dBi gain and 6.1% radiation efficiency for an unloaded folded dipole of the same footprint size at the same

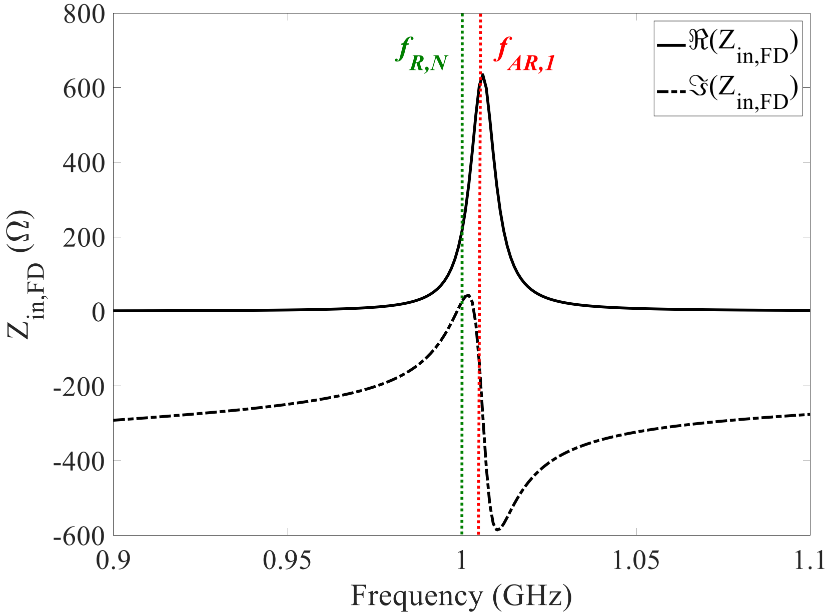

(a)

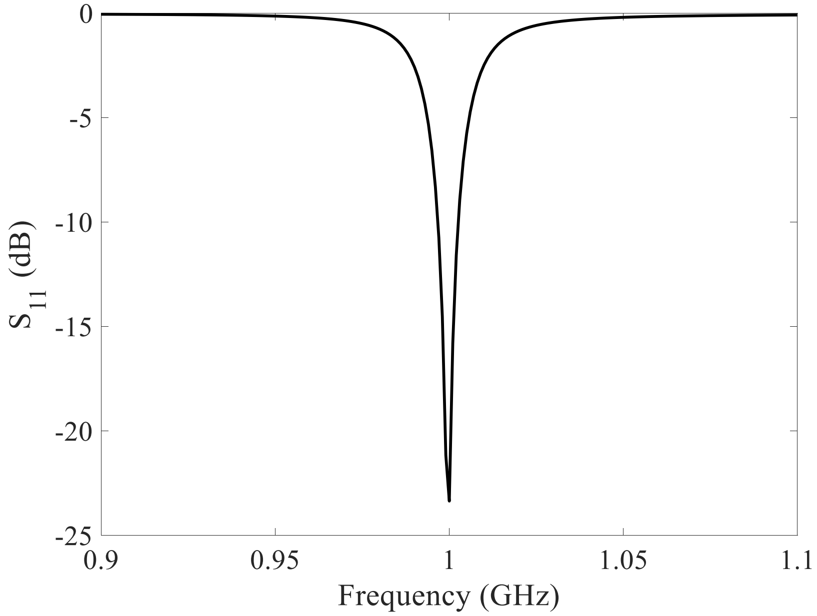

(b)

Figure 4.2: (a) Input impedance of the reactively loaded folded dipole antenna, and (b) corresponding S_{11} with respect to 200 Ω source impedance.

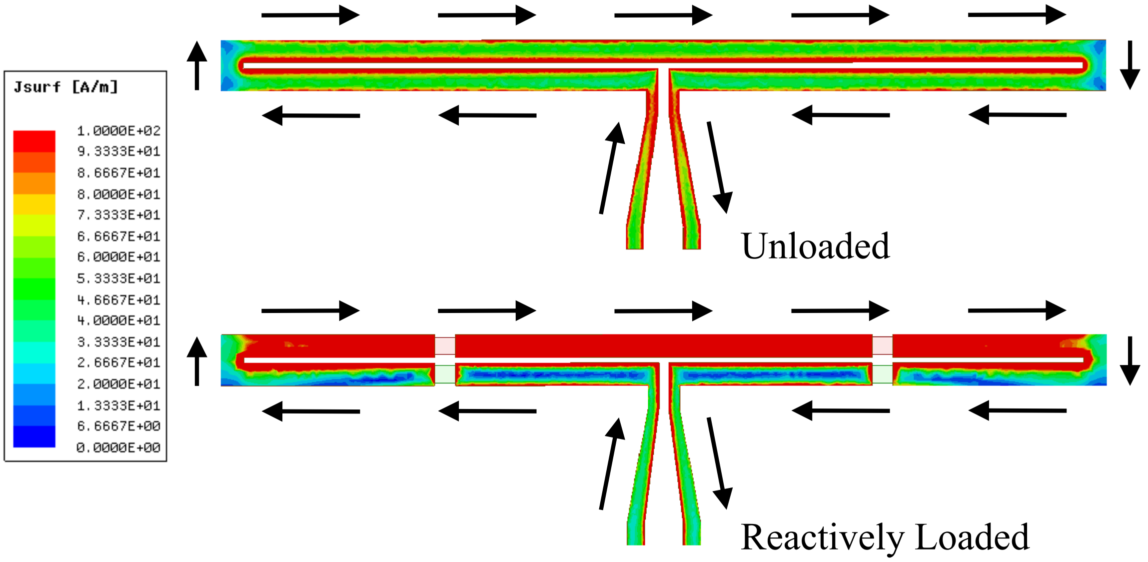

Figure 4.3: Comparison of current distributions for the unloaded and reactively loaded folded dipole antennas at 1 GHz.

frequency. The improvement of the gain and the radiation efficiency may be inferred from the current distributions on the two antennas, shown in Fig. 4.3. Both current distributions are plotted on the same scale at the frequency of 1 GHz. It can be easily seen that for the unloaded case, the current magnitudes on the two arms are contra-directed on either side of the gap and of the same magnitude, resulting in an effective cancellation of radiated fields. However, for the reactively loaded case, although the currents on the two arms remain contra-directed, the magnitude is much higher on the folded arm, which essentially produces a net unbalanced current that ultimately results in radiation, and hence a better radiation efficiency could be realized. Finally, the simulated 10-dB return-loss bandwidth of this miniaturized antenna is expectedly narrow, measuring 6 MHz.

4.2.3 Effect of Variation of Arm Widths

It is well known that the input impedance of a folded dipole antenna can be altered by varying the widths of its individual arms [66]. Thus, it was decided to introduce arm-width

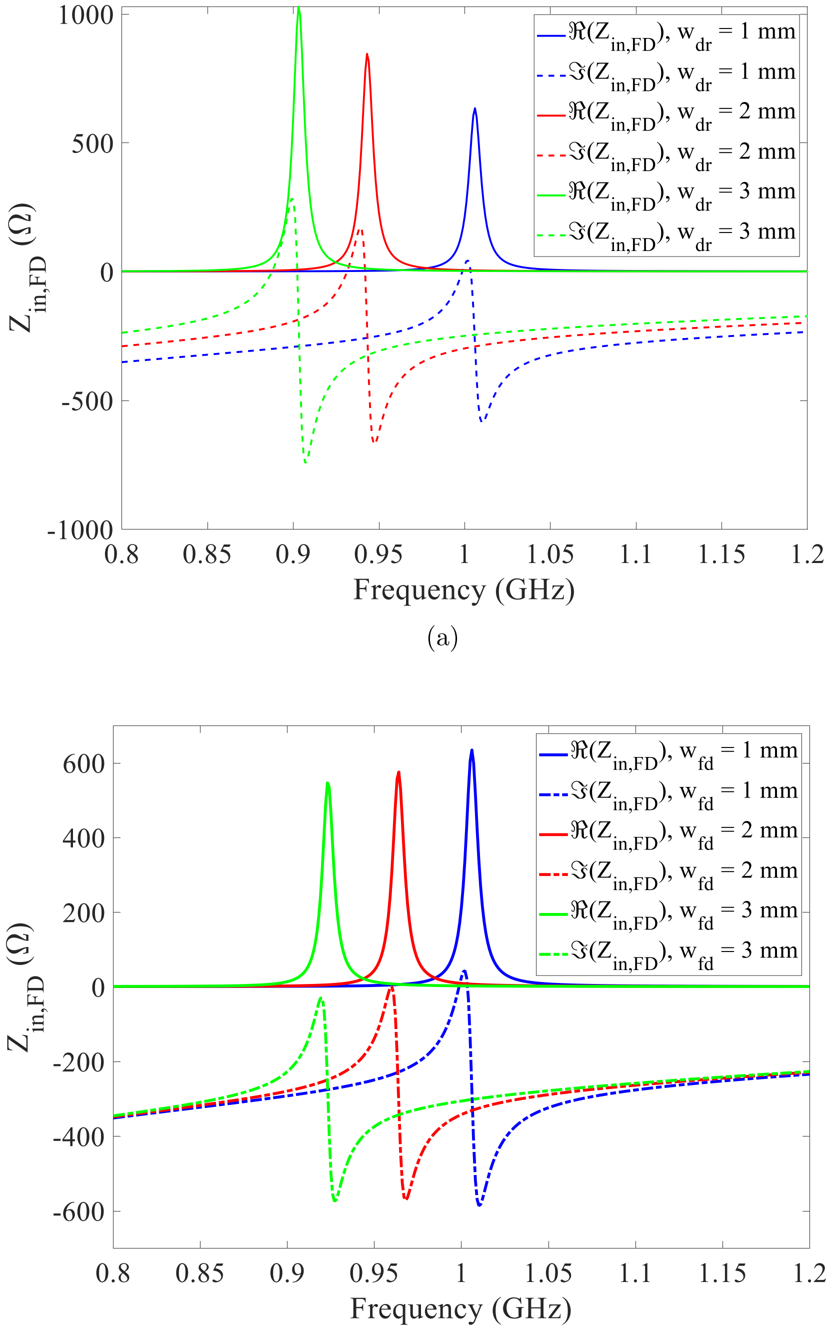

(a)

(b)

Figure 4.4: (a) Input impedance profiles as a function of w_{dr} with w_{fd} fixed at 1 mm, and b) Input impedance profiles as a function of w_{fd} with w_{dr} fixed at 1 mm.

w_{dr} (mm)	w_{fd} (mm)	$f_{AR,1}$ (GHz)	η_{rad} at $f_{AR,1}$(%)
1	1	1.006	71.10
1	2	0.964	74.04
	3	0.923	75.07
2	1	0.943	71.88
3		0.903	72.51

Table 4.1: Positions of $f_{AR,1}$ and the corresponding radiation efficiencies as functions of w_{dr} and w_{fd}.

variation as an additional design parameter in this work, such that the dependence on the loading reactance values can be reduced to some extent. The driven arm width w_{dr} and the folded arm width w_{fd} were varied separately, keeping the other arm width fixed at 1 mm. The loading reactances values were kept the same as mentioned in Section 4.2.2. The input impedance profiles corresponding to the variation of w_{dr} and w_{fd} are shown in Figs. 4.4(a) and 4.4(b), respectively. It can be seen from both the figures that increasing either of the arm width shifts the resonances further towards lower frequencies, of course at the cost of increased footprint size in the lateral direction. Moreover, $\Re(Z_{in,FD})$ at the antiresonance $f_{AR,1}$ increases with increasing w_{dr}, whereas it decreases with increasing w_{fd}, which could be useful for matching the antenna with a smaller source impedance (e.g., 50 Ω). The position of the individual antiresonances along with the corresponding radiation efficiencies are listed in Table 4.1 as functions of both w_{dr} and w_{fd}.

It can be seen that in addition to shifting the resonances towards lower frequencies, the increasing arm widths also enhance the radiation efficiency very slightly. Thus, it was decided to continue with $w_{dr} = 1$ mm, and $w_{fd} = 2$ mm for the remainder of this chapter, such that a slightly higher radiation efficiency can be obtained without increasing the footprint size significantly. The loading reactance values were readjusted to bring the return loss peak back to 1 GHz. However, instead of using lumped components, this time the loading capacitors were realized in interdigitated form with gap width C_g and finger length C_l, as shown in Fig. 4.5. It was found that for L = 43.2 nH, capacitor dimensions $C_g = 0.10$ mm, $C_l = 0.04$ mm, $C_w = 0.15$ mm, and $C_e = 0.075$ mm; again a good return loss could be obtained exactly

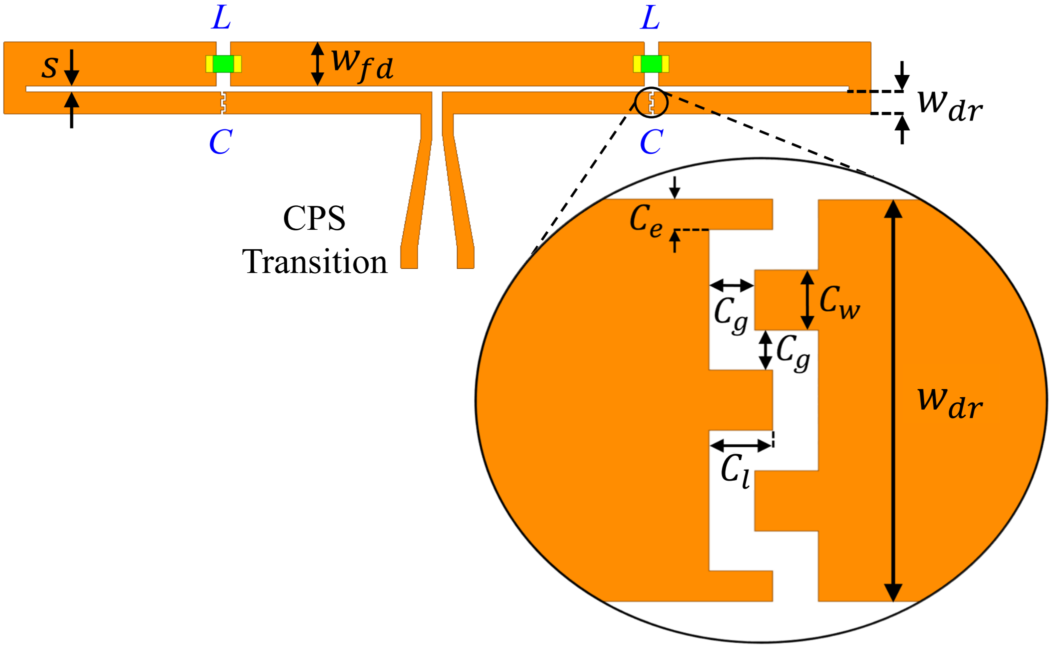

Figure 4.5: Schematic of reactively loaded folded dipole antenna with interdigitated loading capacitors, and w_{dr}=1 mm, w_{fd}= 2 mm.

at 1 GHz. The equivalent capacitance of the interdigitated structure was estimated using simulation to be approximately 5.3 fF. The input impedance profile and S_{11} of the design are shown in Figs. 4.6(a) and 4.6(b), respectively. The corresponding gain and radiation efficiency values at 1 GHz are -0.9 dBi and 72.3%, respectively, as compared to -12.2 dBi gain and 5.8% radiation efficiency of its unloaded equivalent.

4.3 Design Guidelines for Miniaturizing a Folded Dipole Antenna

Thus, although it is possible to achieve good impedance matching and radiation performance for a folded dipole antenna at generally any miniaturization level following this method, more extreme miniaturization implies increasingly narrow bandwidths, lower radiation efficiencies, and typically more extreme values for the loading reactances. Generally, the design procedure for achieving good impedance matching at a high degree of miniaturization

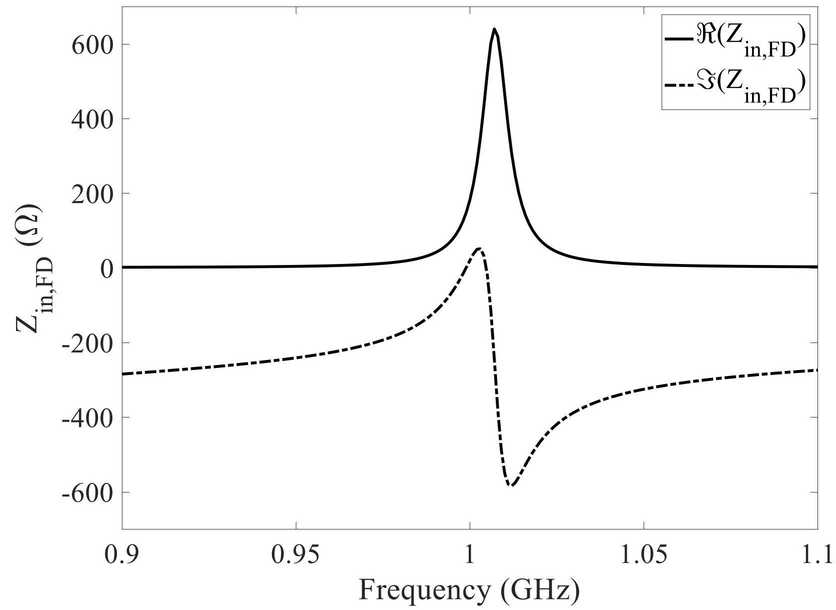

(a)

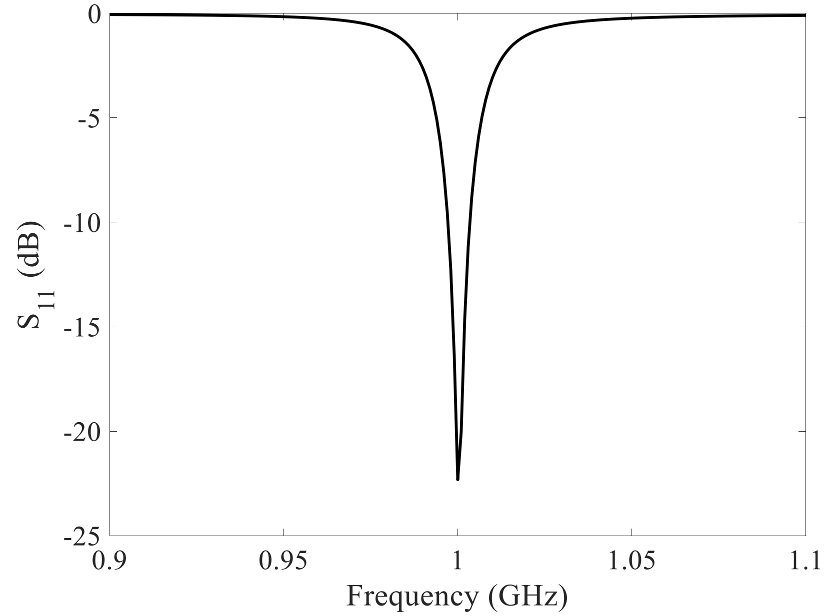

(b)

Figure 4.6: (a) Input impedance of the reactively loaded folded dipole antenna shown in Fig. 4.5, and (b) corresponding S_{11} with respect to 200 Ω source impedance.

can be summarized as follows:

1. Choose a target frequency of operation or, conversely, the desired degree of miniaturization for a given physical length.
2. Introduce high series L-loading on the folded arm in order to bring $f_{AR,1}$ below the target frequency.
3. Introduce series C-loading on the driven arm to bring $f_{AR,1}$ around the target frequency, and $f_{R,N}$ very close to $f_{AR,1}$.
4. Optimize the loading values and the arm widths simultaneously, e.g., using parametric full-wave simulations, to achieve good return loss at the target frequency.

4.4 Practical Considerations – Effect of Feed Structure, Inductor Losses

Since the folded dipole antenna requires a balanced input, and the measurement devices use a standard 50-Ω reference impedance, it is necessary to design a balun structure that can transform a 50-Ω unbalanced coaxial line to a 200-Ω balanced coplanar strip line. The choice of this particular impedance transformation was motivated by the availability of a surface-mount balun transformer (Mini Circuits TC4-25+), which is a center-tap transformer with a 1:4 turns ratio and can be operated over a bandwidth of 500 MHz to 2.5 GHz. A microstrip-based feed structure has been designed to house the balun transformer and a Micro-Miniature Coaxial (MMCX) surface mount connector, which will be fed via a 50 Ω MMCX cable. The total length of the feed structure is 23.5 mm (0.08λ at 1 GHz), which is much smaller than conventional printed microstrip-to-CPS balun structures that require approximately quarter-wavelength (or sometimes even longer) transition lengths [85–89]. It must be remembered that the feed structure used here is only for the purpose of converting an unbalanced input current to balanced output current, and given the choice of having a balanced input available for the antenna, it would not be necessary. The feed structure along with the antenna is shown in Fig. 4.7.

In order to determine the frequency response of the feed layout, it was simulated in HFSS with 50 Ω and 200 Ω port impedances at the input and output sides, respectively. The balun transformer could not be included in the simulation due to the unavailability of an accurate full-wave model. However, the scattering parameters of the feed layout obtained using HFSS could be co-simulated with the published scattering-parameter data of the transformer [90] using the Keysight Advanced Design System (ADS) microwave circuit simulator. The overall generalized scattering parameters of the feed structure are shown in Fig. 4.8. It can be seen that the feed structure has an excellent broadband, low loss and well matched response around the frequency range of interest. Thus, it can be ensured that the feed will not introduce significant dispersion into the antenna response and have a minimal effect on the radiation efficiency of the antenna, a proof of which has been demonstrated in Appendix A.

The loading inductance was achieved using a Coilcraft 0603HP-33N inductor, which has a nominal value of 35.45 nH at 1 GHz as determined from its manufacturer-provided SPICE model [91]. This value is deliberately chosen to be smaller than the 43.2 nH used in the simulation of the miniaturized antenna so as to prove that this technique does not need to rely on the availability of a particular design value of lumped loading inductor, if the inductance may be otherwise compensated (as would be needed, for example, to compensate tolerances on off-the-shelf components and the effect of variations in landing patterns). In the next section, it will be shown that any effect on the antenna S_{11} response caused by the use of a smaller-valued inductance and the feed structure, indeed, can be neutralized simply by modifying the folded arm slightly and fine-tuning the loading capacitance.

It is important to note at this point that every practical lumped inductor is associated with some amount of ohmic loss, which is usually quantified as the quality factor (Q_{ind}) of the inductor and can be represented as an equivalent series resistance. The Q_{ind} of the

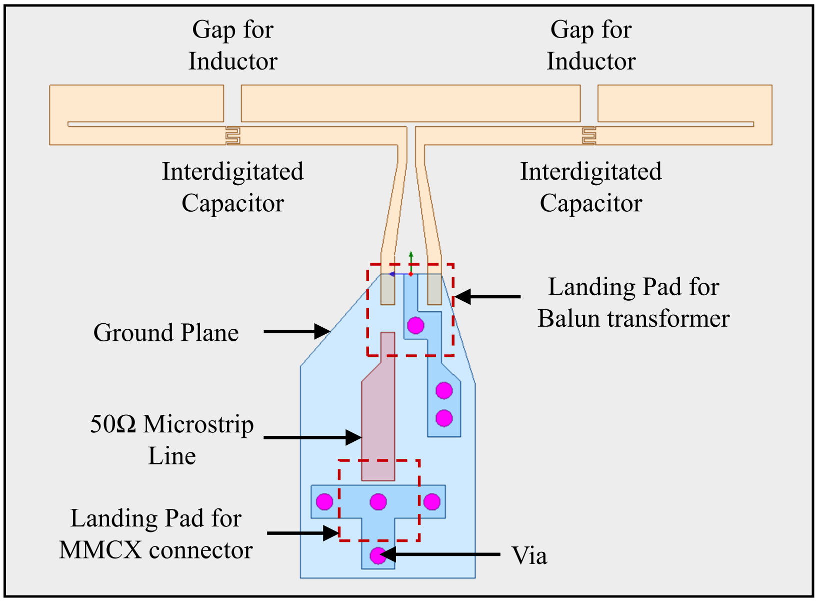

(a)

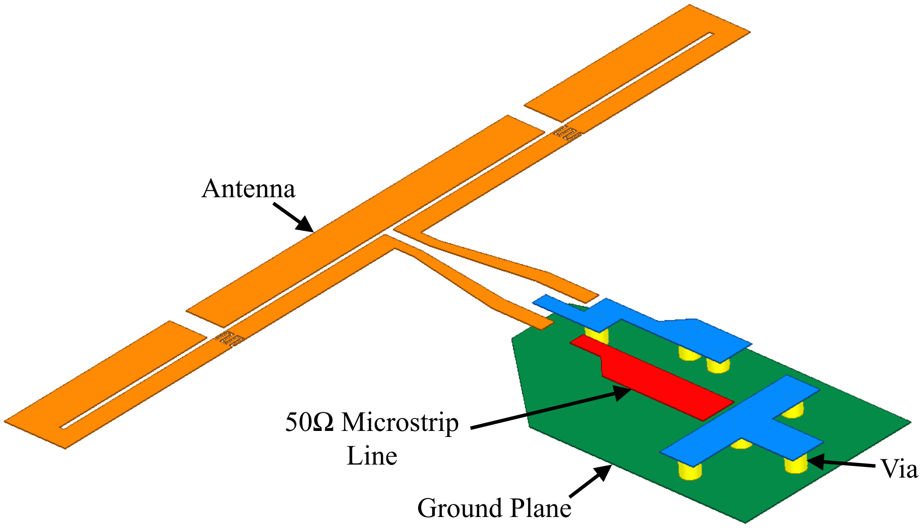

(b)

Figure 4.7: (a) Layout of miniaturized antenna with the feed structure., and (b) isometric view of the antenna with the feed structure.

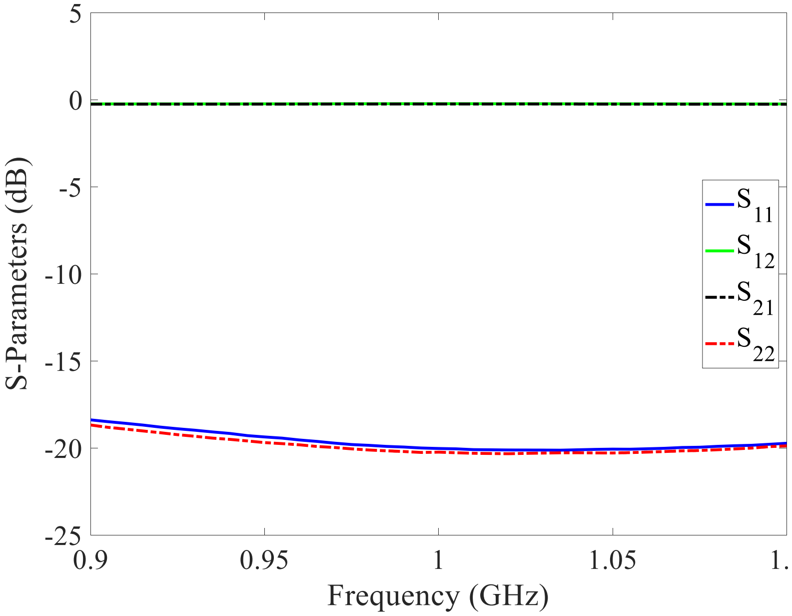

Figure 4.8: Frequency response of the feed structure.

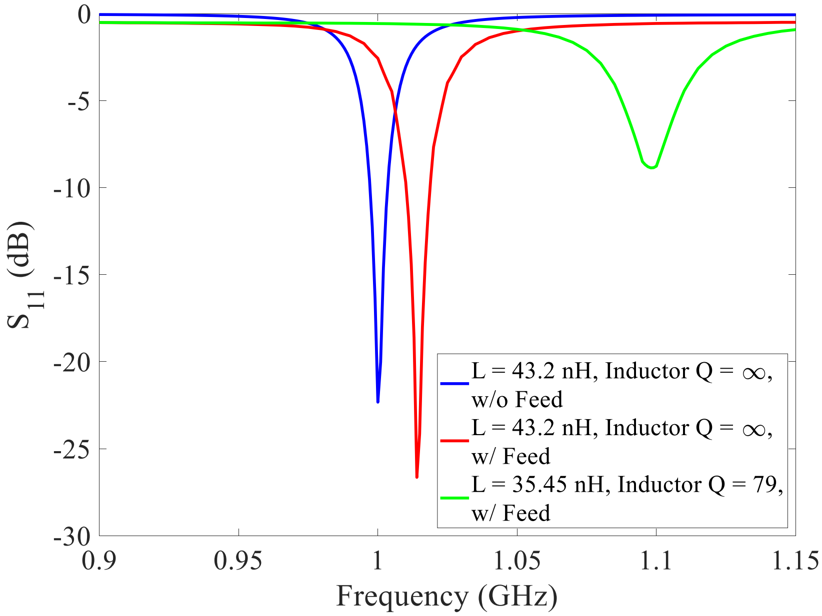

Figure 4.9: Comparison of simulated S_{11} data for the antenna with L = 43.2 nH, $Q_{ind} = \infty$, without and with the feed structure vs. with L = 35.45 nH, $Q_{ind} = 79$ with feed structure.

selected inductor was found to be 79 at 1 GHz, suggesting an equivalent series resistance of 2.8 Ω. Two HFSS simulations were performed in order to study the effects of the feed structure and the finite Q_{ind} of the lumped inductor. In the first simulation, the antenna was simulated in the presence of the feed structure, but keeping the loading inductance value unchanged at 43.2 nH. In the second simulation, the 43.2 nH inductor was replaced by the chosen 35.45 nH Coilcraft inductor with a 2.8 Ω resistor in series. The corresponding return loss responses were compared with the return loss response shown in Fig. 4.6(b). The comparison is shown in Fig. 4.9. As mentioned earlier, the feed structure does not significantly affect the return loss of the antenna, and only shifts the peak of the return loss by 14 MHz, from 1 GHz to 1.014 GHz. However, in the second simulation, the use of a smaller value of loading inductance shifts the peak return-loss value by 98 MHz. The return loss has also degraded by 13.45 dB, which occurs both due to the mismatch caused by a different loading inductance value and the added loss to the structure through the finite inductor Q_{ind}.

4.5 Final Design

As mentioned earlier, all these effects can be compensated and good matching can be realized at 1 GHz for the whole structure by optimizing the different antenna parameters. For the selected lumped inductor, in order to bring the return-loss peak to 1 GHz and compensate for the lost inductance, two perpendicular sections of width $w_p = 1$ mm and length l_p were added to the folded arm at the inductive loading locations as shown in Fig. 4.10. The length of these additional sections was fine-tuned to provide the necessary additional inductive loading. In addition, the finger-length (C_l) of the interdigitated capacitor was readjusted to vary the overall loading capacitance and re-establish the required proximity of $f_{AR,1}$ and $f_{R,N}$ around 1 GHz. All other antenna parameters were kept unchanged. It was found that, for $l_p = 2.11$ mm and $C_l = 0.64$ mm (approximate equivalent loading capacitance 102.9 fF),

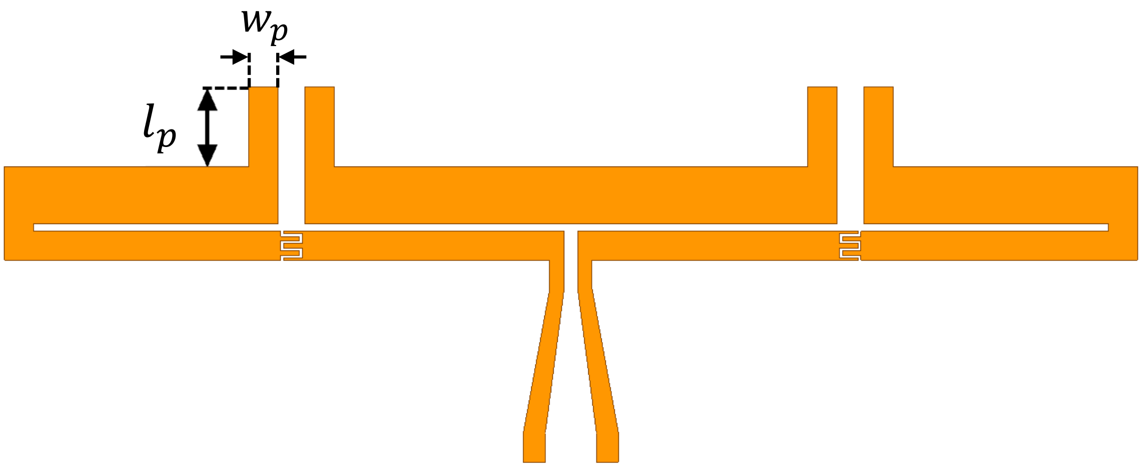

Figure 4.10: Antenna layout with modified folded arm (lumped loading inductances not included).

again a good return-loss response was obtained with S_{11} = -31.78 dB at 1 GHz and a 10-dB bandwidth of 15 MHz. The enhancement of bandwidth can be attributed largely to the finite losses introduced to the lumped loading inductors.

The radiation efficiency is expected to be strongly reduced by the Q_{ind}, but is also susceptible to additional insertion losses incurred due to multiple scattering outside the antenna operating bandwidth, where the antenna is strongly mismatched to the feed. To quantify both sources of power dissipation, an overall radiation efficiency $\eta_{rad,O}$ can be defined for the antenna with the feed structure, which may be estimated using the following equation:

$$\eta_{rad,O} = \eta_F \times \eta_{rad,A}. \tag{4.1}$$

Here, η_F is the efficiency of the feed structure in transmitting the accepted power, and $\eta_{rad,A}$ is the radiation efficiency of the antenna including the parasitic effects of the feed layout, which can slightly shift the antenna resonance. This was obtained from HFSS by directly exciting the antenna in the presence of the feed layout, excluding the balun transformer. The feed efficiency η_F can be written in terms of the scattering parameters of the feed structure including the balun structure (subscript F) and the antenna (subscript A), as follows:

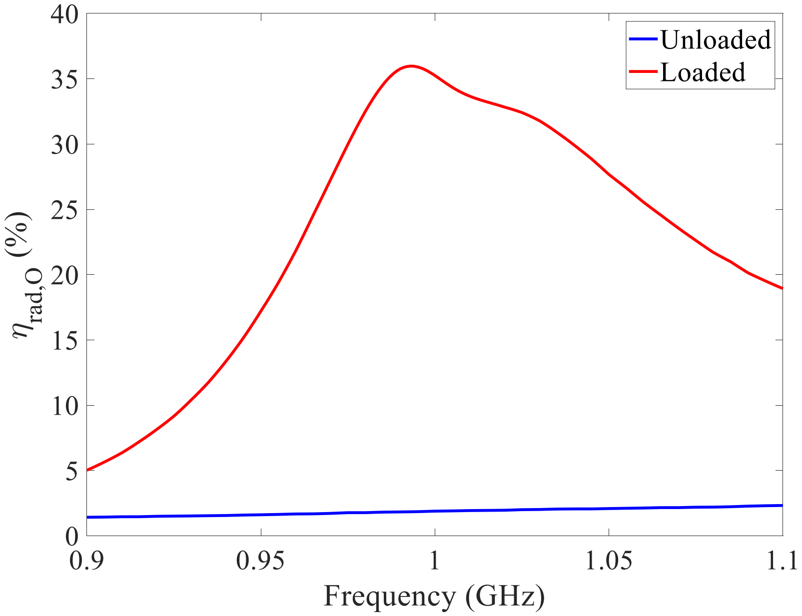

Figure 4.11: Comparison of overall radiation efficiencies ($\eta_{rad,O}$) of unloaded and reactively loaded folded dipole antennas, in the presence of the feed structure.

$$\eta_F = \frac{|S_{21,F}|^2 \times (1 - |S_{11,A}|^2)}{1 - \left| S_{11,F} + \dfrac{S_{12,F} S_{21,F} S_{11,A}}{1 - S_{22,F} S_{11,A}} \right|^2}. \tag{4.2}$$

The derivation of equation 4.2 is detailed in the Appendix A.

Using equation 4.1, a comparison was made between the reactively loaded folded dipole antenna and an unloaded folded dipole antenna having the same overall footprint, both in the presence of the feed structure, and shown in Fig. 4.11. It can be easily seen that, although reduced due to the introduction of losses, the use of asymmetric loading to enable impedance matching nevertheless results in a substantially better radiation efficiency than the unloaded case. $\eta_{rad,O}$ of the loaded folded dipole antenna was found to be 35.3% at 1 GHz (∼34% at the edges of the 10-dB return loss band), whereas the radiation efficiency is just 1.9% for the unloaded folded dipole antenna at the same frequency. It is also worth comparing the simulated realized gains of the two antennas, which takes into account both the matching and the radiation efficiency, and can be related more directly to the radiated

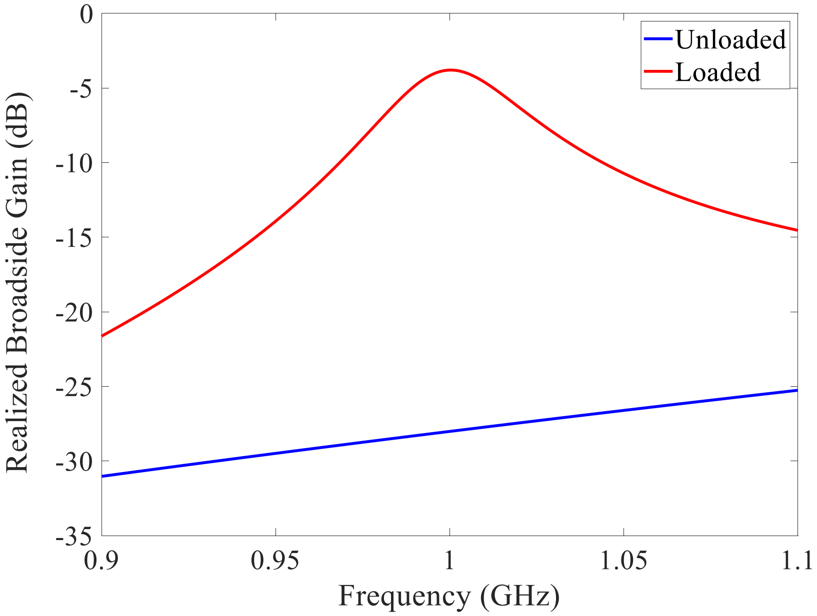

Figure 4.12: Comparison of realized gains of unloaded and reactively loaded folded dipole antennas, in the presence of the feed structure.

power. It can be seen from Fig. 4.12 that, as expected, the loaded folded dipole antenna has a much better realized broadside gain (-3.80 dB) than its unloaded counterpart (-28.02 dB) at 1 GHz. It is important to note that the observed S_{11} bandwidth, radiation efficiency, and antenna quality factor are well within the Chu-Harrington limit, which is described in detail in Appendix B.

4.6 Comparison of Radiation Properties with an Equivalent Conventional Dipole

So far, the radiation properties (i.e., radiation efficiency and gain) of the miniaturized folded dipole antenna were compared to that of its unloaded counterpart. However, it is also important to compare the same with respect to an equivalent conventional dipole antenna.

The equivalent conventional dipole has the same length of 38 mm with an arm width of 1 mm, and is loaded with an inductance of 65.5 nH inductance on each half of the antenna

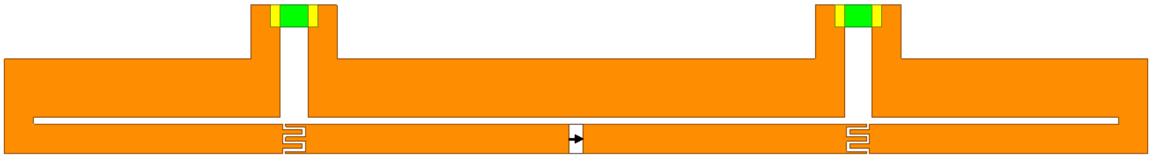

(a)

(b)

Figure 4.13: (a) Lumped inductor loaded miniaturized folded dipole antenna with the CPS transition removed, and (b) equivalent inductively loaded conventional dipole antenna.

in order to reduce its half-wavelength resonance (which is also its first resonance) to 1 GHz. Also, for fairness of comparison, the loading inductors used for the conventional dipole were assigned the same quality factor (Q_{ind}=79) as those used for the lumped inductor loaded miniaturized folded dipole antenna. This results in a reference antenna that is both the same length and has a resonance at the same frequency as the proposed miniaturized folded dipole antenna. Furthermore, in order to factor out the effect of matching, both the antennas were excited using ideal lumped ports in HFSS, with the port impedance being exactly the same as the antenna input resistance at resonance, such that both the antennas are very well matched. Thus, the CPS transition shown in Fig 4.10 has also been removed. Both the antennas exhibited a simulated return loss level greater than 34 dB. The two simulated antennas are shown in Fig. 4.13.

It was found that both the loaded miniaturized folded dipole antenna and the loaded conventional dipole have almost equal radiation efficiency and realized gain values (37.17% radiation efficiency and -3.79 dB realized gain for the miniaturized folded dipole antenna, as compared to 36.16% radiation efficiency and -3.89 dB realized gain for the equivalent conventional dipole antenna), which establishes that the miniaturized folded dipole antenna works at least as well as an equivalent-length loaded conventional dipole operating at the same frequency. However, two things must be noted here: (1) HFSS lumped ports are highly idealized and impractical, and (2) the input impedance of the loaded conventional dipole antenna cannot be as easily or widely engineered in order to match to a given port impedance by changing its loading values and/or the dimensions like the miniaturized folded dipole antenna. Furthermore, since the input resistance of the conventional dipole antenna at its miniaturized resonance is only 31.4 Ω, it still requires a matching network in order to match to practical source impedances like 50 Ω. However, the miniaturized folded dipole antenna could be matched without requiring any such network. It is also noteworthy that the CPS transition used in the miniaturized folded dipole antenna was inspired by the availability of the particular balun transformer used in the final design, but technically it could be just as easily matched to a balanced 50 Ω source.

4.7 Fabrication and Measurement

4.7.1 Fabrication

The optimized structure was fabricated using an LPKF ProtoLaser U3 milling machine that uses a laser to pattern designs on a dielectric substrate. The lumped inductors were soldered onto the antenna surface, along with the balun transformer and the MMCX surface-mount connector, and the vias were created using LPKF 0.9 mm copper rivets inserted into the substrate using a manual rivet punch and then soldered. The fabricated prototype is shown in Fig. 4.14.

4.7.2 Measurement

The return loss characteristics of the fabricated antenna were measured using a Keysight PNA-X (model N5244A) vector network analyzer. Early prototypes exhibited a matching frequency slightly higher than 1 GHz, suggesting that the inductance of the surface-mount inductor component used in this study was slightly smaller than its reported nominal value.

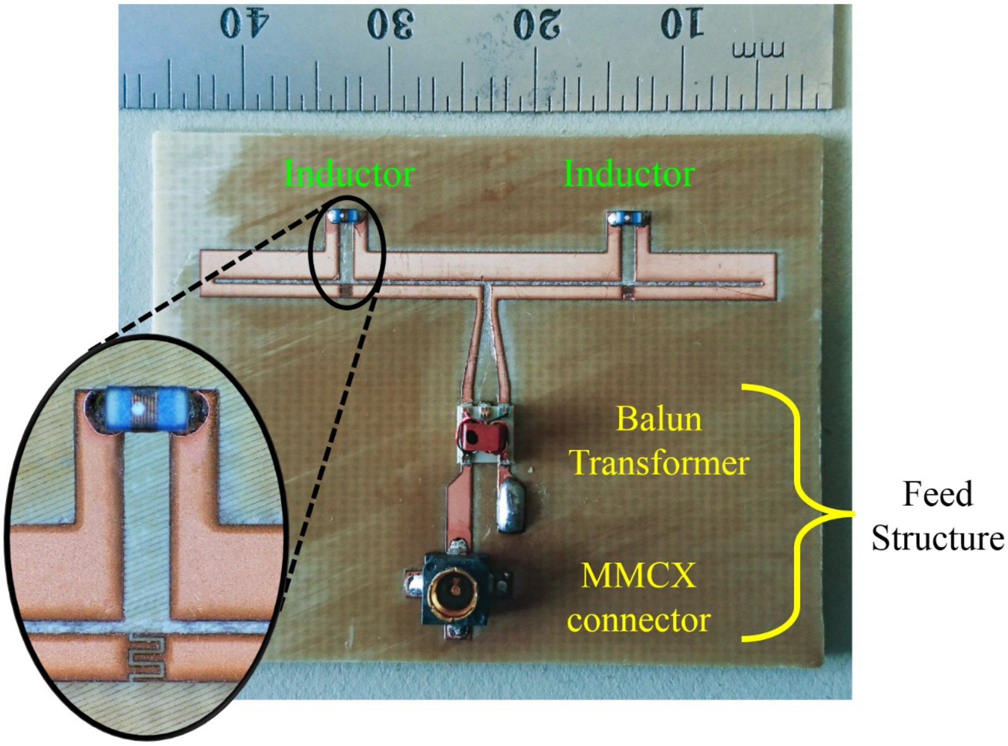

Figure 4.14: Fabricated prototype of the reactively loaded miniaturized folded dipole antenna.

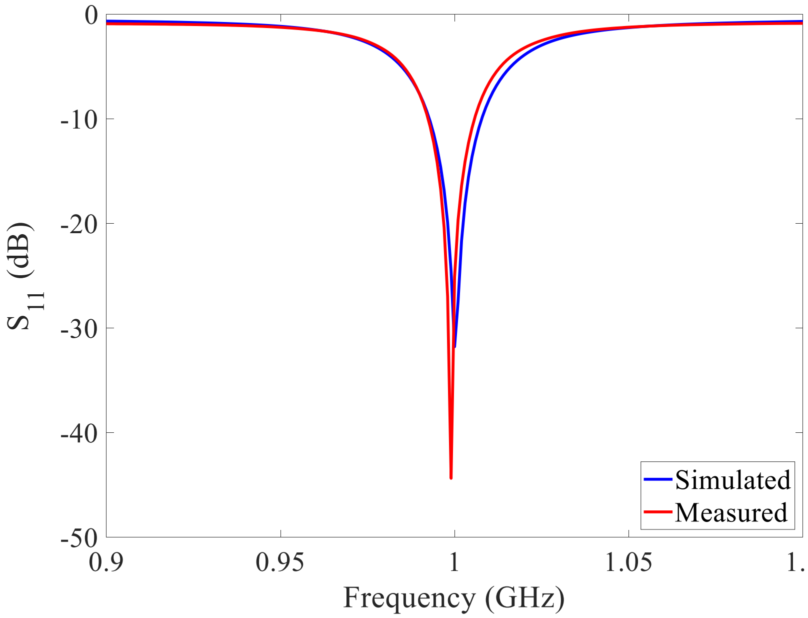

Figure 4.15: Simulated vs. measured S_{11}.

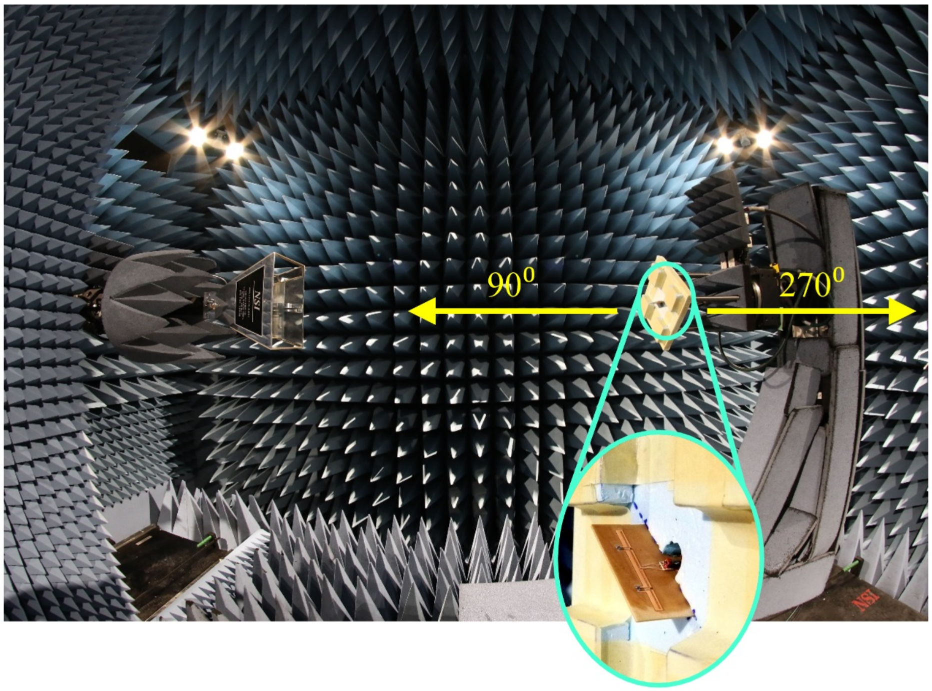

Figure 4.16: Experimental setup for measuring the normalized radiation patterns (E-plane is the horizontal plane).

Thus, the length l_p of the perpendicular sections was further increased to 2.75 mm (keeping the other antenna parameters unchanged) in order to bring the return-loss peak closer to 1 GHz. Excellent -44.36 dB matching was obtained for the fabricated antenna at 0.999 GHz ($\sim$75% miniaturized). It was found through simulations that a reduction in the loading inductance from its reported nominal value of 35.45 nH to 34.15 nH (which is within the specified $\pm$5% tolerance value of the inductor) predicts the observed return-loss maximum at 0.999 GHz. The measured return loss was compared to the simulated result described in Section 4.5 ($l_p = 2.11$ mm, L = 35.45 nH), and shown in Fig. 4.15. Excellent agreement was found between the simulated and measured return-loss responses with a 10-dB return loss bandwidth of approximately 14 MHz (1.4%).

The radiation patterns were measured at 0.999 GHz inside a near-field anechoic chamber manufactured by NSI-MI Inc. [92], using a dual-ridged horn antenna that has a bandwidth from 750 MHz to 10 GHz as the transmitting antenna while the fabricated folded dipole antenna was used as the receiver. Due to the lack of experimental capabilities to accurately

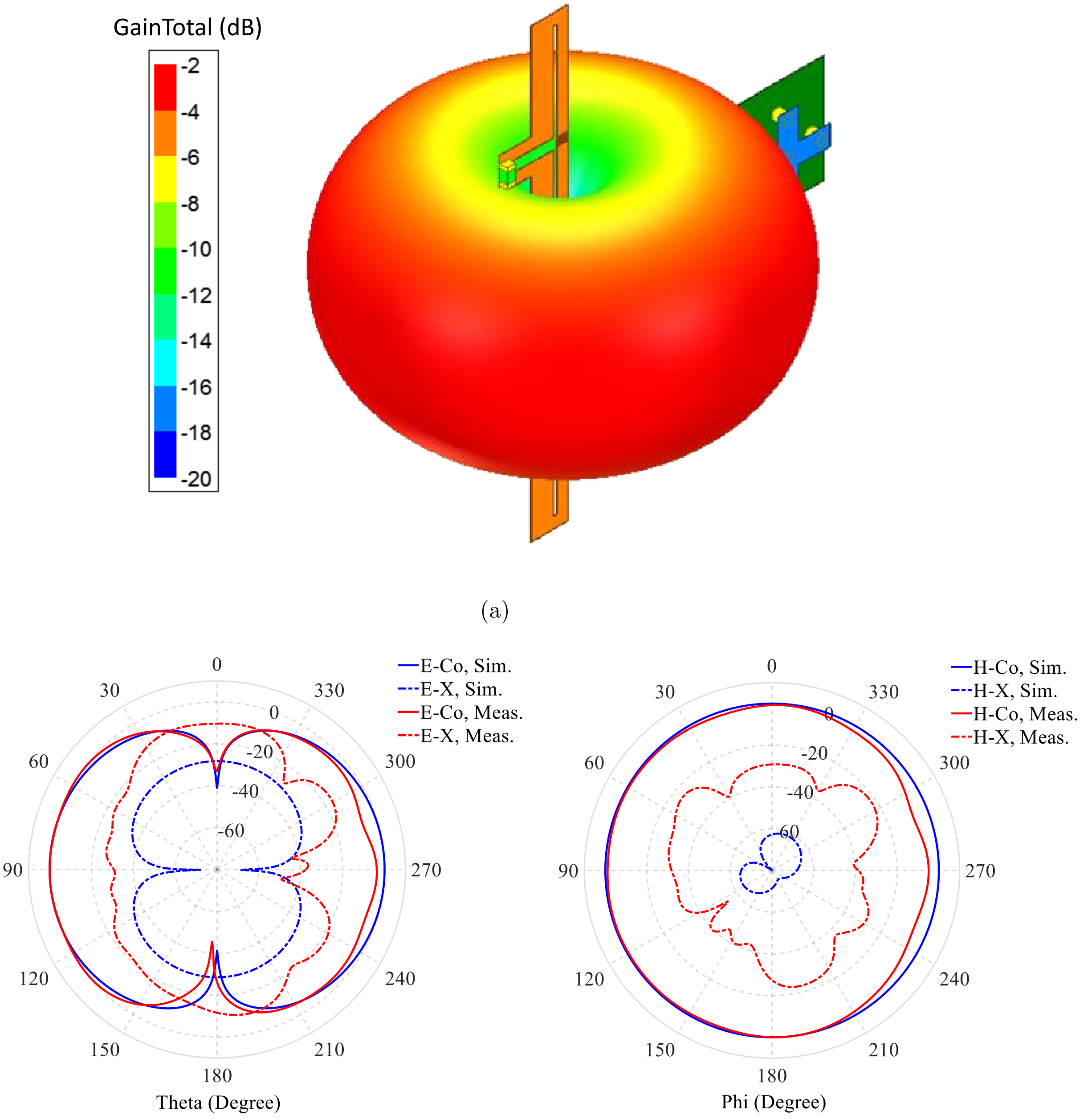

(a)

(b) (c)

Figure 4.17: (a) Simulated 3D radiation pattern of the reactively loaded folded dipole antenna at 0.999 GHz in presence of the feed structure as parasitic; and comparison of normalized radiation patterns at 0.999 GHz (simulated vs. measured): (b) E-plane, (c) H-plane.

measure gain, only the normalized radiation patterns have been presented. The measurement setup is shown in Fig. 4.16. The simulated 3-D radiation pattern at 0.999 GHz was obtained in presence of the feed structure acting as a parasitic, and is shown in Fig. 4.17(a). It should be noted that, since the parasitic feed structure does not include the balun transformer, there are no actual currents on the feed structure other than the currents induced by the antenna, and thus the feed structure has only a very minimal effect on the simulated pattern. The corresponding normalized E- and H-plane patterns were compared with their measured counterparts, and a good agreement was found between them, as shown in Figs. 4.17(b) and 4.17(c), respectively. The measured co-pol to cross-pol separation at broadside direction (90°) is approximately 30 dB. It was noticed from the simulations that the added vertical segments at the L-loading locations have a minimal contribution to the cross-pol magnitudes. The observed differences between the simulated and measured patterns, particularly in the cross-pol magnitudes, can be attributed to the radiation from the actual currents on the feed structure of the fabricated antenna, and also potentially to the multipath reflections from the measurement setup inside the chamber. Finally, the slight discrepancies evident in the E- and H-plane patterns at angles around 270° are due to blockage by the vertical mounting stand, as indicated in Fig. 4.16.

4.8 Comparison with Other Miniaturized Dipole-like Antennas

In this section, the miniaturized reactively loaded folded dipole antenna described in Section 4.5 has been compared with some other highly miniaturized conventional and folded dipole antennas found in the literature. The summary of the comparison has been presented in Table 4.2.

In [30], examples can be found where a conventional dipole antenna has been miniaturized to the levels of approximately 80% by means of using simple reactive loading techniques.

Reference	Antenna Type	Miniaturization		Fractional Bandwidth	η_{rad}	Matching Technique
		Technique	Level			
[30]	Conventional Dipole	Circular Disk + Helix Loaded	77%	1.44%	95.5%	Stub Matching
		Spherical Disk + Helix Loaded	83%	0.74%	93.3%	
[36]	Conventional Dipole	Transmission-Line Metamaterial	64%	1.7%	27.0%	Dispersion Engineering by Varying the Loading Reactances
[40]	Conventional Bowtie	Transmission-Line Metamaterial	47%	4.0%	47.8%	Dispersion Engineering by Varying the Loading Reactances
[30]	Folded Dipole	Helical Arms in the Shape of a Sphere	83%	0.87%	97.4%	Multiple Folded Arms
		Helical Arms in the Shape of a Cylinder	83%	0.57%	97.7%	
[73]	Folded Monopole	180° Metamaterial Phase Shifter at the Antenna End	55%	2.5%	80.0%	Higher Input Resistance of the Folded Monopole
[74]	Folded Monopole	0° Metamaterial Phase Shifter at the Antenna End	80%	1.3%	72.3%	Multiple Folded Arms
[77]	Folded Monopole	Conventional Phase Shifter at the Antenna End	80%	0.83%	81.7%	Multiple Folded Arms
Proposed	Folded Dipole	Series-LC Loading	75%	1.5%	35.3%	Embedded Impedance Engineering

Table 4.2: Comparison between the proposed miniaturized folded dipole antenna and some other highly miniaturized conventional and folded dipole antennas found in the literature.

The antenna was loaded simultaneously with a series L and a shunt C by employing helical arms and by adding circular or spherical disks at the ends of the dipole antenna, respectively, in order to realize a high degree of miniaturization. Although the antennas resulted in a very high radiation efficiency of greater than 90%, the resulting bandwidths are of the same order as the miniaturized folded dipole antenna reported in this chapter. However, the major demerits of these miniaturized conventional dipole antennas are the following: (1) external matching networks are required for achieving good impedance matching, and (2) large lateral dimensions due to the application of top-hat loading.

The miniaturized conventional dipole antenna reported in [36] employs a transmission line metamaterial, where the dispersion properties of the metamaterial loaded transmission line were manipulated by varying the loading reactances in order to achieve both miniaturization and matching. As a result, the antenna does not require an external matching network. However, since the antenna is essentially composed of a two-conductor transmission line, it usually suffers from poor radiation efficiencies due to oppositely directed currents on the two conductors. The antenna reported in [36] has a lower radiation efficiency compared to the miniaturized folded dipole antenna described in Section 4.5, although having a lower miniaturization level. A similar technique has been explored in [40] to miniaturize a bowtie antenna. Although the miniaturized bowtie antenna exhibits a slightly higher radiation efficiency than the proposed miniaturized folded dipole antenna, it must be noted that the corresponding miniaturization level is also much lower (∼47%).

As mentioned in Section 2.2.3, the traditional miniaturization techniques for folded dipole antennas usually focus on using the series resonance f_R, rather than the antiresonance $f_{AR,1}$, due to its ease of matching and higher radiation efficiency. The same can be noticed from the examples found in [30], [73], [74], and [77]. Additionally, these miniaturized folded dipoles employed multiple folded arms, which not only helped in realizing higher input resistance such that matching can be enabled without external matching networks, but also resulted in a very high radiation efficiency owing to the co-directed currents on all the arms. However, the overall footprint of these kind of miniaturized folded dipole antennas are much larger than the one described in this chapter due to the usage of multiple folded arms, and higher the level of miniaturization, more the number of folded arms that are required to realize the necessary input resistance.

Thus, although the radiation efficiency of the proposed miniaturized folded dipole antenna is not very high compared to some of the examples listed in Table 4.2, it has the following advantages: (1) low overall footprint, (2) simple miniaturization process that uses only series reactive loading components, (3) flexible matching scheme that allows to match the miniaturized folded dipole antenna to an arbitrary source impedance, at a given miniaturization level without significantly increasing the antenna footprint. Moreover, as it will be described in more detail in the next chapter, low radiation efficiencies are tolerable for sensor applications, which is the intended application of the proposed miniaturized folded dipole antenna.

4.9 Summary

This work demonstrated that engineering the input impedance of a printed folded dipole antenna using asymmetric series-LC loading and variable arm widths can enable excellent impedance matching, co- to cross-polarization separation, and improved radiation efficiency, even when it is highly miniaturized (∼75%) at the operating frequency. The miniaturized antenna does not require any external matching network and has attractive radiation performance suitable for sensor applications. The measured results are in excellent agreement with the simulated results.

A fully printed equivalent antenna can be developed, which will not require any lumped components and thus will not be susceptible to the tolerances in off-the-shelf lumped component values, and also will be easier and less expensive to fabricate. An example of a 75% miniaturized fully printed folded dipole antenna will be shown in the next chapter, which would be a suitable choice for sensing applications that require real-input-impedance matching. Furthermore, although the technique presented in this work was used to engineer the input impedance in order to match to a real source impedance, it may more generally be used to realize complex input impedances for conjugate matching for some sensor applications like RFID tag antennas, an example of which will also be demonstrated in the next chapter.

Chapter 5

Applications in Sensing

5.1 Introduction

In Chapter 4, an example of an inherently matched but highly miniaturized folded dipole antenna was demonstrated using both simulations and measurements, where good impedance matching was realized at a 75% miniaturization level by properly choosing the loading reactance values and using unequal arm widths as an additional degree of freedom. It was also shown that the miniaturized folded dipole antenna exhibits a much better radiation efficiency and realized gain compared to its unloaded counterpart of the same footprint, which was achieved by employing an asymmetric reactive loading scheme. Furthermore, a unique feed structure had been designed in order to provide a balanced input current to the antenna, and its effects on the antenna performance were described in detail.

In this chapter, the design of a fully printed version of the aforementioned miniaturized antenna will be demonstrated, which is generally scalable and can be useful as sensor antennas that require a real input impedance. The fully printed antenna has been designed to operate at the UHF ISM frequency band specified for sensing applications in North America. Furthermore, the idea of input-impedance engineering will be extended for realizing a RFID tag antenna that requires conjugate matching with a complex input impedance. Both the antennas will be validated using measurements.

5.2 Sensor Antennas with Real Input Impedance

5.2.1 Background

With the exponential growth in numbers and capabilities of sensor-based systems in recent years, the technology related to their associated antennas has been continuously improved. The challenge is, of course, to design an antenna that is small and low profile for the purposes of portability, ease of integration with small sensor circuits, low cost and which exhibits a reasonable radiation performance. A narrow bandwidth and a moderate radiation efficiency usually suffice for these kinds of applications, since for most applications only a very small amount of data need to be transmitted/received over a rather short distance.

One of the most intriguing examples is perhaps Machine-to-Machine (M2M) technology, which commonly refers to the communications between computers and other mobile devices with various smart sensors and systems. This technology is extensively being used in emerging applications like Internet of Things (IoT), which is expected to revolutionize the way people interact with their surrounding environment, such as at home, work, in transportation, cities or rural areas, hospitals, or at school. In this technology, various sensors will be attached to different household objects, industrial instruments and devices, vehicular platforms etc., which are then going to be connected to the cloud via internet, with or without limited human intervention [93, 94]. A variety of different types of antennas have been reported in the literature for M2M and IoT applications, among which dipole/monopole antennas [95–101] and Inverted-F (IF) antennas [102–107] are some of the preferred choices as they offer a low-profile and inexpensive design solution with good omnidirectional radiation patterns.

Another potential application of sensors where real input impedances are used are body-centric communication systems (also known as Body-Area Networks or BAN) that include wearable and body-worn systems, biomedical sensors, in-body implantable monitoring devices, short-range emergency communications etc. The antennas are often designed to be flexible, and since a body-worn antenna is usually in close proximity to, or surrounded by, human tissue, it should be designed with consideration for losses and potential shifts in operating frequency [108, 109]. Preferred antenna choices include patch-type [110–116], Inverted-F [117–120], and dipole/monopole antennas [121–129].

It is noteworthy that for most of these sensor systems, the antennas are only used as a part of the RF transceiver module for establishing communication, and the actual sensor elements are connected to the transceiver module through an Analog-to-Digital Converter (ADC) and a microcontroller unit [108]. The antennas are typically connected to the rest of the system by a transmission line that is already matched to the corresponding transmitter/receiver on the other end and has a real characteristic impedance. This in turn requires the antennas to have an equal real input impedance in order to ensure maximum power transfer.

Sub-GHz UHF bands are often preferred for all the aforementioned applications due to their more reliable propagation characteristics, large communication range, and good in-building penetration. Also, these frequency bands are often less crowded than the 2.4 GHz ISM band. One such example is the 915 MHz band (902-928 MHz), which is an allocated ISM band in North America. In this section, a fully-printed and 75% miniaturized ($l = \lambda/8$) folded dipole antenna will be designed for operation in the 915 MHz band using the same technique described in Chapter 4.

5.2.2 Design and Simulation

For the fully printed folded dipole antenna to operate at 915 MHz at a 75% miniaturization level, the length of the antenna l was chosen to be 41 mm. The dielectric substrate used for this design is the Megtron 4 R-5725 Laminate that has a thickness of 40 mil, same as the substrate used in Chapter 4. Once again, a similar loading scheme was used, i.e., capacitive loading on the driven arm and inductive loading on the folded arm. However,

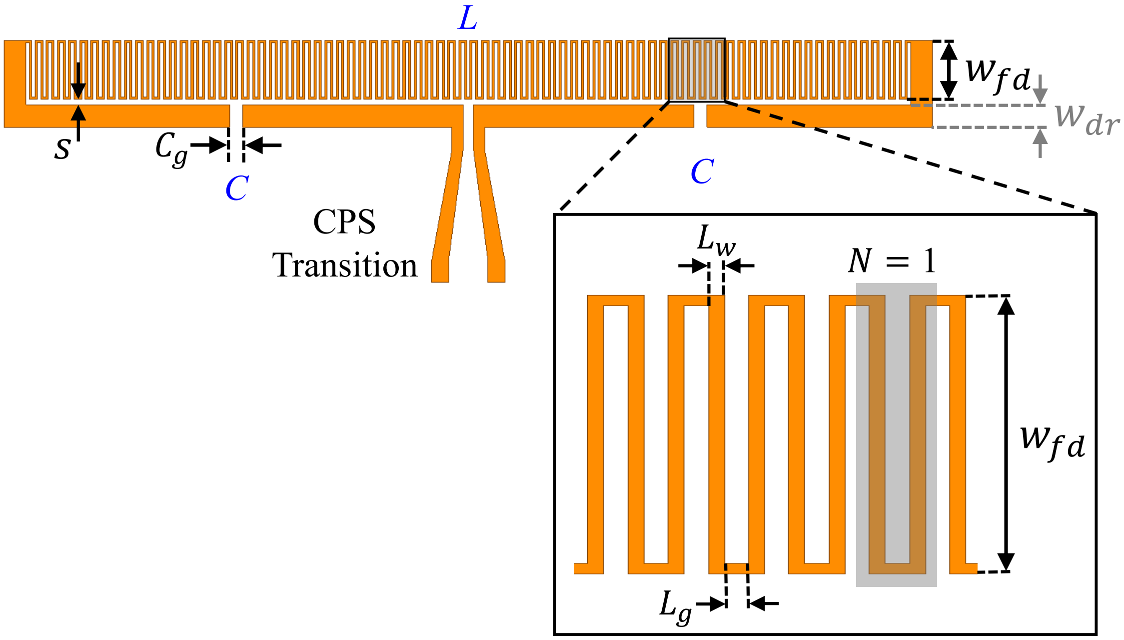

Figure 5.1: Schematic of the fully printed folded dipole antenna.

this time the loading inductor was realized by meandering the folded arm, comprising N turns, with each turn having a side length w_{fd}, width L_w and a separation L_g between two successive traces. Furthermore, it was found that for this design a simple gap of width C_g on the driven arm would provide sufficient capacitive loading, thus an interdigitated capacitor was not necessary. The capacitive gaps were placed at a distance $l/4$ from the antenna ends. A detailed schematic of the fully printed antenna is shown in Fig. 5.1.

Parametric simulations were performed by varying N, w_{fd}, L_w, L_g, and C_g; the driven arm width w_{dr} was kept unchanged at 1 mm, again same as the design described in Chapter 4. The simulations were performed using both HFSS and ADS considering the same feed structure and balun transformer. It was found that for $N = 80$, $w_{fd} = 2.75$ mm, $L_w = 0.10$ mm, $L_g = 0.15$ mm, and $C_g = 0.60$ mm, a very good 18.8 dB return loss was achieved at 915 MHz, with a 23 MHz 10-dB return loss bandwidth. However, it must be noted here that due to the presence of a lot of fine features in the structure, the simulation became very time- and memory-consuming (110 GB for one frequency point). As a result, the parametric simulations were performed after relaxing the convergence criteria slightly. Thus, a slight

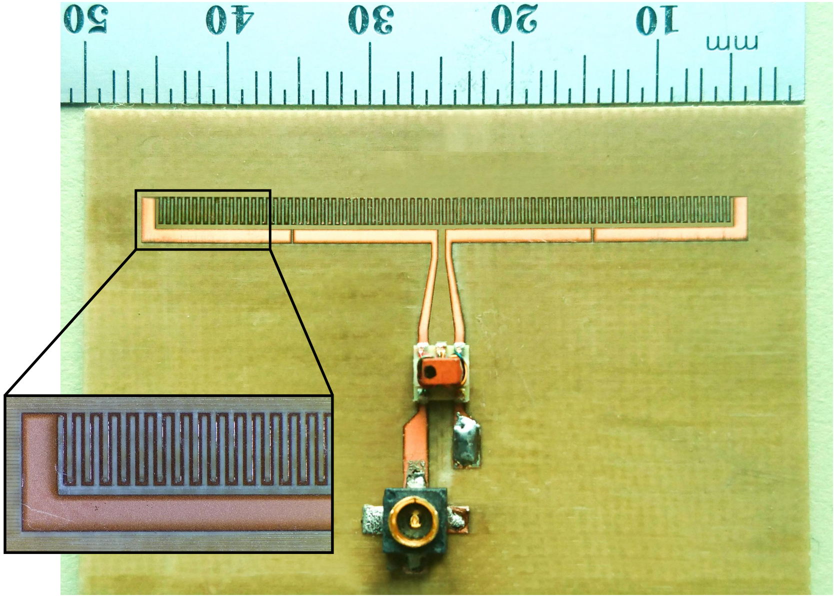

Figure 5.2: Fabricated prototype of the fully printed folded dipole antenna.

deviation can be expected while comparing the measured return loss data to the simulated in the future. Finally, the corresponding overall radiation efficiency ($\eta_{rad,O}$) and realized gain at 915 MHz were found to be 28.3% (~27% at the edges of the 10-dB return loss band) and -4.91 dB, respectively. It can be noticed that the overall radiation efficiency for the fully printed case is slightly smaller compared to the value reported for the same level of miniaturization in Chapter 4, where lumped discrete inductors were used. The reduction of the radiation efficiency is caused potentially due to the lower quality factor and distributed nature of the printed loading inductor, and hence increased losses.

5.2.3 Fabrication and Measurement

The optimized structure was fabricated using the aforementioned LPKF ProtoLaser U3 milling machine. The balun transformer and the MMCX surface-mount connector were soldered at the respective places. A photograph of the fabricated prototype is shown in Fig. 5.2. The return loss response of the fabricated antenna was measured and compared with the simulated return loss, and shown in Fig. 5.3. It can be seen that, due to the relaxation

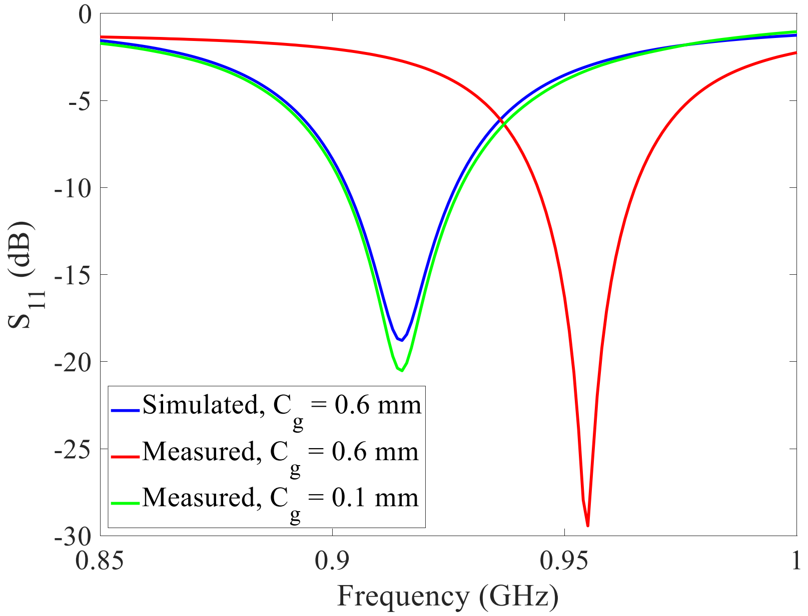

Figure 5.3: Simulated vs. measured S_{11}.

of the simulation convergence, the peak return loss frequency did not occur exactly at 915 MHz, instead it was found to have shifted by 40 MHz (∼4%) to 955 MHz. In order to bring the return loss peak back to 915 MHz, it was decided to only change the loading capacitance. Thus, a second prototype was built with a decreased C_g, such that the actual loading capacitance value is increased and the resonances of the antenna shift towards lower frequencies. It was found that for $C_g = 0.1$ mm, the measured return loss peak occurs exactly at 915 MHz with a comparable return loss level of 20.5 dB. Also, the measured 10-dB bandwidth is 25 MHz, which spans almost the entire bandwidth of specified 902-928 MHz.

Once again, the simulated 3-D radiation pattern was obtained for the fully printed folded dipole antenna at 915 MHz in presence of the parasitic feed structure, and is shown in Fig. 5.4(a). The corresponding E- and H-plane patterns were also measured at 915 MHz in the anechoic chamber using the same measurement setup and the dual-ridged horn antenna, as described in Chapter 4. The measured normalized E- and H-plane radiation patterns were then compared with the simulated data, and shown in Figs. 5.4(b) and 5.4(c), respectively.

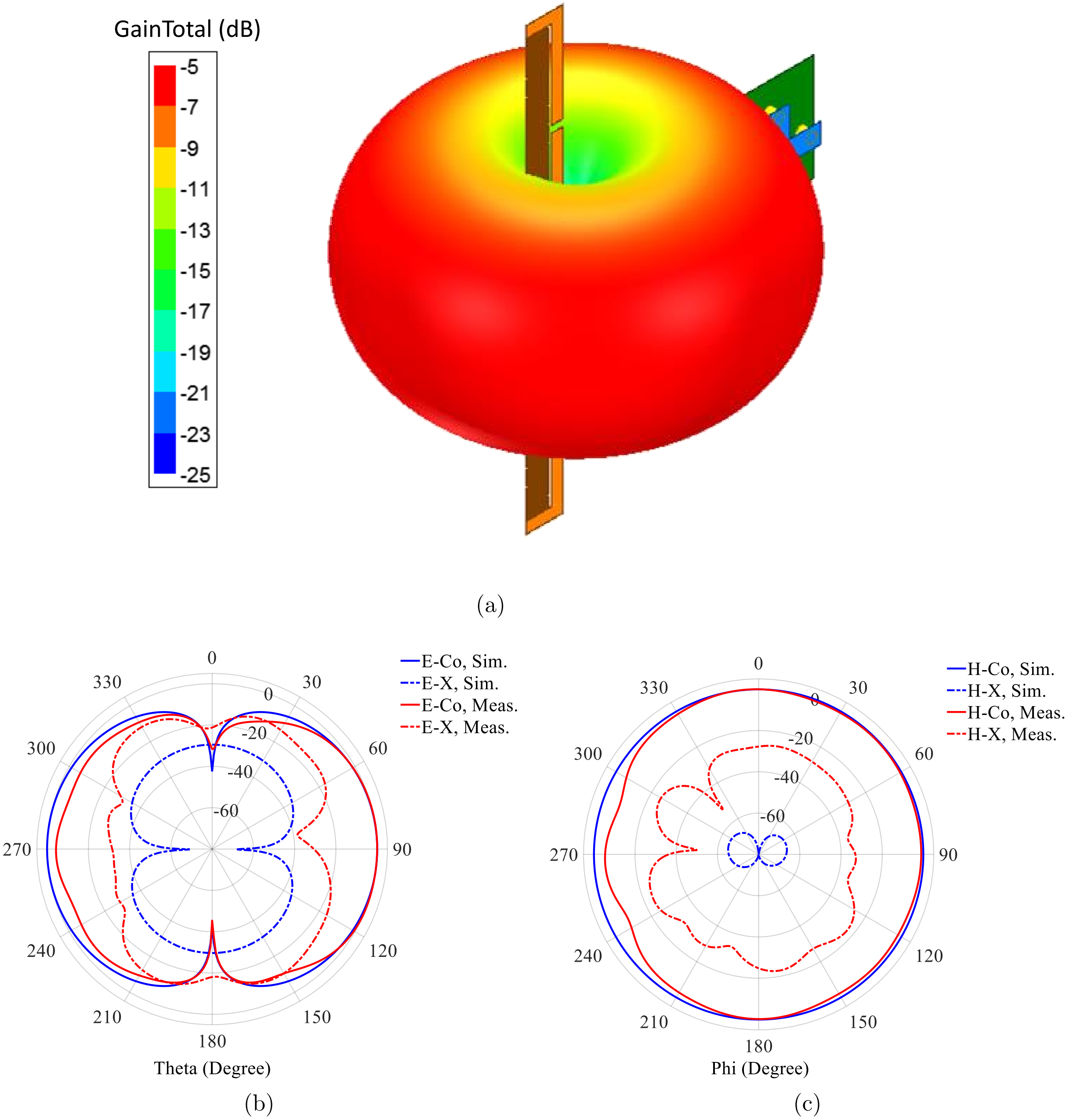

(a)

(b)

(c)

Figure 5.4: (a) Simulated 3D radiation pattern of the fully printed folded dipole antenna at 915 MHz in presence of the feed structure as parasitic; and comparison of normalized radiation patterns at 915 MHz (simulated vs. measured): (b) E-plane, (c) H-plane.

The measured co-pol to cross-pol separation at broadside direction (90°) is approximately 30.7 dB. Since the simulated pattern data were obtained incorporating the parasitic effect of the feed without the balun transformer, the observed differences between the simulated and measured cross-pol patterns could once again be attributed to the radiation from the actual currents on the feed structure of the fabricated antenna, including the multipath reflections from the measurement setup inside the chamber. Moreover, the slight deviations seen in the E- and H-plane patterns at angles around 270° occur due to the blockage created by the vertical mounting stand, as can be seen from Fig. 4.16.

5.3 Sensor Antennas with Complex Input Impedance

5.3.1 Background

Radio Frequency Identification (RFID) technology has become very popular in recent years and is being used in a multitude of applications, e.g., asset identification, manufacturing, distribution logistics and goods flow systems, personal healthcare, safety and security that involves automatic identification and remote tracking of objects [130–132]. RFID is also a prime example of a sensor technology requiring matching to a complex, rather than a real, input impedance. The idea of communicating to an object by using scattered signals was first introduced by H. Stockman in 1948 [133], although a similar idea had already been used by the British during the World War II to identify friendly or enemy aircrafts using passive radar reflectors mounted on the friendly aircrafts. After the early developments in the 1970s, RFID has emerged as a cheap, reliable and largely adopted technology in the 21^{st} century, following the standards developed in the 1990s and the recent advances in silicon technology [134].

A RFID system consists of a scanning unit, also known as the interrogator or a reader, and transponders or tags which are usually mounted on objects that need to be tracked. The reader communicates with the tags and collects information about the objects onto which the tags are mounted. The tags can be classified into three different categories based on their operating principle: passive, semi-passive, and active [135]. Among the three types, passive tags are simplest and cheapest, and will be studied in this section. The tags are typically composed of a transmitting antenna and an integrated circuit (IC) chip. They do not have any internal power source and use the signal transmitted by the reader to power up the IC chip, which then responds to the reader by backscattering its unique signature.

A suitable antenna for the tag must be cheap, low profile and lightweight, and since a very small bandwidth is usually required, miniaturized antennas are the obvious choices for this role. Furthermore, the commercially available RFID IC chips are traditionally highly capacitive, thus the tag antennas need to have an inductive input impedance in order to realize good conjugate matching and ensure maximum power transfer between the antenna and the chip.

Once again, dipole antennas are one of the preferred choices for RFID tags due to their simplicity and low fabrication cost. Miniaturization is usually done by meandering the arms of a dipole antenna [136–140] or sometimes realizing the meandered antenna on a high permittivity dielectric substrate [141]. However, it must be noted that a miniaturized dipole antenna is highly capacitive. Thus, in order to conjugately match to a capacitive IC chip, additional matching networks are usually employed, which helps realizing an inductive input impedance for the antenna. Typical examples of these matching networks include T-match [130, 140–142], inductively coupled loop [130, 139, 143, 144], or the placement of parasitic elements, such as a metal strip, next to the dipole [138, 144], where the dimensions of the matching networks and their position with respect to the dipole antenna are varied in order to achieve good matching.

Alternatively, loop antennas have also been used as RFID tags [145–147]. However, although electrically small loop antennas are inherently inductive, additional matching networks were often employed in order to ensure maximum power transfer with the IC chip. Typical examples of loop-type RFID tags can be found in [146, 147], where the radiating loop is accompanied by an inductively coupled feeding loop, and the corresponding mutual impedance between the two loops is varied by changing their relative positions in order achieve good matching.

Naturally inductive folded dipole antennas have also been employed as tag antennas [148–150]. In [148], a 0.19λ-long folded dipole antenna has been reported with a read range of 2.5 m. The antenna had been bent twice in order to form circular-shaped loads at the ends, and the input impedance of the antenna was tuned by varying the inner and outer radii of these circular loads. The folded dipole antennas reported in [149] and [150] are optimized for operation in the vicinity of a conductive plane, which is known to degrade the performance of dipole-like antennas when placed in close proximity of the antenna. The folded dipole antenna reported in [149] incorporates multiple folded arms and a tuning stub, and exhibits a simulated read range of 3 m for its 0.36λ length in free space. Furthermore, the antenna reported in [150] uses offset feeding and one open end in order to realize the necessary input impedance, however this work does not specifically discuss the tuning mechanisms that would be required to realize any arbitrary complex antenna input impedance. Nevertheless, the antenna demonstrates a free-space read range of 5.8 m for its 0.27λ length.

Finally, apart from dipole and loop antennas, examples can be found where inverted-F [151–156] and patch antennas [132, 157–160] were also used as RFID tags.

In this section, a 75% miniaturized ($l = \lambda/8$) folded dipole antenna will be designed for the aforementioned UHF-ISM band of 902-928 MHz and its performance will be tested as a RFID tag. The antenna will not require any additional matching network, and once again good matching will be enabled by engineering the locations of $f_{R,N}$ and $f_{AR,1}$ by means of varying the loading reactance values and the arm widths.

5.3.2 Design and Simulation

Once again, the length of the antenna was set to $l = 41$ mm in order to realize a 75% miniaturized antenna with respect to the center frequency of 915 MHz, and the same 40-mil-thick Megtron 4 R-5725 Laminate dielectric substrate was considered for the design. Before performing the optimization, a particular IC chip was selected for the study. The Higgs® 4 chip from Alien Technology exhibits an input impedance equivalent to an 1800 Ω and a 0.95 pF capacitor in parallel and a reading sensitivity of -18.5 dBm, which is essentially the wake-up power of the IC [161]. Thus, at the 915 MHz, the input impedance of the chip becomes $18.4 - j181.2$ Ω.

It is important at this point to define two parameters that are traditionally used to assess the performance of a RFID tag. As mentioned earlier, the antenna input impedance (Z_a) needs to be the conjugate of the IC input impedance (Z_{ic}), i.e., $Z_a = Z_{ic}^*$. Thus, an antenna-IC power transfer efficiency τ can be defined as [162]:

$$\tau = \frac{4 \cdot \Re(Z_a) \cdot \Re(Z_{ic})}{|Z_a + Z_{ic}|^2}. \tag{5.1}$$

The parameter τ represents the matching between the antenna and the IC chip, and can have values between 0 (totally mismatched) to 1 (perfectly matched). The second parameter is the read range of the tag (d_{tag}), which is essentially derived from the well-known Friis transmission equation, and can be calculated using the following equation [162]:

$$d_{tag} = \frac{\lambda}{4\pi} \sqrt{\frac{\chi_{pol} \cdot G_{r,tag} \cdot EIRP}{P_{ic}}} \tag{5.2}$$

where λ is the wavelength corresponding to the operating frequency, χ_{pol} is the polarization mismatch factor, which takes the value of 1 if both the reader and the tag antennas have the same polarization, and 0.5 for the case when one of the antennas is circularly polarized and the other is linearly polarized. $G_{r,tag}$ is the realized gain of the tag antenna, and can be given as:

$$G_{r,tag} = \tau \cdot \eta_{r,tag} \cdot D_{tag} \tag{5.3}$$

where $\eta_{r,tag}$ and D_{tag} are the radiation efficiency and directivity of the tag, respectively, at the operating frequency. $EIRP$ is the regulated equivalent isotropically radiated power of the reader antenna, and under the RFID emission regulation in North America the maximum of reader $EIRP$ can be 4 W. Finally, P_{ic} refers to the wake-up power of the selected IC chip.

Unlike the previous cases where the miniaturized antenna was designed to match with a real input impedance, this time the two resonances $f_{R,N}$ and $f_{AR,1}$ do not need to be in close proximity with each other, and since the input impedance of the antenna is inductive only between these two resonances, matching has to be attained somewhere in this frequency range. Thus, a wider difference between these two resonances will essentially result in a larger range of workable frequencies, over which conjugate matching can be performed by adjusting the real and imaginary parts of the antenna input impedance as functions of the loading reactance values. It can be recalled from Table 3.1 that as the driven arm was becoming more inductive (increase in L on driven arm), or/and the folded arm more capacitive (decrease in C on folded arm), the difference between $f_{R,N}$ and $f_{AR,1}$ was increasing. Thus, for the design of the proposed RFID tag antenna, the loading scheme was reversed, i.e., inductive loading was placed on driven arm and capacitive loading on folded arm. However, it must be noted here that the reversing of the loading scheme does not change the basic impedance trends with respect to the inductive or capacitive loading on the folded dipole antenna.

It had been mentioned in Section 5.2.2 that in order to obtain accurate simulation results for a fully printed antenna structure, considerably high computational resources would be required, particularly owing to the presence of the fine features in the antenna structure in the form of the meandered inductor (as shown in Fig. 5.1). Thus, although a fully printed prototype should ideally be designed for the tag antenna in order to minimize the fabrication cost, a discrete lumped inductor was decided to be used for this design, which would still substantiate the proposed technique. Two perpendicular segments of length l_p were added at the inductor loading locations in order to reduce the dependence on the particular design value of the loading inductance, thus any commercially available inductor with a smaller inductance value would be applicable to the design. Furthermore, it was found that again a

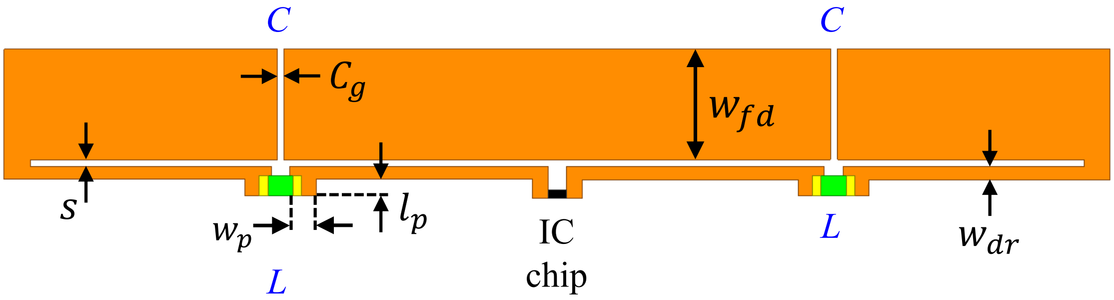

Figure 5.5: Schematic of proposed RFID tag antenna.

simple gap of width C_g on the folded arm would suffice as the loading capacitor. Both the inductive and capacitive loading were placed at a distance $l/4$ from the antenna ends. A schematic of the proposed RFID tag antenna is shown in Fig. 5.5.

Parametric simulations were performed by varying the loading reactance values along with the arm widths in order to get the input impedance of the antenna as close as the target impedance, i.e., Z_{ic}^*, as possible. For the desired 75% miniaturization level, the loading inductance was realized using a Coilcraft 0603HP-43N inductor, which has a nominal inductance value of 44.9 nH and quality factor of 72 at 915 MHz. It was found that for $w_{dr} = 0.50$ mm, $w_{fd} = 4.20$ mm, $C_g = 0.25$ mm (equivalent capacitance ≈ 4.8 fF), $s = 0.25$ mm, $l_p = 0.62$ mm, and $w_p = 1$ mm, the antenna exhibited an input impedance of $Z_a = 24.9 + j181.7\ \Omega$ at 915 MHz, which is very close to Z_{ic}^* at the same frequency. This in turn resulted in very good matching at 915 MHz, with corresponding $\tau = 0.98$. A comparison between the provided Z_{ic}^* and simulated Z_a has been shown in Fig. 5.6(a), and the corresponding plot of τ is shown in Fig. 5.6(b). Finally, the simulated radiation efficiency at 915 MHz was found to be 30.93% (which remains approximately the same over the entire selected UHF-ISM band), and the corresponding read range was calculated to be 8.09 m considering a reader $EIRP$ of 4 W, which is also maximum in the band.

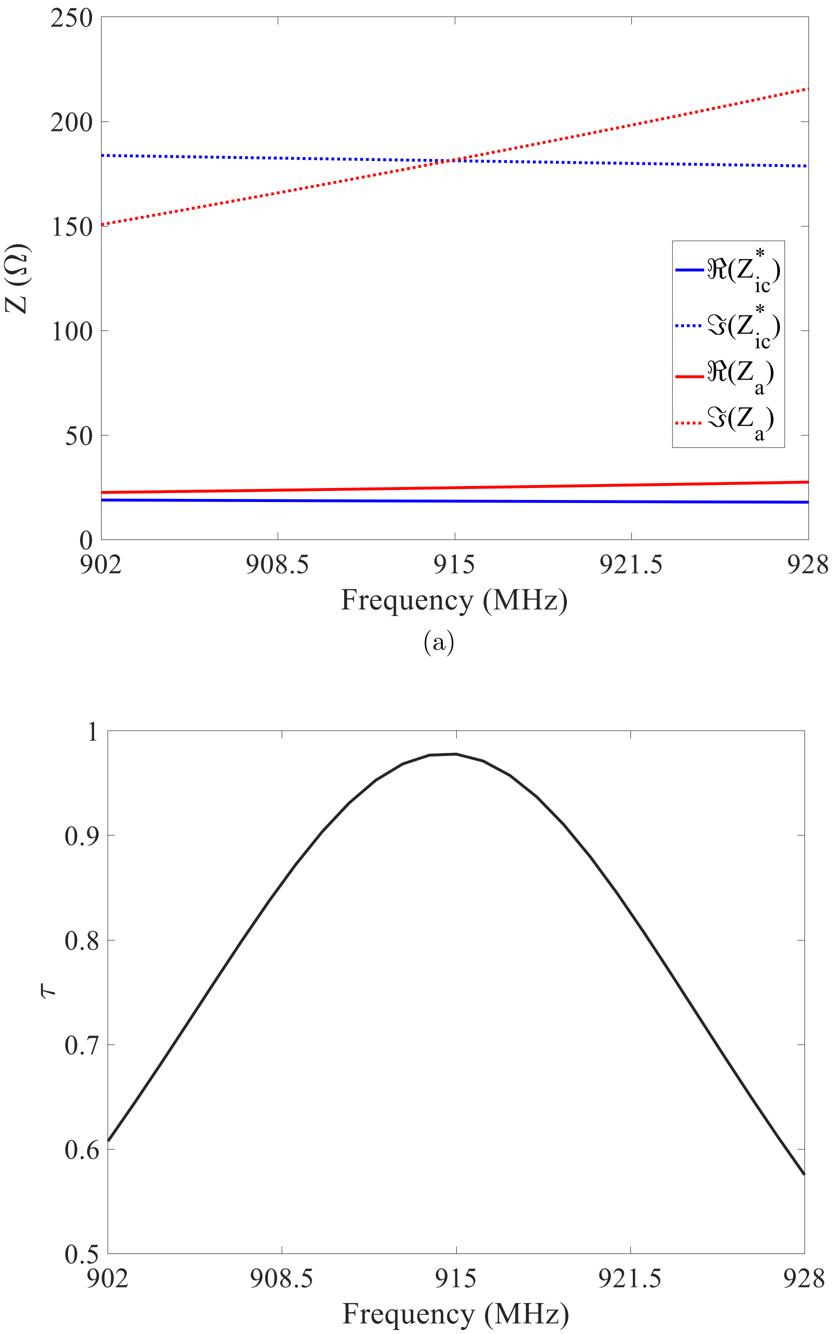

(a)

(b)

Figure 5.6: (a) Comparison between Z_{ic}^* and Z_a, and (b) corresponding an antenna-IC power transfer efficiency τ.

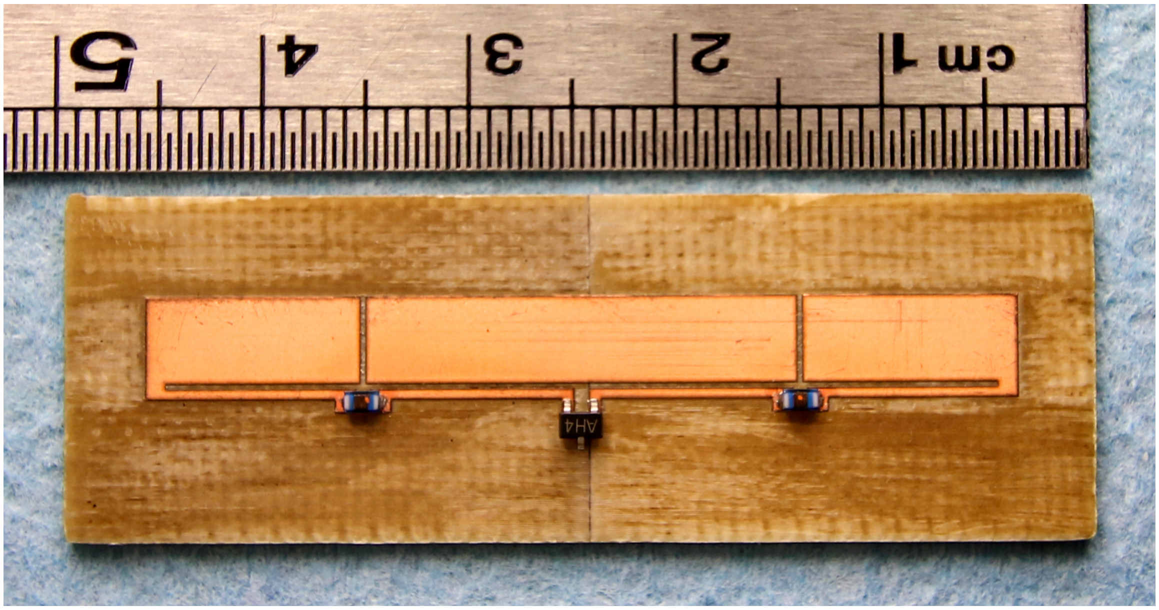

Figure 5.7: Fabricated prototype of the RFID tag antenna.

5.3.3 Fabrication and Measurement

The simulated structure was fabricated using the LPKF ProtoLaser U3 milling machine. The lumped discrete inductors and the IC chip were soldered onto the antenna surface at their respective places. The fabricated prototype is shown in Fig. 5.7.

In order to measure the read range of the tag antenna, a commercially available Right-Handed Circularly Polarized (RHCP) patch antenna (MT-242025/TRH/A by MTI Wireless Edge Ltd.) was used as the front end of the reader. The antenna has an operating bandwidth of 865-956 MHz, and exhibits a gain of 7.5 dBic in the frequency range of 902-928 MHz [163]. The next section of the reader comprised a ThingMagic M6e Embedded RFID reader module, where the input power of the reader antenna could be varied over a range from 5 dBm to 31.5 dBm [164].

The read-range measurement was performed inside the near-field anechoic chamber, but since the maximum available distance inside the chamber between the reader and the tag antennas ($\approx$ 2.5 m) was much smaller compared to the simulated read range reported in Section 5.3.2, it was decided to decrease the $EIRP$ of the reader antenna by reducing its

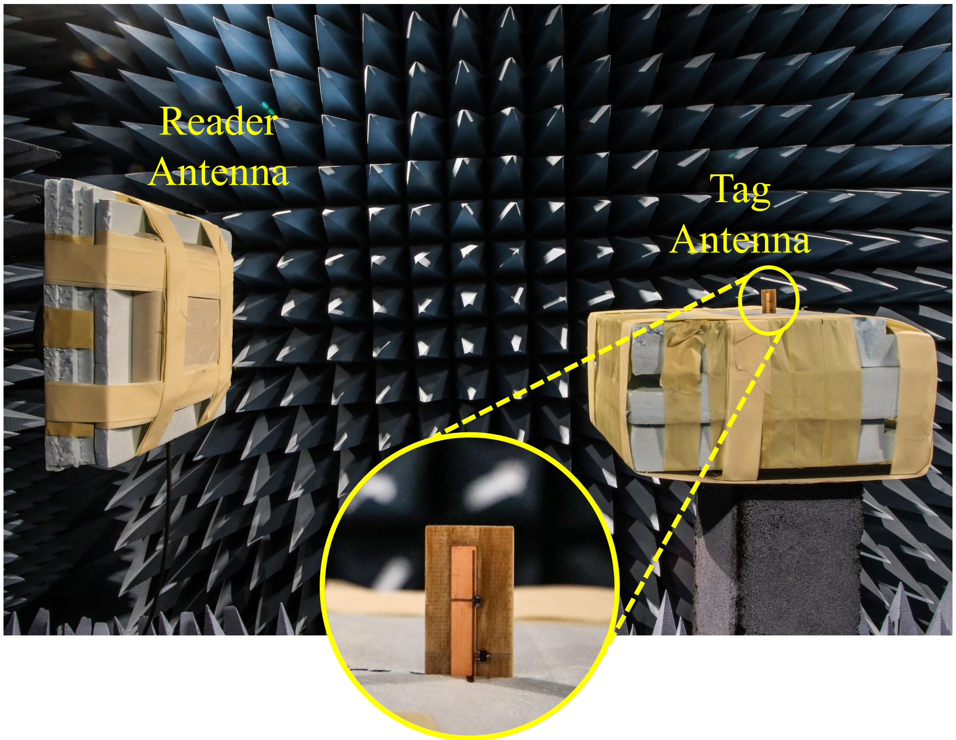

Figure 5.8: Experimental setup for measuring the read range of the RFID tag antenna.

input power in order to bring down the maximum read range within the available distance. The tag antenna was placed in such a way that the reader antenna appears in its broadside direction. The measurement setup is shown in Fig. 5.8.

In order to compare the measured read range with the simulated, the measured data were scaled for $EIRP = 4$ W and a linearly-polarized reader antenna using the following equation, which can be obtained directly from equation 5.2:

$$\frac{d_{tag,scaled}}{d_{tag,meas}} = \sqrt{\frac{4}{\chi_{pol} \cdot EIRP_{meas}}} \tag{5.4}$$

where, $d_{tag,scaled}$ and $d_{tag,meas}$ are the scaled and measured read ranges, respectively. Since the reader and the tag antennas are circularly and linearly polarized, respectively, the value of the polarization efficiency χ_{pol} was set as 0.5. Finally, $EIRP_{meas}$ is the $EIRP$ of the reader antenna with reduced input power P_{in} and can be given as:

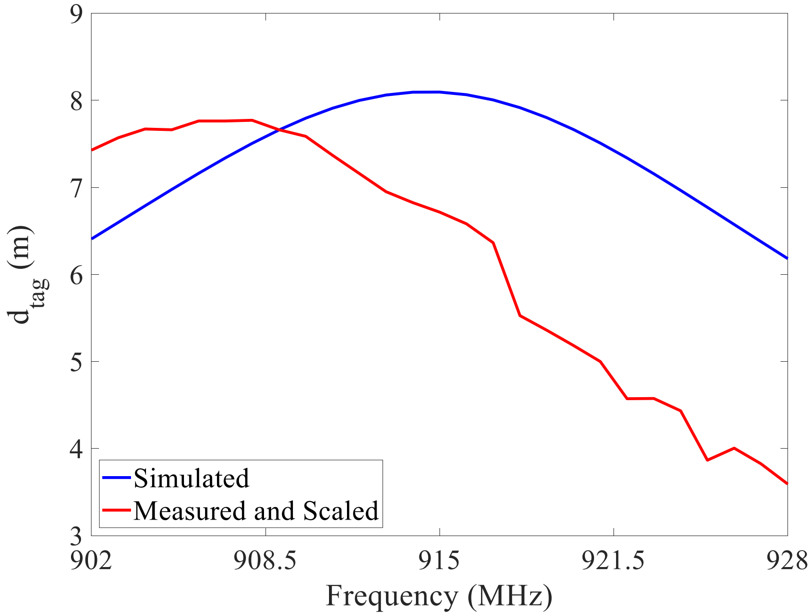

Figure 5.9: Simulated vs. measured and scaled d_{tag}.

$$EIRP_{meas} = G_{reader} \cdot P_{in} \tag{5.5}$$

where, G_{reader} is the gain of the reader antenna. The comparison between the measured and scaled vs. simulated read-range data is shown in Fig. 5.9. It can be seen that the maximum measured read range occurs at 908 MHz, which is still within the 902-928 MHz band, and only 7 MHz shifted from the simulated read range peak. The shift is potentially caused due to the finite tolerances (±5%) of the discrete lumped loading inductors. However, this issue can be easily resolved by replacing the lumped inductors by their printed meandered equivalents. The measured read range value at 908 MHz is 7.77 m, which is also very close to the maximum value of the simulated read range at 915 MHz, i.e., 8.09 m.

The E- and H-plane read-range patterns were also measured for the designed tag antenna at 908 MHz where the tag antenna exhibits maximum read range, and shown in Fig. 5.10. Once again, the measurement was done by reducing the $EIRP$ of the reader antenna with an angular resolution of 10° at each plane, and then the measured data were scaled following the same technique. It can be easily noticed that the E- and H-plane read-range patterns

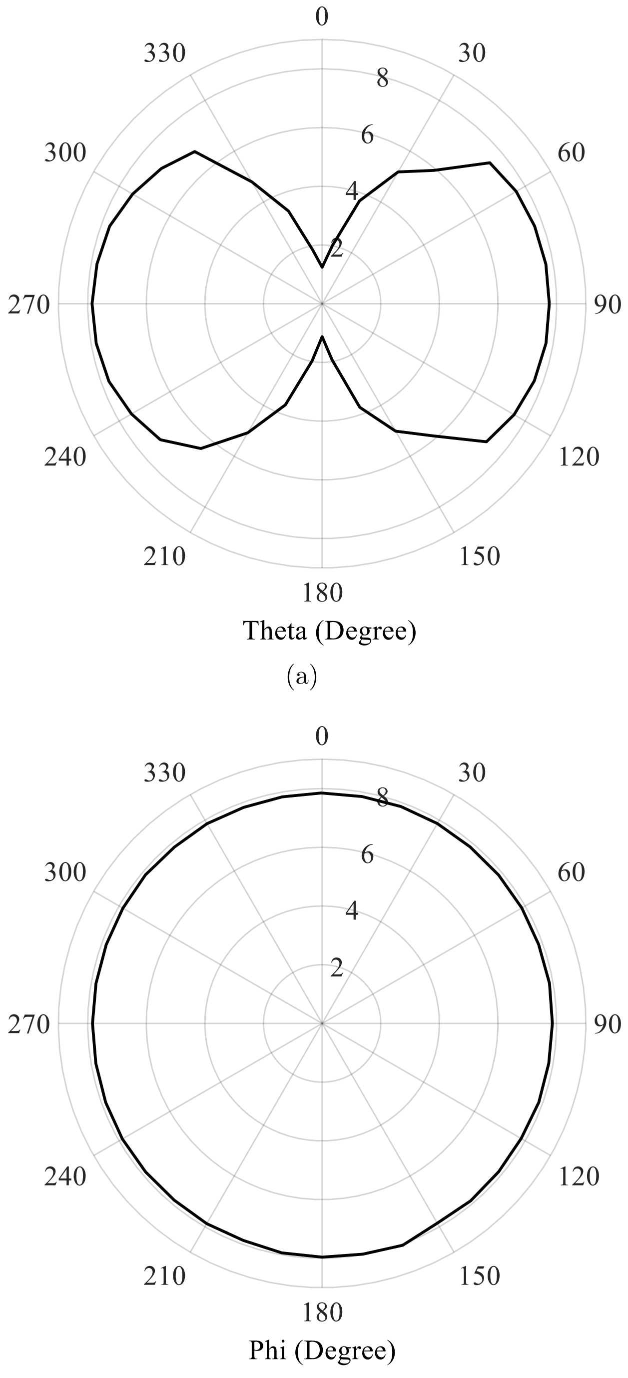

Figure 5.10: Measured read-range patterns at 908 MHz: (a) E-plane, and (b) H-plane (radial scale is in meters).

are exactly identical to the E- and H-plane radiation patterns of a dipole antenna, thus an omnidirectional coverage area of the fabricated RFID tag antenna could be confirmed.

5.4 Summary

In this chapter, it was demonstrated that using the technique proposed in Chapter 4, a folded dipole antenna could be miniaturized and used for various sensing applications that require matching with either real or complex input impedances. For both the cases, the folded dipole antenna were highly miniaturized (75%) and exhibited excellent matching with the target input impedance.

However, it must be noted that some of these sensors often need to operate in close proximity of reflective or high permittivity and lossy mediums, which can alter the performance of these antennas significantly by shifting the operating frequency and/or by reducing the radiation efficiency drastically. Thus, a prior knowledge of the surrounding environment would be helpful while designing these miniaturized sensor antennas.

Chapter 6

Conclusion

6.1 Summary

The work described in this thesis was focused on developing a highly miniaturized, but inherently matched antenna that exhibits dipole-like radiation characteristics, and can be useful in a wide array of narrowband applications. The inherent matching enables these miniaturized antennas to be integrated into various wireless systems without the use of an external matching network, which often increases the overall size and complexity. Additionally, good matching increases the accepted power into an antenna, which implies enhanced radiated power, and hence longer detection range for a sensor antenna. A folded dipole antenna was selected over a conventional dipole antenna for this purpose, mainly because of the presence of an additional resonance ($f_{AR,1}$) before the half-wavelength frequency (f_R) in its input impedance profile and also its impedance-modification property by means of structural changes. A simple series reactive loading scheme has been proposed for this miniaturization technique.

First, the standard theory of folded dipole antenna was extended in order to include the effects of reactive loading. A symmetric loading topology has been applied on an infinitesimally-thin folded dipole antenna for studying the corresponding input impedance trends. It was found that by applying a large series loading inductance and a small series loading capacitance, a new resonance ($f_{R,N}$) could be introduced just before $f_{AR,1}$, which can then be used in conjunction with $f_{AR,1}$ to engineer the corresponding input impedance, such that a good matching can be realized at a desired miniaturized operating frequency. However, it was found that in order to realize closely situated $f_{R,N}$ and $f_{AR,1}$, extreme values would be necessary for the loading reactances while using a symmetric loading topology. Thus, it was decided to introduce asymmetries into the loading scheme, which resulted in a smaller and easily realizable loading reactance values. The conclusions from this study were then applied to a practical example, where a printed folded dipole antenna was miniaturized by 75% and excellent matching was achieved with respect to a real source impedance by properly choosing the loading reactance values and using unequal arm widths as an additional degree of freedom. A unique feed structure was designed to provide a balanced input to the antenna, and its effects on the antenna performance were described in detail. It was shown that any effect on the impedance matching of the miniaturized antenna by the inclusion of practical losses or the feed structure can be easily compensated by slightly adjusting the loading values. Furthermore, the fabricated prototype was validated by performing measurements, which showed excellent agreement with the simulated results. It was also shown that the miniaturized folded dipole antenna exhibits a much better radiation efficiency than its unloaded counterpart and an approximately equal radiation efficiency when compared to an equivalent loaded conventional dipole. However, due to its ability to achieve good impedance matching with respect to any given source impedance, the miniaturized loaded folded dipole antenna will always exhibit a better realized gain than both the other cases, which can be related directly to the radiated power.

In the final chapter, a 75% miniaturized fully printed folded dipole antenna was designed following the same technique, which can be useful for sensor antennas requiring a real input impedance. The UHF-ISM frequency band (902-928 MHz) specified for sensing applications in North America was selected for the design. It was shown that by using a fully printed topology, the bandwidth of operation can be improved slightly at the expense of the radiation efficiency, due to the lower quality factor of the loading reactances. Furthermore, the idea of input-impedance engineering was extended for realizing a RFID tag antenna capable of being inherently and conjugately matched to a complex output source impedance. Once again, the designed structure was validated using measurements, which produced very good agreements with the simulated results.

6.2 Contributions

This section lists the academic contributions made during the course of this doctoral thesis, including journal papers, conference papers, and abstracts.

6.2.1 Journal Papers

[J5] S. Das, H. Saghlatoon, P. Mousavi, and A. K. Iyer, "A highly miniaturized and inherently conjugately matched folded dipole-based RFID tag antenna," *IEEE Access*, vol. 7, pp. 101658-101664, July 2019.

[J4] S. Das, D. J. Sawyer, N. Diamanti, A. P. Annan, and A. K. Iyer, "A strongly miniaturized and inherently matched folded dipole antenna for narrowband applications," under fourth round of review in *IEEE Transactions on Antennas and Propagation*, 2019.

[J3] D. J. Sawyer, S. Das, N. Diamanti, A. P. Annan, and A. K. Iyer, "Choke rings for pattern shaping of a GPR dipole antenna," *IEEE Transactions on Antennas and Propagation*, vol. 66, no. 12, pp. 6781-6790, December 2018.

[J2] L. A. Shaik, C. Saha, S. Arora, S. Das, J. Y. Siddiqui, and A. K. Iyer, "Bandwidth control of cylindrical ring dielectric resonator antennas using metallic cap and sleeve loading," *IET Microwaves, Antennas & Propagation*, vol. 11, no. 12, pp. 1742-1747, October 2017.

[J1] S. Das, H.-L. Nguyen, G. N. Babu, and A. K. Iyer, "Free-space focusing at C-band using a flat fully printed multilayer metamaterial lens," *IEEE Transactions on Antennas and Propagation*, vol. 63, no. 11, pp. 4702-4714, November 2015.

6.2.2 Conference Papers

[C2] S. Das, A. K. Iyer, L. A. Shaik, C. Saha, and J. Y. Siddiqui, "Design of a frequency notched coplanar tapered slot antenna using split ring resonator," 5^{th} *IEEE Applied Electromagnetics Conference (AEMC)*, Guwahati, Assam, India, December 2015.

[C1] S. Das and A. K. Iyer, "Recent results verifying free-space focusing using a fully printed metamaterial lens," 5^{th} *IEEE Applied Electromagnetics Conference (AEMC)*, Guwahati, Assam, India, December 2015.

6.2.3 Abstracts

[A2] S. Das, D. J. Sawyer, N. Diamanti, A. P. Annan, and A. K. Iyer, "Design of strongly miniaturized, inherently matched, and scalable folded dipole antennas," presented in the Special Session: Low-Profile Antennas from Gigahertz to Terahertz at the *USNC-URSI National Radio Science Meeting*, Boulder, CO, USA, January 2019.

[A1] S. Das, A. K. Iyer, A. P. Annan, and N. Diamanti, "Study of reactive loading for the miniaturization of folded dipole antennas," *IEEE International Symposium on Antennas and Propagations and North American Radio Science Meeting*, San Diego, CA, USA, July 2017.

6.3 Future Work

So far in this thesis, it has been demonstrated using both simulations and measurements that a folded dipole antenna can be made to achieve impedance matching for both real and complex input impedances at a desired level of miniaturization, without the need of an external matching network. Potential extensions of this research are discussed below.

6.3.1 Effect of Loading Locations

For all the examples shown in Chapters 4 and 5, the reactive loading elements were placed right in the middle of each half of the antenna. Thus, it is important to study the effect of reactive loading locations on the input impedance and the radiation efficiency of the antenna. Furthermore, an analytical model for the asymmetrically loaded folded dipole antenna as a function of the loading location would be very useful in obtaining more accurate initial guesses without the need for time- and memory-consuming simulations.

6.3.2 Effect of Multiple Arms

For certain applications, using multiple folded/driven arms might become necessary. Therefore, it is also important to study how the input impedance and the radiation efficiency of the antenna varies as a function of the loading reactance values, when the antenna is operated around its first antiresonance along with multiple folded/driven arms.

6.3.3 Other Topologies

A three-dimensional topology can be realized based on the fully printed miniaturized folded dipole antenna reported in Chapter 5, as shown in Fig. 6.1. In this topology, the inductive loading is realized by a helical folded arm, and the loading value can be controlled by varying the radius and/or the number of turns of the helix. The capacitive loading is realized by placing two gaps on the cylindrical driven arm. A further study can be performed

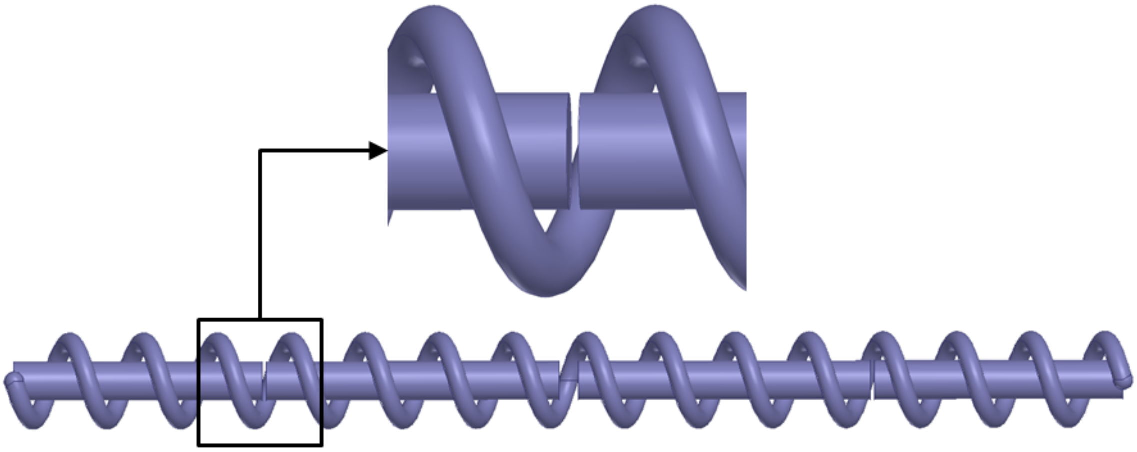

Figure 6.1: Three-dimensional topology for miniaturizing folded dipole antennas.

with this topology in order to realize a higher radiation efficiency of the antenna. It has been shown in [165–167] that if an electrically small antenna occupies most of the space inside the smallest possible sphere that completely encloses the antenna and its currents, then the quality factor of the antenna approaches its theoretical minimum limit, which can be used for improving the bandwidth and the radiation efficiency of the small antenna. Thus, for the 3-D antenna, if the helix radius can be changed with each turn in a way such that the maximum radius occurs at the feed and the minimum radius occurs at the ends, it is possible to lower the quality factor of the antenna. An example of the proposed structure is shown in Fig. 6.2. Furthermore, a bowtie variant can also be studied for achieving a broader bandwidth.

6.3.4 Other Investigations

The sensor antennas described in Chapter 5 should be tested in real-life scenarios, e.g., in proximity with reflective or high permittivity and lossy mediums, which can degrade the performance of the antennas by shifting the operating frequency and/or by deteriorating the radiation efficiency significantly. Thus structural changes might be necessary along with optimizing loading reactance values in order to achieve the required system specifications. Furthermore, a conformal prototype of the miniaturized fully printed folded dipole antenna

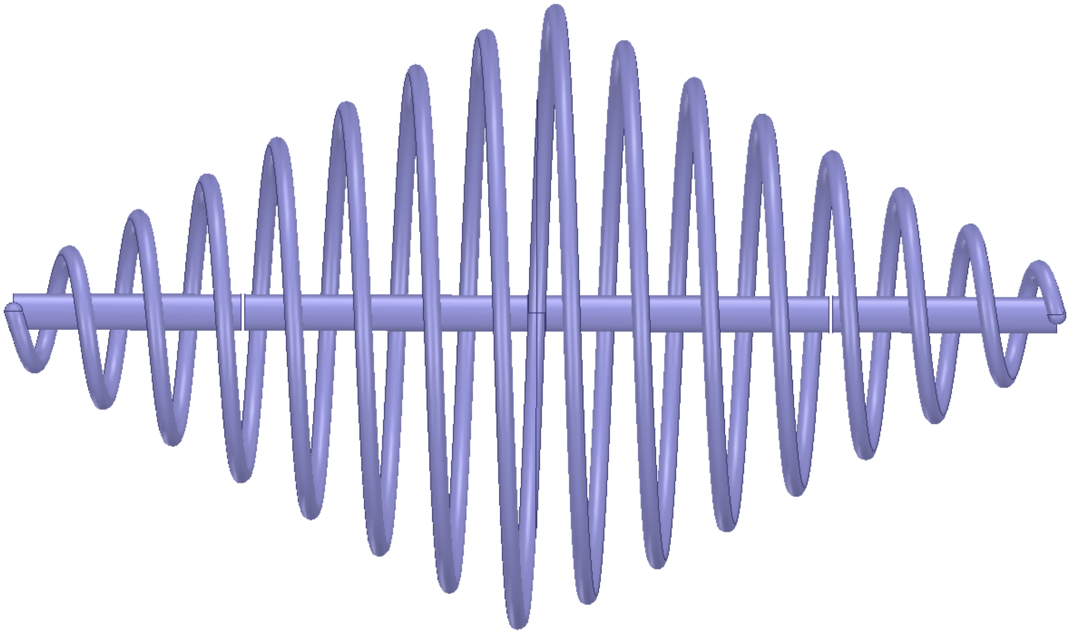

Figure 6.2: Three-dimensional topology with increasing helix radius towards the feed.

can be realized on a flexible substrate.

The operating point of the miniaturized antennas depends on the permittivity of the dielectric substrate used, and hence the effective permittivity of the medium. Thus, if the antenna is brought closer to another dielectric substrate, the operating frequency will shift due to the change in the effective permittivity. Thus, these electrically small antennas can also be used in dielectric sensing applications.

Finally, since a loop antenna has a similar input impedance profile as a folded dipole antenna, this technique can also be used to realize electrically small loop antennas that are matched inherently to a given source impedance.

Bibliography

[1] J. Ramsay, "Highlights of antenna history," *IEEE Antennas and Propagation Society Newsletter*, vol. 23, no. 6, pp. 7–20, December 1981.

[2] C. A. Balanis, *Antenna Theory: Analysis and Design.* Hoboken, NJ, USA: John Wiley & Sons, Inc., 2005.

[3] K. Fujimoto and J. R. James, *Mobile Antenna Systems Handbook.* Norwood, MA, USA: Artech House, 1994.

[4] M. A. Jensen and Y. Rahmat-Samii, "Performance analysis of antennas for hand-held transceivers using FDTD," *IEEE Transactions on Antennas and Propagation*, vol. 42, no. 8, pp. 1106–1113, August 1994.

[5] C. A. Balanis, *Modern Antenna Handbook.* Hoboken, NJ, USA: John Wiley & Sons, Inc., 2008.

[6] T. A. Milligan, *Modern Antenna Design.* Hoboken, NJ, USA: John Wiley & Sons, Inc., 2005.

[7] M. A. Bulgerin and A. B. Walters, *NOLC Report*, vol. 154, pp. 67–83, 1954.

[8] C. Harrison, "Monopole with inductive loading," *IEEE Transactions on Antennas and Propagation*, vol. 11, no. 4, pp. 394–400, July 1963.

[9] R. Hansen, "Efficiency and matching tradeoffs for inductively loaded short antennas," *IEEE Transactions on Communications*, vol. 23, no. 4, pp. 430–435, April 1975.

[10] R. C. Hansen, “Optimum inductive loading of short whip antennas,” *IEEE Transactions on Vehicular Technology*, vol. 24, no. 2, pp. 21–29, May 1975.

[11] K. Fujimoto, “A loaded antenna system applied to VHF portable communication equipment,” *IEEE Transactions on Vehicular Technology*, vol. 17, no. 1, pp. 6–12, October 1968.

[12] H. Brueckmann, “Theory and performance of vehicular center-fed whip antenna,” *IRE Transactions on Vehicular Communications*, vol. 9, no. 3, pp. 10–20, December 1960.

[13] W. Czerwinski, “On optimizing efficiency and bandwidth of inductively loaded antennas,” *IEEE Transactions on Antennas and Propagation*, vol. 13, no. 5, pp. 811–812, September 1965.

[14] W. P. Czerwinski, “On a foreshortened center-fed whip antenna,” *IEEE Transactions on Vehicular Communications*, vol. 15, no. 2, pp. 33–40, October 1966.

[15] J. Rashed and C.-T. Tai, “A new class of resonant antennas,” *IEEE Transactions on Antennas and Propagation*, vol. 39, no. 9, pp. 1428–1430, September 1991.

[16] M. Ali and S. S. Stuchly, “A meander-line bow-tie antenna,” in *IEEE Antennas and Propagation Society International Symposium. 1996 Digest*, vol. 3, July 1996, pp. 1566–1569 vol.3.

[17] T. J. Warnagiris and T. J. Minardo, “Performance of a meandered line as an electrically small transmitting antenna,” *IEEE Transactions on Antennas and Propagation*, vol. 46, no. 12, pp. 1797–1801, December 1998.

[18] B. Al-Khateeb, V. Rabinovich, B. Oakley, and N. Alexandrov, “Compact planar antennas for short-range wireless automotive communication,” *IEEE Transactions on Vehicular Technology*, vol. 55, no. 4, pp. 1425–1435, July 2006.

[19] O. O. Olaode, W. D. Palmer, and W. T. Joines, “Effects of meandering on dipole antenna resonant frequency,” *IEEE Antennas and Wireless Propagation Letters*, vol. 11, pp. 122–125, 2012.

[20] H. Nakano, H. Tagami, A. Yoshizawa, and J. Yamauchi, “Shortening ratios of modified dipole antennas,” *IEEE Transactions on Antennas and Propagation*, vol. 32, no. 4, pp. 385–386, April 1984.

[21] M. Ali, S. Stuchly, and K. Caputa, “Characteristics of bent wire antennas,” *Journal of Electromagnetic Waves and Applications*, vol. 9, no. 9, pp. 1149–1162, 1995.

[22] A. A. Lestari, D. Yulian, A. B. Suksmono, E. Bharata, A. C. Yarovoy, and L. P. Ligthart, “Rolled dipole antenna for low-resolution GPR,” *Progress in Electromagnetics Research*, vol. 3, no. 7, pp. 1107–1110, 2007.

[23] J. H. Bryant, “The first century of microwaves-1886 to 1986,” *IEEE Transactions on Microwave Theory and Techniques*, vol. 36, no. 5, pp. 830–858, May 1988.

[24] S. A. Schelkunoff and H. T. Friis, *Antennas: Theory and Practice.* NY, USA: John Wiley & Sons, Inc., 1952.

[25] K. Fujimoto and H. Morishita, *Modern Small Antennas.* NY, USA: Cambridge University Press, 2013.

[26] T. L. Simpson, “The disk loaded monopole antenna,” *IEEE Transactions on Antennas and Propagation*, vol. 52, no. 2, pp. 542–550, February 2004.

[27] Z. Shen and J. Wang, “Top-hat monopole antenna for conical-beam radiation,” *IEEE Antennas and Wireless Propagation Letters*, vol. 10, pp. 396–398, 2011.

[28] C. E. Smith and E. M. Johnson, “Performance of short antennas,” *Proceedings of the IRE*, vol. 35, no. 10, pp. 1026–1038, October 1947.

[29] A. Gangi, S. Sensiper, and G. Dunn, "The characteristics of electrically short, umbrella top-loaded antennas," *IEEE Transactions on Antennas and Propagation*, vol. 13, no. 6, pp. 864–871, November 1965.

[30] S. R. Best and D. L. Hanna, "A performance comparison of fundamental small-antenna designs," *IEEE Antennas and Propagation Magazine*, vol. 52, no. 1, pp. 47–70, February 2010.

[31] J. Hao, "Spiral coil loaded short wire antenna," in *2008 IEEE Radio and Wireless Symposium*, January 2008, pp. 319–322.

[32] K. Fujimoto, A. Henderson, K. Hirasawa, and J. R. James, *Small Antennas.* Letchworth, UK: Research Studies Press, 1987.

[33] A. D. Wunsch and S.-P. Hu, "A closed-form expression for the driving-point impedance of the small inverted L antenna," *IEEE Transactions on Antennas and Propagation*, vol. 44, no. 2, pp. 236–242, February 1996.

[34] G. V. Eleftheriades and K. G. Balmain, *Negative-Refraction Metamaterials: Fundamental Principles and Applications.* Hoboken, NJ, USA: John Wiley & Sons, Inc., 2005.

[35] C. Caloz and T. Itoh, *Electromagnetic Metamaterials: Transmission Line Theory and Microwave Applications.* Hoboken, NJ, USA: John Wiley & Sons, Inc., 2006.

[36] H. Iizuka and P. S. Hall, "Left-handed dipole antennas and their implementations," *IEEE Transactions on Antennas and Propagation*, vol. 55, no. 5, pp. 1246–1253, May 2007.

[37] C. Caloz, T. Itoh, and A. Rennings, "CRLH metamaterial leaky-wave and resonant antennas," *IEEE Antennas and Propagation Magazine*, vol. 50, no. 5, pp. 25–39, October 2008.

[38] C. Caloz and A. Rennings, "Overview of resonant metamaterial antennas," in *The 3rd European Conference on Antennas and Propagation (EuCAP)*, March 2009, pp. 615–619.

[39] M. R. Booket, M. Kamyab, A. Jafargholi, and S. M. Mousavi, "Analytical modeling of the printed dipole antenna loaded with CRLH structures," *Progress in Electromagnetic Research B*, vol. 20, pp. 167–186, 2010.

[40] M. A. Antoniades and G. V. Eleftheriades, "Multiband compact printed dipole antennas using NRI-TL metamaterial loading," *IEEE Transactions on Antennas and Propagation*, vol. 60, no. 12, pp. 5613–5626, December 2012.

[41] R. W. Ziolkowski and A. Erentok, "Metamaterial-based efficient electrically small antennas," *IEEE Transactions on Antennas and Propagation*, vol. 54, no. 7, pp. 2113–2130, July 2006.

[42] A. Erentok and R. W. Ziolkowski, "Metamaterial-inspired efficient electrically small antennas," *IEEE Transactions on Antennas and Propagation*, vol. 56, no. 3, pp. 691–707, March 2008.

[43] K. B. Alici and E. Ozbay, "Radiation properties of a split ring resonator and monopole composite," *physica status solidi (b)*, vol. 244, no. 4, pp. 1192–1196, 2007.

[44] M. R. Booket, A. Jafargholi, Z. Atlasbaf, and M. Kamyab, "Miniaturized dual-band dipole antenna loaded with metamaterial based structure," in *2011 19th Iranian Conference on Electrical Engineering*, May 2011, pp. 1–4.

[45] R. King, C. Harrison, and D. Denton, "Transmission-line missile antennas," *IRE Transactions on Antennas and Propagation*, vol. 8, no. 1, pp. 88–90, January 1960.

[46] R. A. Bhatti, Y. Im, and S. Park, “Compact PIFA for mobile terminals supporting multiple cellular and non-cellular standards,” *IEEE Transactions on Antennas and Propagation*, vol. 57, no. 9, pp. 2534–2540, September 2009.

[47] D. M. Elsheakh and E. A. Abdallah, “Compact multiband multifolded-slot antenna loaded with printed-IFA,” *IEEE Antennas and Wireless Propagation Letters*, vol. 11, pp. 1478–1481, 2012.

[48] D. M. Elsheakh and A. M. E. Safwat, “Slow-wave quad-band printed inverted-F antenna (IFA),” *IEEE Transactions on Antennas and Propagation*, vol. 62, no. 8, pp. 4396–4401, August 2014.

[49] H.-T. Chen, K.-L. Wong, and T.-W. Chiou, “PIFA with a meandered and folded patch for the dual-band mobile phone application,” *IEEE Transactions on Antennas and Propagation*, vol. 51, no. 9, pp. 2468–2471, September 2003.

[50] A. Holub and M. Polivka, “Vertically meander-folded, shorted-patch antennas,” *Microwave and Optical Technology Letters*, vol. 51, no. 12, pp. 2938–2942, 2009.

[51] O. Losito, V. Dimiccoli, and D. Barletta, “Meander-line inverted F antenna designed using a transmission line model,” in *The 8th European Conference on Antennas and Propagation (EuCAP)*, April 2014, pp. 1370–1373.

[52] C. R. Rowell and R. D. Murch, “A capacitively loaded PIFA for compact mobile telephone handsets,” *IEEE Transactions on Antennas and Propagation*, vol. 45, no. 5, pp. 837–842, May 1997.

[53] L. Loizou, J. Buckley, M. Belcastro, J. Barton, B. O’Flynn, and C. O’Mathuna, “Miniaturized inverted-F antenna with capacitive loading,” in *The 7th European Conference on Antennas and Propagation (EuCAP)*, April 2013, pp. 3213–3216.

[54] A. R. Raslan, A. A. Ibrahim, and A. M. E. Safwat, “Resonant-type antennas loaded with CRLH unit cell,” *IEEE Antennas and Wireless Propagation Letters*, vol. 12, pp. 23–26, 2013.

[55] A. Soliman, D. Elsheakh, E. Abdallah, and H. El-Hennawy, “Multiband printed metamaterial inverted-F antenna (IFA) for USB applications,” *IEEE Antennas and Wireless Propagation Letters*, vol. 14, pp. 297–300, 2015.

[56] D. M. Grimes, “Miniaturized resonant antenna using ferrites,” *Journal of Applied Physics*, vol. 29, no. 3, pp. 401–402, March 1958.

[57] C. Polk, “Resonance and supergain effects in small ferromagnetically or dielectrically loaded biconical antennas,” *IRE Transactions on Antennas and Propagation*, vol. 7, no. 5, pp. 414–423, December 1959.

[58] J. Galejs, “Dielectric loading of electric dipole antennas,” *Journal of research of the National Bureau of Standards-D, Radio propagation*, vol. 66D, no. 5, pp. 557–562, September-October 1962.

[59] J. R. James and A. Henderson, “Electrically short monopole antennas with dielectric or ferrite coatings,” *Proceedings of the Institution of Electrical Engineers*, vol. 125, no. 9, pp. 793–803, September 1978.

[60] T. F. Kennedy, S. A. Long, and J. T. Williams, “Modification and control of currents on monopole antennas using magnetic bead loading,” *IEEE Antennas and Wireless Propagation Letters*, vol. 2, pp. 208–211, 2003.

[61] R. C. Hansen and R. E. Collin, *Small Antenna Handbook.* Hoboken, NJ, USA: John Wiley & Sons, Inc., 2011.

[62] J. L. Volakis, *Antenna Engineering Handbook.* NY, USA: The McGraw-Hill Companies, 2007.

[63] P. A. Ryan, “Low profile electric field sensor,” U.S. patent 4 383 260A, May 10, 1983.

[64] G. Skahill, R. M. Rudish, and J. A. Pierro, “Apparatus and method for broadband matching of electrically small antennas,” U.S. patent 6 121 940A, September 19, 2000.

[65] S. E. Sussman-Fort, “Matching network design using non-foster impedances,” *International Journal of RF and Microwave Computer-Aided Engineering*, vol. 16, no. 2, pp. 135–142, 2006.

[66] R. Guertler, “Impedance transformation in folded dipoles,” *Proceedings of the IRE*, vol. 38, no. 9, pp. 1042–1047, September 1950.

[67] E. Seeley, “Inductively loaded folded antenna,” U.S. patent 3 103 011, September 3, 1963.

[68] S. R. Best, “The performance properties of electrically small resonant multiple-arm folded wire antennas,” *IEEE Antennas and Propagation Magazine*, vol. 47, no. 4, pp. 13–27, August 2005.

[69] M. Takiguchi and Y. Yamada, “Radiation and ohmic resistances in very small meander line antennas of less than 0.1 wavelength,” *Electronics and Communications in Japan (Part I: Communications)*, vol. 88, no. 8, pp. 1–11, 2005.

[70] Y. Zhang and H. Y. D. Yang, “Bandwidth-enhanced electrically small printed folded dipoles,” *IEEE Antennas and Wireless Propagation Letters*, vol. 9, pp. 236–239, 2010.

[71] E. W. Seeley, “An experimental study of the disk-loaded folded monopole,” *IRE Transactions on Antennas and Propagation*, vol. 4, no. 1, pp. 27–28, January 1956.

[72] E. Seeley, J. Burns, and K. Welton, “Cap-loaded folded antenna,” in *1958 IRE International Convention Record*, vol. 6, March 1958, pp. 133–138.

[73] T. Kokkinos and A. P. Feresidis, "Low-profile folded monopoles with embedded planar metamaterial phase-shifting lines," *IEEE Transactions on Antennas and Propagation*, vol. 57, no. 10, pp. 2997–3008, October 2009.

[74] M. A. Antoniades and G. V. Eleftheriades, "A folded-monopole model for electrically small NRI-TL metamaterial antennas," *IEEE Antennas and Wireless Propagation Letters*, vol. 7, pp. 425–428, 2008.

[75] J. Oh, J. Choi, F. T. Dagefu, and K. Sarabandi, "Extremely small two-element monopole antenna for HF band applications," *IEEE Transactions on Antennas and Propagation*, vol. 61, no. 6, pp. 2991–2999, June 2013.

[76] J. Choi, F. T. Dagefu, B. M. Sadler, and K. Sarabandi, "Electrically small folded dipole antenna for HF and low-VHF bands," *IEEE Antennas and Wireless Propagation Letters*, vol. 15, pp. 718–721, 2016.

[77] M. Polivka and D. Vrba, "Electrically small spiral transmission line-connected triple-arm folded monopole antenna," in *The 6th European Conference on Antennas and Propagation (EuCAP)*, March 2012, pp. 2488–2490.

[78] S. H. Kim and J. H. Jang, "Compact folded monopole antenna with LC-loadings," in *2010 International Workshop on Antenna Technology (iWAT)*, March 2010, pp. 1–4.

[79] R. King, "The rectangular loop antenna as a dipole," *IRE Transactions on Antennas and Propagation*, vol. 7, no. 1, pp. 53–61, January 1959.

[80] G. Thiele, E. Ekelman, and L. Henderson, "On the accuracy of the transmission line model of the folded dipole," *IEEE Transactions on Antennas and Propagation*, vol. 28, no. 5, pp. 700–703, September 1980.

[81] R. W. P. King and C. W. Harrison, *Antennas and Waves: A Modern Approach.* Cambridge, MA, USA: The MIT Press, 1969.

[82] R. N. Simons, *Coplanar Waveguide Circuits, Components, and Systems.* Hoboken, NJ, USA: John Wiley & Sons, Inc., 2001.

[83] E. Newman, "The equivalent separation(s) for the self-impedance of thin strips," *IEEE Transactions on Antennas and Propagation*, vol. 35, no. 1, pp. 110–113, January 1987.

[84] R. S. Elliott, *Antenna Theory and Design.* NJ, USA: Prentice Hall, Inc., 1981.

[85] Y. Qian and T. Itoh, "A broadband uniplanar microstrip-to-CPS transition," in *1997 Asia-Pacific Microwave Conference*, December 1997, pp. 609–612.

[86] Y.-H. Suh and K. Chang, "A wideband coplanar stripline to microstrip transition," *IEEE Microwave and Wireless Components Letters*, vol. 11, no. 1, pp. 28–29, January 2001.

[87] T. Chiu and Y.-S. Shen, "A broadband transition between microstrip and coplanar stripline," *IEEE Microwave and Wireless Components Letters*, vol. 13, no. 2, pp. 66–68, February 2003.

[88] W.-H. Tu and K. Chang, "Wide-band microstrip-to-coplanar stripline/slotline transitions," *IEEE Transactions on Microwave Theory and Techniques*, vol. 54, no. 3, pp. 1084–1089, March 2006.

[89] Y. Kim, D. Woo, K. W. Kim, and Y. Cho, "A new ultra-wideband microstrip-to-CPS transition," in *2007 IEEE/MTT-S International Microwave Symposium*, June 2007, pp. 1563–1566.

[90] Mini-Circuits, Inc., NY, USA. [Online]. Available: https://www.minicircuits.com/WebStore/dashboard.html?model=TC4-25%2B.

[91] Coilcraft, Inc., IL, USA. [Online]. Available: https://www.coilcraft.com/pdfs/spice_0603hp.pdf.

[92] NSI-MI Technologies, CA, USA. [Online]. Available: https://www.nsi-mi.com/.

[93] M. Chen, J. Wan, and F. Li, "Machine-to-machine communications: Architectures, standards and applications," *KSII Transactions on Internet and Information Systems*, vol. 6, no. 2, pp. 480–497, February 2012.

[94] D. S. Watson, M. A. Piette, O. Sezgen, and N. Motegi, "Machine to machine (M2M) technology in demand responsive commercial buildings," in *2004 ACEEE Summer Study on Energy Efficiency in Buildings*, August 2004.

[95] K. Y. Yazdandoost and R. Miura, "Compact printed multiband antenna for M2M applications," in *The 8th European Conference on Antennas and Propagation (EuCAP)*, April 2014, pp. 2521–2524.

[96] Y. Suzuki and M. Sumi, "Multiband film antenna comprising offset fed dipole elements using inkjet printer for M2M applications," in *2016 International Workshop on Antenna Technology (iWAT)*, February 2016, pp. 51–54.

[97] M. Sumi, K. Cho, and Y. Suzuki, "Printed antenna comprising symmetrically arranged trapezoidal elements, rectangle strip elements, and folded strip elements for GSM/W-CDMA/LTE M2M applications," in *2015 International Workshop on Antenna Technology (iWAT)*, March 2015, pp. 257–259.

[98] C. Hu, W. Chen, J. W. Huang, and J. Chiu, "Design of a multiband coupled-meander-line monopole antenna for M2M applications," in *2010 International Conference on Applications of Electromagnetism and Student Innovation Competition Awards (AEM2C)*, August 2010, pp. 264–268.

[99] A. Loutridis, K. Yang, M. John, and M. J. Ammann, "Dual band printed antenna for M2M applications in ISM and GSM bands," in *2015 Loughborough Antennas Propagation Conference (LAPC)*, November 2015, pp. 1–4.

[100] A. Loutridis, M. John, and M. Ammann, “Printed folded meander line dual-band monopole for TV white space and GSM,” in *The 8th European Conference on Antennas and Propagation (EuCAP)*, April 2014, pp. 2848–2852.

[101] M. John and M. J. Ammann, “A compact shorted printed monopole antenna for TV white space trials,” in *The 7th European Conference on Antennas and Propagation (EuCAP)*, April 2013, pp. 3713–3715.

[102] Q. Zhang, Y. Gao, and C. Parini, “Miniaturized UHF antenna using a magneto-dielectric superstrate for M2M communications,” in *2015 IEEE International Symposium on Antennas and Propagation USNC/URSI National Radio Science Meeting*, July 2015, pp. 1240–1241.

[103] R. Ma, Y. Gao, Y. Wang, and C. Parini, “Circular co-planar inverted-F antenna for UHF machine-to-machine communications,” in *2015 IEEE International Symposium on Antennas and Propagation USNC/URSI National Radio Science Meeting*, July 2015, pp. 1418–1419.

[104] L. Lizzi and F. Ferrero, “Use of ultra-narrow band miniature antennas for internet-of-things applications,” *Electronics Letters*, vol. 51, no. 24, pp. 1964–1966, 2015.

[105] L. Lizzi, F. Ferrero, P. Monin, C. Danchesi, and S. Boudaud, “Design of miniature antennas for IoT applications,” in *2016 IEEE Sixth International Conference on Communications and Electronics (ICCE)*, July 2016, pp. 234–237.

[106] L. Lizzi, F. Ferrero, C. Danchesi, and S. Boudaud, “Design of antennas enabling miniature and energy efficient wireless IoT devices for smart cities,” in *2016 IEEE International Smart Cities Conference (ISC2)*, September 2016, pp. 1–5.

[107] A. Loutrids, M. John, and M. J. Ammann, “Dual band LTE planar inverted-F antenna for M2M applications,” *Microwave and Optical Technology Letters*, vol. 55, no. 12, pp. 2925–2929, 2013.

[108] C. Reig and E. Avila-Navarro, “Printed antennas for sensor applications: A review,” *IEEE Sensors Journal*, vol. 14, no. 8, pp. 2406–2418, August 2014.

[109] R. Salvado, C. Loss, R. Gonsalves, and P. Pinho, “Textile materials for the design of wearable antennas: A survey,” *Sensors*, vol. 12, no. 11, pp. 15 841–15 857, November 2012.

[110] P. Soontornpipit, C. M. Furse, and Y. C. Chung, “Design of implantable microstrip antenna for communication with medical implants,” *IEEE Transactions on Microwave Theory and Techniques*, vol. 52, no. 8, pp. 1944–1951, August 2004.

[111] J. Kim and Y. Rahmat-Samii, “Implanted antennas inside a human body: simulations, designs, and characterizations,” *IEEE Transactions on Microwave Theory and Techniques*, vol. 52, no. 8, pp. 1934–1943, August 2004.

[112] T. Koo, Y. Hong, G. Park, K. Shin, and J. Yook, “Extremely low-profile antenna for attachable bio-sensors,” *IEEE Transactions on Antennas and Propagation*, vol. 63, no. 4, pp. 1537–1545, April 2015.

[113] A. Kiourti and K. S. Nikita, “A review of implantable patch antennas for biomedical telemetry: Challenges and solutions [Wireless Corner],” *IEEE Antennas and Propagation Magazine*, vol. 54, no. 3, pp. 210–228, June 2012.

[114] G. A. Conway and W. G. Scanlon, “Antennas for over-body-surface communication at 2.45 GHz,” *IEEE Transactions on Antennas and Propagation*, vol. 57, no. 4, pp. 844–855, April 2009.

[115] I. Locher, M. Klemm, T. Kirstein, and G. Troster, “Design and characterization of purely textile patch antennas,” *IEEE Transactions on Advanced Packaging*, vol. 29, no. 4, pp. 777–788, November 2006.

[116] T. F. Kennedy, P. W. Fink, A. W. Chu, N. J. Champagne, G. Y. Lin, and M. A. Khayat, "Body-worn e-textile antennas: The good, the low-mass, and the conformal," *IEEE Transactions on Antennas and Propagation*, vol. 57, no. 4, pp. 910–918, April 2009.

[117] F. Merli, L. Bolomey, E. Meurville, and A. K. Skrivervik, "Implanted antenna for biomedical applications," in *2008 IEEE Antennas and Propagation Society International Symposium*, July 2008, pp. 1–4.

[118] U. Kim and J. Choi, "An implantable antenna for wireless body area network application," *Journal of Electromagnetic Engineering and Science*, vol. 10, no. 4, pp. 206–211, December 2010.

[119] S. Kim, K. Kwon, and J. Choi, "Design of a miniaturized high-isolation diversity antenna for wearable WBAN applications," *Journal of Electromagnetic Engineering and Science*, vol. 13, no. 1, pp. 28–33, March 2013.

[120] Q. Bai and R. Langley, "Crumpling of PIFA textile antenna," *IEEE Transactions on Antennas and Propagation*, vol. 60, no. 1, pp. 63–70, January 2012.

[121] M. Hirvonen, C. Bohme, D. Severac, and M. Maman, "On-body propagation performance with textile antennas at 867 MHz," *IEEE Transactions on Antennas and Propagation*, vol. 61, no. 4, pp. 2195–2199, April 2013.

[122] N. Cho, T. Roh, J. Bae, and H.-J. Yoo, "A planar MICS band antenna combined with a body channel communication electrode for body sensor network," *IEEE Transactions on Microwave Theory and Techniques*, vol. 57, no. 10, pp. 2515–2522, October 2009.

[123] L. Zhang, Z. Wang, and J. L. Volakis, "Textile antennas and sensors for body-worn applications," *IEEE Antennas and Wireless Propagation Letters*, vol. 11, pp. 1690–1693, 2012.

[124] S.-D. Jang and J. Kim, “Passive wireless structural health monitoring sensor made with a flexible planar dipole antenna,” *Smart Materials and Structures*, vol. 21, no. 2, p. 027001, January 2012.

[125] Basari, D. Zakaria, F. Y. Zulkifli, and E. T. Rahardjo, “Implanted helical dipole antenna for UHF band applications,” in *2012 International Symposium on Antennas and Propagation (ISAP)*, October 2012, pp. 1256–1259.

[126] A. M. Chrysler, K. L. Hall, and C. M. Furse, “A comparison of solid, mesh, and segmented strip dipoles in a subdermal environment,” *IEEE Journal of Electromagnetics, RF and Microwaves in Medicine and Biology*, vol. 2, no. 4, pp. 218–225, December 2018.

[127] H. Lin, M. Takahashi, K. Saito, and K. Ito, “Performance of implantable folded dipole antenna for in-body wireless communication,” *IEEE Transactions on Antennas and Propagation*, vol. 61, no. 3, pp. 1363–1370, March 2013.

[128] S. Bakogianni and S. Koulouridis, “Design of a novel compact printed folded dipole antenna for biomedical applications,” in *The 8th European Conference on Antennas and Propagation (EuCAP)*, April 2014, pp. 3178–3182.

[129] H. Mizuno, K. Ito, M. Takahashi, and K. Saito, “A helical folded dipole antenna for implantable communication devices,” in *2010 IEEE Antennas and Propagation Society International Symposium*, July 2010, pp. 1–4.

[130] G. Marrocco, “The art of UHF RFID antenna design: Impedance-matching and size-reduction techniques,” *IEEE Antennas and Propagation Magazine*, vol. 50, no. 1, pp. 66–79, February 2008.

[131] A. Kiourti, “RFID antennas for body-area applications: From wearables to implants,” *IEEE Antennas and Propagation Magazine*, vol. 60, no. 5, pp. 14–25, October 2018.

[132] S. Rao, N. Llombart, E. Moradi, K. Koski, T. Bjorninen, L. Sydanheimo, J. M. Rabaey, J. M. Carmena, Y. Rahmat-Samii, and L. Ukkonen, "Miniature implantable and wearable on-body antennas: Towards the new era of wireless body-centric systems [Antenna applications corner]," *IEEE Antennas and Propagation Magazine*, vol. 56, no. 1, pp. 271–291, February 2014.

[133] H. Stockman, "Communication by means of reflected power," *Proceedings of the IRE*, vol. 36, no. 10, pp. 1196–1204, October 1948.

[134] J. Landt, "The history of RFID," *IEEE Potentials*, vol. 24, no. 4, pp. 8–11, October 2005.

[135] V. Chawla and D. S. Ha, "An overview of passive RFID," *IEEE Communications Magazine*, vol. 45, no. 9, pp. 11–17, September 2007.

[136] G. Marrocco, A. Fonte, and F. Bardati, "Evolutionary design of miniaturized meander-line antennas for RFID applications," in *IEEE Antennas and Propagation Society International Symposium (IEEE Cat. No.02CH37313)*, vol. 2, June 2002, pp. 362–365.

[137] G. Marrocco, "Gain-optimized self-resonant meander line antennas for RFID applications," *IEEE Antennas and Wireless Propagation Letters*, vol. 2, pp. 302–305, 2003.

[138] K. V. S. Rao, P. V. Nikitin, and S. F. Lam, "Antenna design for UHF RFID tags: A review and a practical application," *IEEE Transactions on Antennas and Propagation*, vol. 53, no. 12, pp. 3870–3876, December 2005.

[139] W. Choi, H. W. Son, C. Shin, J.-H. Bae, and G. Choi, "RFID tag antenna with a meandered dipole and inductively coupled feed," in *2006 IEEE Antennas and Propagation Society International Symposium*, July 2006, pp. 619–622.

[140] J. Mathew, M. Abraham, C. Aanandan, and T. Mathew, “A broadband miniaturized UHF RFID dipole tag antenna with tapered meandered arms,” *Microwave and Optical Technology Letters*, vol. 59, no. 5, pp. 1142–1145, May 2017.

[141] N. Michishita and Y. Yamada, “A novel impedance matching structure for a dielectric loaded 0.05 wavelength small meander line antenna,” in *2006 IEEE Antennas and Propagation Society International Symposium*, July 2006, pp. 1347–1350.

[142] C. Cho, H. Choo, and I. Park, “Broadband RFID tag antenna with quasi-isotropic radiation pattern,” *Electronics Letters*, vol. 41, no. 20, pp. 1091–1092, September 2005.

[143] H.-W. Son and C.-S. Pyo, “Design of RFID tag antennas using an inductively coupled feed,” *Electronics Letters*, vol. 41, no. 18, pp. 994–996, September 2005.

[144] Z.-J. Tang, J. Zhan, Z.-F. Xi, and Y.-G. He, “Broadband UHF RFID tag antenna with a rectangular-loop feed and additional patches,” *Microwave and Optical Technology Letters*, vol. 54, no. 5, pp. 1234–1236, May 2012.

[145] R. Lodato, V. Lopresto, R. Pinto, and G. Marrocco, “Numerical and experimental characterization of through-the-body UHF-RFID links for passive tags implanted into human limbs,” *IEEE Transactions on Antennas and Propagation*, vol. 62, no. 10, pp. 5298–5306, October 2014.

[146] M.-C. Tsai, C.-W. Chiu, H.-C. Wang, and T.-F. Wu, “Inductively coupled loop antenna design for UHF RFID on-Body applications,” *Progress In Electromagnetics Research*, vol. 143, no. 4, pp. 315–330, 2013.

[147] Q. Liu, Y. Yu, and S. He, “Capacitively loaded, inductively coupled fed loop antenna with an omnidirectional radiation pattern for UHF RFID tags,” *IEEE Antennas and Wireless Propagation Letters*, vol. 12, pp. 1161–1164, 2013.

[148] Y. Choi, U. Kim, J. Kim, and J. Choi, “Design of modified folded dipole antenna for UHF RFID tag,” *Electronics Letters*, vol. 45, no. 8, pp. 387–389, April 2009.

[149] S. Genovesi and A. Monorchio, “Low-profile three-arm folded dipole antenna for UHF Band RFID tags mountable on metallic objects,” *IEEE Antennas and Wireless Propagation Letters*, vol. 9, pp. 1225–1228, 2010.

[150] H. Sun, B. Tao, and O. M. Ramahi, “Offset-fed folded dipole and its application as RFID tag antenna,” *IEEE Journal of Radio Frequency Identification*, vol. 1, no. 2, pp. 109–114, June 2017.

[151] L. Ukkonen, D. Engels, L. Sydanheimo, and M. Kivikoski, “Planar wire-type inverted-F RFID tag antenna mountable on metallic objects,” in *IEEE Antennas and Propagation Society Symposium, 2004.*, vol. 1, June 2004, pp. 101–104 Vol.1.

[152] J. Liu, “Dual-band RFID tag antenna using coplanar inverted-F/L structure,” in *2010 IEEE International Conference on RFID-Technology and Applications*, June 2010, pp. 96–99.

[153] J. Zhang and Y. Long, “A novel metal-mountable electrically small antenna for RFID tag applications with practical guidelines for the antenna design,” *IEEE Transactions on Antennas and Propagation*, vol. 62, no. 11, pp. 5820–5829, November 2014.

[154] H. Kwon and B. Lee, “Compact slotted planar inverted-F RFID tag mountable on metallic objects,” *Electronics Letters*, vol. 41, no. 24, pp. 1308–1310, November 2005.

[155] M. Hirvonen, P. Pursula, K. Jaakkola, and K. Laukkanen, “Planar inverted-F antenna for radio frequency identification,” *Electronics Letters*, vol. 40, no. 14, pp. 848–850, July 2004.

[156] B. Yu, S.-J. Kim, B. Jung, F. J. Harackiewicz, M.-J. Park, and B. Lee, "Balanced RFID tag antenna mountable on metallic plates," in *2006 IEEE Antennas and Propagation Society International Symposium*, July 2006, pp. 3237–3240.

[157] G. Marrocco, "Body-matched RFID antennas for wireless biometry," in *The 1st European Conference on Antennas and Propagation (EuCAP)*, November 2006, pp. 1–5.

[158] G. Marrocco, "RFID antennas for the UHF remote monitoring of human subjects," *IEEE Transactions on Antennas and Propagation*, vol. 55, no. 6, pp. 1862–1870, June 2007.

[159] S. Manzari, S. Pettinari, and G. Marrocco, "Miniaturised wearable UHF-RFID tag with tuning capability," *Electronics Letters*, vol. 48, no. 21, pp. 1325–1326, October 2012.

[160] C. Occhiuzzi, S. Cippitelli, and G. Marrocco, "Modeling, design and experimentation of wearable RFID sensor tag," *IEEE Transactions on Antennas and Propagation*, vol. 58, no. 8, pp. 2490–2498, August 2010.

[161] Alien Technology, CA, USA. [Online]. Available: https://www.alientechnology.com/products/ic/higgs-4/.

[162] T. Bjorninen, A. A. Babar, A. Z. Elsherbeni, L. Ukkonen, L. Sydanheimo, and J. Kallioinen, "Compact metal mountable UHF RFID tag on a Barium Titanate based substrate," *Progress In Electromagnetics Research C*, vol. 26, pp. 43–57, 2012.

[163] MTI Wireless Edge Ltd., Israel. [Online]. Available: https://rfid.atlasrfidstore.com/hubfs/1_Tech_Spec_Sheets/MTI/ATLAS_MTI_MT-242025.pdf.

[164] JADAK, Novanta Inc., NY, USA. [Online]. Available: https://www.jadaktech.com/products/rfid/embedded-uhf-rfid-readers/mercury6e-m6e/.

[165] H. A. Wheeler, “Fundamental limitations of small antennas,” *Proceedings of the IRE*, vol. 35, no. 12, pp. 1479–1484, December 1947.

[166] S. R. Best, “A discussion on the properties of electrically small self-resonant wire antennas,” *IEEE Antennas and Propagation Magazine*, vol. 46, no. 6, pp. 9–22, December 2004.

[167] S. R. Best, “Low Q electrically small linear and elliptical polarized spherical dipole antennas,” *IEEE Transactions on Antennas and Propagation*, vol. 53, no. 3, pp. 1047–1053, March 2005.

[168] H. A. Wheeler, “The radiansphere around a small antenna,” *Proceedings of the IRE*, vol. 47, no. 8, pp. 1325–1331, August 1959.

[169] R. W. P. King, *The Theory of Linear Antennas.* Cambridge, MA, USA: Harvard University Press, 1956.

[170] L. J. Chu, “Physical limitations of omnidirectional antennas,” *Journal of Applied Physics*, vol. 19, no. 12, pp. 1163–1175, December 1948.

[171] R. Collin and S. Rothschild, “Evaluation of antenna Q,” *IEEE Transactions on Antennas and Propagation*, vol. 12, no. 1, pp. 23–27, January 1964.

[172] J. S. McLean, “A re-examination of the fundamental limits on the radiation Q of electrically small antennas,” *IEEE Transactions on Antennas and Propagation*, vol. 44, no. 5, pp. 672–, May 1996.

[173] R. W. Ziolkowski and A. Erentok, “At and below the Chu limit: Passive and active broad bandwidth metamaterial-based electrically small antennas,” *IET Microwaves, Antennas & Propagation*, vol. 1, no. 1, pp. 116–128, February 2007.

[174] A. D. Yaghjian and S. R. Best, “Impedance, bandwidth, and Q of antennas,” *IEEE Transactions on Antennas and Propagation*, vol. 53, no. 4, pp. 1298–1324, April 2005.

[175] H. L. Thal, “New radiation Q limits for spherical wire antennas,” *IEEE Transactions on Antennas and Propagation*, vol. 54, no. 10, pp. 2757–2763, October 2006.

[176] M. Gustafsson, C. Sohl, and G. Kristensson, “Physical limitations on antennas of arbitrary shape,” *Proceedings of the Royal Society A: Mathematical, Physical and Engineering Sciences*, vol. 463, no. 2086, pp. 2589–2607, July 2007.

Appendix A

Effect of Feed Structure on the Radiation Efficiency

Since the measurable input power of an antenna structure is typically the power at the input of the corresponding feed, it is more appropriate to consider the feed as a part of the whole radiating system, particularly for electrically small antennas. This is because, irrespective of whether it is a miniaturized antenna employing external matching network in its feed or an inherently matched miniaturized antenna using a balun as its feed (e.g., the miniaturized folded dipole antennas described in Chapters 4 and 5), the bandwidth and the losses in the feed structure are the two most critical parameters in determining how much power is actually being transferred from the input of the feed to the actual antenna terminals, which essentially will dictate the realized gain of the electrically small antenna and hence the overall radiated power.

A schematic diagram of an antenna with its feed structure has been shown in Fig. A.1, where P_{in} and $\Gamma_{in,F}$ are the overall input power and the reflection coefficient at the input terminals of the feed, respectively, $P_{acc,F}$ is the power accepted into the feed structure when terminated in the antenna, $P_{out,F}$ is the power output from the feed structure, $P_{acc,A}$ is the power accepted into the antenna, and finally P_{rad} is the radiated power from the antenna.

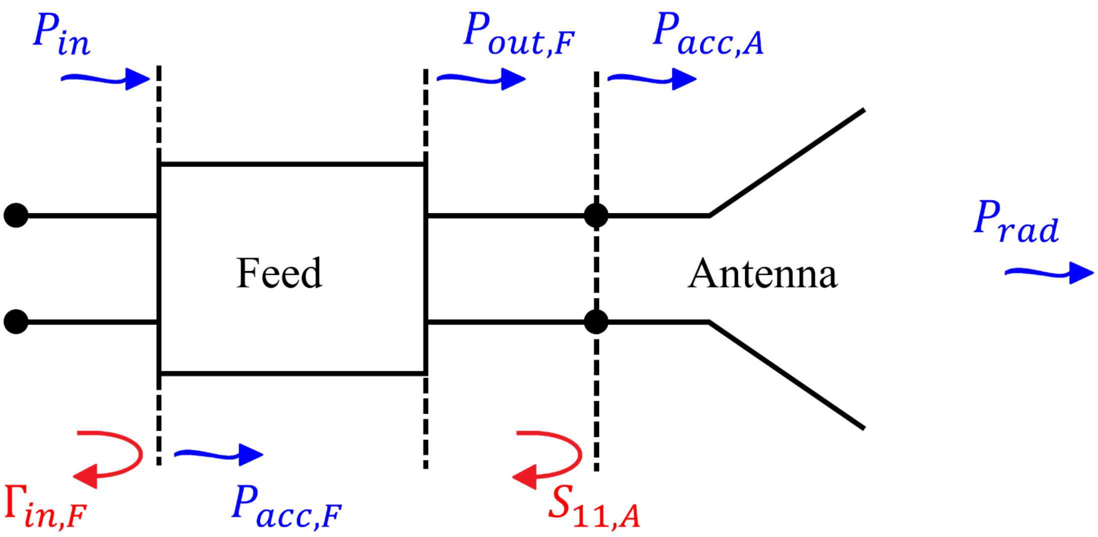

Figure A.1: Schematic diagram of the antenna with the feed structure.

Therefore, it is obvious that any insertion loss introduced by the feed and/or the reflection loss occurring from the feed-antenna interface will only get amplified due to multiple scattering between the input of the feed and the antenna. This will essentially determine the total power accepted into the whole system, and hence the overall radiation efficiency.

Considering the feed structure to be a two-port network, the overall radiation efficiency of the antenna including the feed structure can be given by the following equation:

$$\begin{aligned}\eta_{rad,O} &= \frac{P_{rad}}{P_{acc,F}} = \frac{P_{rad}}{P_{in}(1-|\Gamma_{in,F}|^2)} \\ &= \frac{P_{rad}}{P_{in}\left(1-\left|S_{11,F}+\dfrac{S_{12,F}S_{21,F}S_{11,A}}{1-S_{22,F}S_{11,A}}\right|^2\right)}\end{aligned} \tag{A.1}$$

where $S_{11,F}$, $S_{12,F}$, $S_{21,F}$, and $S_{22,F}$ are the generalized scattering parameters of the feed structure and $S_{11,A}$ pertains to the antenna loaded by the feed structure parasitically, but excluding the balun transformer.

Now, P_{rad} can be given as follows:

$$P_{rad} = P_{acc,A} \times \eta_{rad,A} \tag{A.2}$$

where $\eta_{rad,A}$ is the radiation efficiency of the antenna including the parasitic effects of the feed layout, which was obtained directly from HFSS. The accepted power into the antenna $P_{acc,A}$ can be expressed using the following equation:

$$P_{acc,A} = P_{out,F} \times (1 - |S_{11,A}|^2) = P_{in} \times |S_{21,F}|^2 \times (1 - |S_{11,A}|^2). \tag{A.3}$$

Thus, incorporating equations A.2 and A.3 into equation A.1, the overall radiation efficiency can be obtained as:

$$\begin{aligned} \eta_{rad,O} &= \frac{P_{in} \times |S_{21,F}|^2 \times (1 - |S_{11,A}|^2)}{P_{in}\left(1 - \left|S_{11,F} + \dfrac{S_{12,F}S_{21,F}S_{11,A}}{1 - S_{22,F}S_{11,A}}\right|^2\right)} \times \eta_{rad,A} \\ &= \eta_F \times \eta_{rad,A} \end{aligned} \tag{A.4}$$

where

$$\eta_F = \frac{|S_{21,F}|^2 \times (1 - |S_{11,A}|^2)}{1 - \left|S_{11,F} + \dfrac{S_{12,F}S_{21,F}S_{11,A}}{1 - S_{22,F}S_{11,A}}\right|^2}. \tag{A.5}$$

It may also be noted that, for an inherently well-matched antenna, $S_{11,A} \approx 0$, hence equation A.5 reduces to

$$\eta_F = \frac{|S_{21,F}|^2}{1 - |S_{11,F}|^2}. \tag{A.6}$$

Furthermore, for a broadband, low loss and well-matched feed structure, considering $S_{11,F} \approx S_{22,F} \approx 0$ and $S_{12,F} \approx S_{21,F} \approx 1$, η_F and $\eta_{rad,O}$ can be obtained as:

$$\eta_F = 1 \tag{A.7}$$

and

$$\eta_{rad,O} = \eta_{rad,A}. \tag{A.8}$$

Appendix B

Comparison of Physical Limits of The Miniaturized Folded Dipole Antennas

B.1 Fundamental Limitations of Electrically Small Antennas

An electrically small antenna (ESA) is one whose overall dimensions are typically much smaller than the wavelength. However, the definition can be somewhat ambiguous. Wheeler defined a small antenna as the one that has a maximum volume less than the "radiansphere" [168], which has a radius of one radian, i.e., $\lambda/2\pi$, λ being the wavelength. Other definitions can also be found – one example is that if the largest dimension of an antenna measured from its input terminals does not exceed one eighth of a wavelength, then the antenna can be called a small antenna [24]. However, for most modern ESAs, the definition provided by King is usually followed [169], which states that in order for an antenna to be "very short", the electrical size of the antenna ka must not be greater than 0.5, i.e., $ka \leqslant 0.5$, where k is the wavenumber $= 2\pi/\lambda$ and a is the smallest radius of the sphere that circumscribes the antenna completely. The antennas described in Chapters 4 and 5 are all 75% miniaturized, yielding the corresponding $ka \approx 0.4$. Thus, all the antennas discussed in this thesis can be considered as electrically small.

As mentioned earlier, it is a well-known fact that ESAs suffer from poor bandwidth and radiation efficiency. As the dimensions become smaller, the antenna becomes more reactive and less resistive. As a result, the antenna stores more energy than it dissipates, the latter mostly in the form of radiation and some ohmic loss. Thus, inspired by the similarities with reactive elements like an inductor or a capacitor, ESAs were also assigned quality factors (Q_{ant}) that are essentially the ratio of the maximum energy stored to the total power dissipated per period. The Q_{ant} of an ESA represents a fundamental limit on the performance of the antenna, and relates the bandwidth and radiation efficiency with its electrical size. However, it must be noted that unlike the quality factor of reactive elements, antenna quality factors are desired to be small in order to maximize the bandwidth and the radiated power. Chu calculated the minimum limit of Q_{ant} by assuming a vertically polarized dipole antenna fully enclosed by the smallest possible sphere, and then by expressing the radiated fields outside the sphere as a sum of several spherical modes by using spherical function expansion [170]. However, a simpler and far more convenient expression for Q_{ant} was derived by Collin and Rothschild [171] who evaluated the energy in terms of electromagnetic fields rather than the equivalent circuit approach used by Chu, which was later confirmed by McLean [172]. The exact expression of minimum Q_{ant} for the lowest order mode can be given as [171, 172]:

$$Q_{ant,min} = \frac{1}{ka} + \frac{1}{(ka)^3}. \tag{B.1}$$

For a generally lossy antenna with a radiation efficiency of η_{rad}, the expression becomes [167, 173]:

$$Q_{ant,min} = \eta_{rad}\left[\frac{1}{ka} + \frac{1}{(ka)^3}\right]. \tag{B.2}$$

B.2 Calculation of Quality Factors and Fractional Bandwidths for the Reported Miniaturized Antennas

Bandwidth is one of the most frequently used parameters by antenna and communication engineers. Thus, in an attempt to relate the bandwidth of an antenna specified by an arbitrary choice of VSWR to the corresponding quality factor, Yaghjian and Best derived the following expression [174]:

$$Q_{ant}(\omega_0) = \frac{2\sqrt{\beta}}{FBW_V(\omega_0)} \quad , \quad \sqrt{\beta} = \frac{\sigma - 1}{2\sqrt{\sigma}} \tag{B.3}$$

where σ is the VSWR level, and $FBW_V(\omega_0)$ is the fractional VSWR bandwidth at the operating frequency ω_0, and can be calculated by taking the ratio of the bandwidth at the specified VSWR level to ω_0. Thus, the upper limit of the fractional bandwidth can be found using equations B.2 and B.3 as:

$$FBW_{V,max}(\omega_0) = \frac{2\sqrt{\beta}}{Q_{ant,min}(\omega_0)} = \frac{\dfrac{\sigma - 1}{\sqrt{\sigma}}}{\eta_{rad}\left[\dfrac{1}{ka} + \dfrac{1}{(ka)^3}\right]}. \tag{B.4}$$

However, these equations can only be used if the following three conditions are maintained: (1) the antenna needs to be resonant at the operating point, (2) the antenna should be well-matched with respect to the corresponding source impedance, and (3) no other resonance should be present within the selected VSWR bandwidth.

The quality factors and the fractional bandwidths of the proposed miniaturized folded dipole antenna and the equivalent loaded conventional antenna described in Chapter 4, and the fully printed antenna described in Chapter 5 were calculated for $\sigma = 2$ (i.e., ≈ 10-dB return loss level) using equation B.4 and compared in Table B.1.

It is noteworthy at this point that each of the aforementioned three conditions holds true for all the three antennas. Although the miniaturized folded dipole antennas have the

Antenna Type	ka	σ	$\eta_{rad}\,(\%)$	$Q_{ant,min}$	Q_{ant}	$\frac{Q_{ant}}{Q_{ant,min}}$	$FBW_{V,max}$	FBW_V
Lumped-L loaded miniaturized folded dipole (Fig. 4.10)	0.4	2	35.3	6.3	47.1	7.48	0.112	0.015
Equivalent loaded conventional dipole (Fig. 4.13(b))			36.1	6.5	54.4	8.37	0.109	0.013
Fully printed miniaturized folded dipole (Fig. 5.1)			28.3	5.3	28.3	5.34	0.133	0.025

Table B.1: Comparison of antenna quality factors and the fractional bandwidths of the antennas reported in the thesis.

antiresonance $f_{AR,1}$ situated very close to the operating point $f_{R,N}$, due to the narrowband return loss response, $f_{AR,1}$ is always situated outside the 10-dB bandwidth of both the antennas. Furthermore, the miniaturized RFID tag antenna could not be included in this comparison, since it does not operate at any of the resonances in order to attain the required complex input impedance. It can be noticed from Table B.1 that the lumped inductor loaded miniaturized dipole antenna has very close but slightly better quality factor and fractional bandwidth compared to the equivalent conventional dipole antenna, however best results are obtained by the fully printed miniaturized folded dipole antenna owing to its slightly more lossy reactive loading topology, which essentially results in a better bandwidth at the expense of radiation efficiency.

The methods described for calculating the lower bound of antenna quality factor so far only consider the fields external to the smallest sphere circumscribing the ESA, and any stored energy present within the sphere, i.e., between the actual antenna volume and the sphere are ignored. Thus, for linear or planar antennas, which occupy only a fraction of the whole spherical volume, the actual lower bound of the quality factor should in fact be somewhat higher than that calculated using equation B.1, owing to the unaccounted additional energy stored in the empty space within the spherical volume [175, 176]. This, in turn justifies the high values of $Q_{ant}/Q_{ant,min}$ for the miniaturized antennas listed in Table B.1. Conversely, if an antenna occupies most of the available space inside the sphere, the corresponding Q_{ant} becomes very close to the $Q_{ant,min}$ calculated using equation B.1 [165, 167]. In other words, the larger the footprint of an antenna is within the particular sphere, the closer is its quality factor to the absolute lower bound, i.e., $Q_{ant,min}$ calculated using equation B.1. The three antennas listed in Table B.1 have the same length, i.e., $ka \approx 0.4$, and thus can be circumscribed by the same spherical volume. However, the overall widths $(w_{dr} + s + w_{fd})$ corresponding to the lumped inductor loaded folded dipole, equivalent conventional dipole and the fully printed folded dipole are 3.25 mm, 1 mm, and 4 mm, respectively, which are consistent with the calculated $Q_{ant}/Q_{ant,min}$ values.